Dynamic Failure Characteristics in Layered Materials and Structures

Thesis by

Luoyu Roy Xu

In Partial Fulfillment of the Requirements

For the Degree of

Doctor of Philosophy

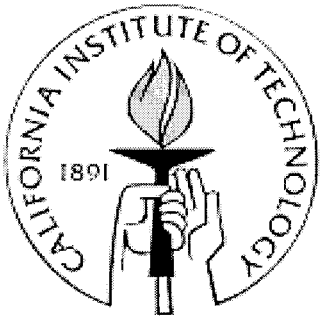

California Institute of Technology

Pasadena, California 91125

2002

(Defended June 19, 2001)

Acknowledgements

I was very fortunate to work with an excellent mentor, Prof. Ares J. Rosakis. I am indebted to him for his support, advice and encouragement through the completion of the work summarized here. It is his unusual passion to scientific research that made me feel that I spent only "five dynamic microseconds," rather than five lengthy years in the subbasement "Cage" Laboratory of Firestone building.

I cannot thank Prof. Guruswami Ravichandran enough, who unceasingly monitored my learning process at Caltech. His wise and generous advice kept me focused all along. I benefited greatly from my interaction with Prof. Michael Ortiz, a dedicated scholar and a trendsetter in computational mechanics. Two of my favorite instructors at Caltech are Prof. William Johnson and Prof. Wolfgang Knauss, whose comprehensive knowledge of materials and mechanics, together with an organized teaching style, contributed greatly to my intellectual development. I am also grateful to Prof. Thomas H. Heaton for taking time to review this dissertation and serving on my thesis committee.

This thesis could not be completed smoothly without the numerous discussions and direct assistance from Dr. David Owen, "second commander "of our group; our non-metal sub-group members, Dr. Demirkan Coker and Dr. Omprakash Samudrala; and metal sub-group members, David Anderson, Dr. Benjamin Chow and Dr. Pradeep Guduru; senior laboratory specialist, Petros Arakelian and senior administrative secretary, Denise Thobe. I would also like to thank Joe Haggerty, Ali Kiani, Bradley St. John, and Larry Frazier for their advice and help in machining my numerous non-standard specimens.

Special thanks go to Prof. Younggang Y. Huang of the University of Illinois at Urbana-Champaign, for his insightful discussion on the dynamic failure in layered materials, and for his direct contributions to the modeling of crack deflection and penetration problem at an interface. My Caltech experience and academic career was initiated by a GALCIT alumnus, Prof. Weinong Chen at the University of Arizona. Weinong and I go back to our times at the Beijing University of Aeronautics and Astronautics, and I always consider him as one of my closest friends.

Thanks to Dr. Y. D. S. Rajapakse of the Office of Naval Research for the generous financial support.

Lastly, I cannot overlook the contribution of my wife, Lihong, and our daughter, Tan. Their loving support and care have allowed me to concentrate 100% of my abilities on the completion of this thesis.

Abstract

Systematic investigations were carried out to understand the general nature of dynamic failure mechanisms in layered materials and structures such as composite and sandwich structures, thin films, layered armors and layered rock. A series of impact experiments on model-layered specimens were conducted using high-speed photography and dynamic photoelasticity.

For the first time, the sequence and interaction of two major dynamic failure modes in layered materials—inter-layer cracking and intra-layer cracking were revealed in real time. For heterogeneous three-layer systems, shear-dominated inter-layer cracking was always the first failure event for specimens subjected to low-speed impact. Inter-layer cracking generally nucleated from interfacial locations where the inter-layer shear stress acquired a local maximum. Depending on impact speed and bond strength characteristics, inter-layer cracks were very transient and often became intersonic even under moderate impact speeds. Intra-layer cracking always initiated after the development of inter-layer cracks as a result of inter-layer crack kinking into the adjacent layer. The resulting intra-layer mode I cracks often accelerated and branched as they attained high speeds, causing core layer fragmentation. For homogenous-layered systems composed of bonded layers of Homalite, intra-layer cracks appeared in the form of cracks radiating from the impact site. As soon as these cracks approached an interface, inter-layer cracks were often induced depending on the angle between the crack path and the interface. Direct experimental evidence of the dynamic equivalent of "Cook-Gordon mechanism" was recorded, i.e., two intersonic interfacial cracks nucleated and

propagated along the interface before a fan of mode I incident cracks was ever able to reach the interface. Also, significant dependence of the failure characteristics on impact speeds and interfacial strengths was found. For the heterogeneous three-layer system subjected to a high impact speed, two clear shear shock waves associated with the intersonic inter-layer cracks were observed at the specimen center. Shock waves were also observed along the interface in heterogeneous three-layer systems featuring weak and ductile bonds. The impact momentum and loading duration were identified as two important parameters in damage spreading for a given impact energy.

Motivated by the experimental observations of crack deflection/penetration at an interface, a novel wedge-loaded impact specimen was designed to explore the basic mechanics nature of this phenomenon. The deflection/penetration behavior of an incoming dynamic crack at an interface was found to depend on the interfacial angle and the interfacial fracture toughness. A dynamic fracture model, together with an energy criterion, were proposed and were found to agree reasonably well with the experimental observations.

Table of Contents

Chapter II

Impact Failure Characteristics in Sandwich Structures; Part II: Effects of Impact Speed and Interfacial Strength

Chapter III

An Experimental Study of Impact-induced Failure Events in Homogeneous Layered Materials Using Dynamic Photoelasticity and High-speed Photography

Chapter IV

Dynamic Crack Deflection and Penetration at Interfaces in Homogeneous Materials: Experimental Studies and Model Prediction

Summary

This doctoral dissertation consists of four chapters, each with its own abstract, introduction and conclusions. The overall scope of this work is to understand the basic features of dynamic failure in layered materials and structures. In order to simulate the general dynamic failure behavior in layered materials and structures such as composite and sandwich structures, thin films, layered armors and rock, a series of model configurations were designed and tested. Two extreme cases were considered to include many possible combinations of layered materials and structures. Figure 1 (a) represents specimens featuring highly mismatched material combinations (high differences in wave speeds), which is more characteristic of modern sandwich structures involving soft core and stiff faceplates. Figure 1 (b) represents the other extreme of a constitutively homogenous structure involving weak planes or interfaces, a situation more characteristic of layered geological structures. The dynamic response and failure characteristics of a general layered material should be within the ranges of these two extreme cases.

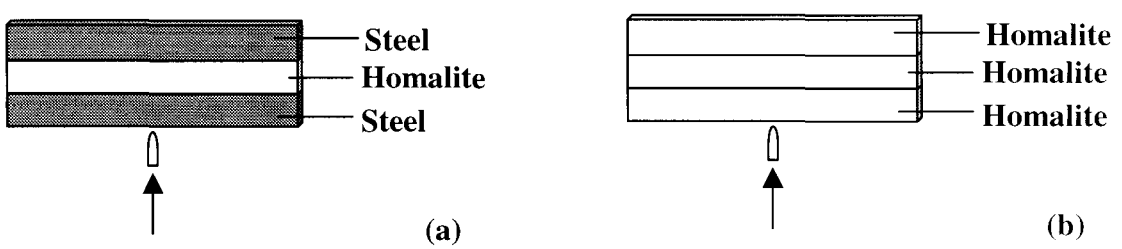

Figure 1. (a) Illustrations of the heterogeneous three-layer specimens and (b) homogenous three-layer specimens

The first chapter of this thesis deals with the investigation of basic failure modes in heterogeneous three-layer materials or model sandwich structures. Model sandwich

specimens involving a compliant polymer core sandwiched between two metal layers were designed and subjected to low-speed impact to simulate failure evolution mechanisms in real sandwich structures. High-speed photography and dynamic photoelasticity were utilized to study the nature and sequence of such failure modes. A series of complex failure modes was observed. In all cases, inter-layer (interfacial) cracks appeared first. These cracks were shear-dominated and were often intersonic even under moderate impact speeds. The transition from inter-layer crack growth to intra-layer crack formation was also observed. The shear inter-layer cracks kinked into the core layer, propagated as opening-dominated intra-layer cracks and eventually branched as they attained high enough growth speeds causing core fragmentation.

After we identified the dominant failure modes in heterogeneous three-layer materials in a baseline case, we changed the external loading and internal material design (e.g., interfacial bond strengths) to explore their effects on the dynamic failure characteristics. The second chapter details these issues. Results show that high impact speeds led to high inter-layer crack speeds. For an inter-layer crack at the intermediate strength interface, the crack speed was slightly slower than that at the strong interface. However, for a crack at the weak but ductile interface, it initiated much later and had a very high speed at the first stage compared to a crack at the strong interface. Impact momentum and loading duration were identified as two important parameters in characterizing damage spreading for a given impact energy.

As we move from heterogeneous-layered materials to homogenous-layered materials as shown in Figure 1(b), failure characteristics were observed to be quite different. The third chapter describes experimental investigations on the generation and

the subsequent evolution of dynamic failure events in homogeneous-layered materials. Tested configurations included three-layer and two-layer Homalite specimens featuring different bond strengths. Here again high-speed photography and dynamic photoelasticity were utilized to study the nature, sequence and interaction of dynamic failure modes. In most cases, and at early stages of the impact event, intra-layer failure (or bulk matrix failure) appeared in the form of cracks radiating from the impact point. These cracks were opening-dominated and their speeds were less than the crack branching speeds of Homalite-100. Subsequent crack branching in several forms was also observed. Mixed-mode inter-layer cracking (or interfacial debonding) was induced when the intra-layer cracks approached the interface at a small incident angle (angle between the crack path and the interface). The dynamic interaction between inter-layer crack growth and intra-layer crack formation (or the dynamic equivalent of so-called "Cook-Gordon Mechanism") was visualized for the first time. Interfacial strength played a significant role in impact damage spreading. Cracks arrested at weak bonds and the stress wave intensity was reduced dramatically by the use of a thin but ductile adhesive layer.

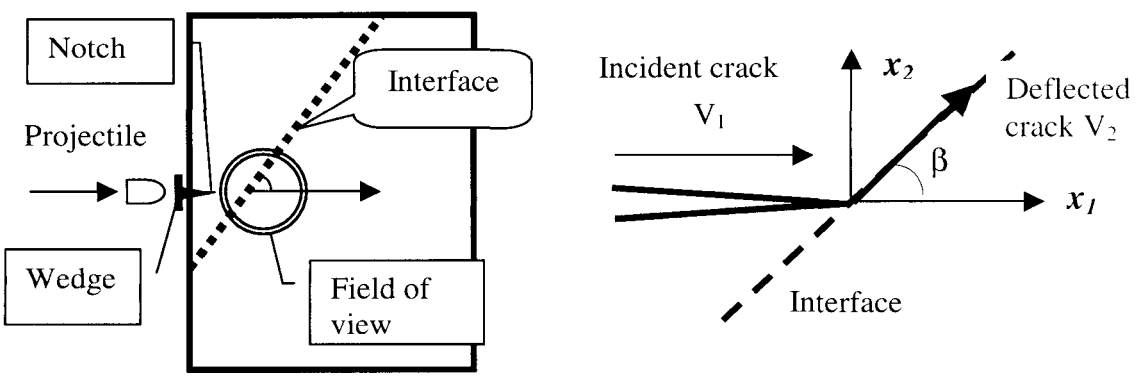

Figure 2. (a) A novel specimen for experimental studies on dynamic crack deflection and penetration at interfaces and (b) the illustration for modeling of this mechanics problem

Motivated by the observations of dynamic crack deflection and penetration at interfaces in homogeneous materials, a novel wedge-loaded specimen, shown in Figure 2, was designed to investigate the effects of interfacial angles and interfacial fracture toughnesses on the dynamic fracture behavior at an interface as described in the fourth chapter. A dynamic fracture mechanics model, together with an energy criterion, were proposed to predict the crack deflection or penetration at the interface. Results show that for a given incident mode I crack and a specific interfacial angle, if the interfacial bonding is weak, a dynamic crack is easily deflected at the interface. The resulting interfacial crack is mixed-mode and its speed is much higher than the incident mode I crack speed. For a given incident crack and an interfacial bond, if the interfacial angle is small enough, a dynamic crack always deflects and never penetrates the interface.

The practical layered materials or structures generally consist of more than three layers. However, the two-layer system (illustrated in Figure 3 (a)) and three-layer system are basic configurations. In this thesis, only the results of three-layer systems are included. The failure characteristics of two-layer systems are slightly different from the failure features of three-layer systems and will be published in an independent paper. Also, experimental studies on the layered systems with initial defects (shown in Figure 3 (b)) were performed and the results will be reported elsewhere.

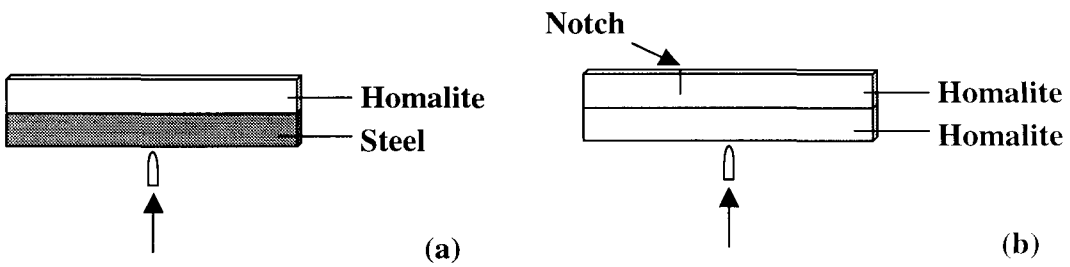

Figure 3. (a) Illustration of the two-layer system and (b) layered systems with initial defects (b)

Chapter I

Impact Failure Characteristics in Sandwich Structures; Part I: Basic Failure Mode Selection

Abstract

In the present work we present a systematic experimental investigation of the generation and subsequent evolution of dynamic failure modes in sandwich structures subjected to low-speed impact. Model sandwich specimens involving a compliant polymer core sandwiched between two metal layers were designed and subjected to impact loading to simulate failure evolution mechanisms in real sandwich structures. High-speed photography and dynamic photoelasticity were utilized to study the nature and sequence of such failure modes. A series of complex failure modes was documented. In all cases, inter-layer (interfacial) cracks appeared first. These cracks were shear-dominated and were often intersonic even under moderate impact speeds. The transition from inter-layer crack growth to intra-layer crack formation was also observed. The shear inter-layer cracks kinked into the core layer, propagated as opening-dominated intra-layer cracks and eventually branched as they attained high enough growth speeds causing core fragmentation.

I-1. Introduction

Layered materials and sandwich structures have diverse and technologically interesting applications in many areas of engineering. These include the increased use of composite laminates in aerospace and automotive engineering; the introduction of layered concrete pavements in civil engineering; the use of thin films and layered structures in

micro-electronic components, and very recently, the introduction of sandwich structures in a variety of naval engineering applications [1-3]. In an entirely different length scale such materials and structures are also found in the natural layered rock structure of earth's crust. While failure characteristics of layered materials and sandwich structures subjected to static loading have been investigated extensively in the past years, their dynamic counterparts have remained elusive [1-7]. Indeed, the presence of highly complex and transient dynamic failure modes in such materials and the inaccessibility of internal damage to real-time scruting have resulted in experimental studies limited to only the final impact damage characteristics of failure and to measurement of post-mortem residual strengths [4-7]. To begin addressing the need for real-time observations of failure events, the work presented here focuses on the study of such events in model sandwich structures, and in particular, on the identification of their nature, chronological evolution and interaction.

To identify the evolution of failure modes for different loading regimes, it is convenient to first classify these modes based on the material constitutions of layered/reinforced structures. As shown schematically in Figure 1, there are two major categories of failure observed in post-mortem studies. The first major failure category is decohesion (or cracking) between bonded layers at an interface. This is often referred to as delamination in composite laminates or interfacial debonding in thin films or sandwich structures. It is also called inter-layer failure. Generally, two distinct inter-layer failure modes are observed. The first one involves opening-dominated inter-layer cracking or "delamination buckling" [8-10]. The second one involves shear-dominated inter-layer

cracks or "shear delaminations," and often occurs in layered materials subjected to out-of-plane impact [11-13].

The second major category is referred to as intra-layer failure. There are three possible intra-layer failure modes depending on the material constitution. The first one is called intra-layer cracking or matrix cracking. This type of cracking often occurs inside the matrix of fiber-reinforced composites or within the soft core of sandwich structures [14-15]. It is also found in the form of tunneling cracks in thin film/substrate structures [1,16]. Another possible intra-layer failure is the failure of reinforcements such as fiber breakage and fiber kinking within a layer [17-18]. The fifth possible intra-layer failure mode is interfacial debonding between the matrix material and the reinforcement [19] such as debonding between particle/fiber and matrix occurring within a constituent layer. As stated earlier, for most layered materials, the presence of such highly complicated dynamic failure modes and the inaccessibility of internal damage to direct observation explain the fact that only the final impact damage characteristics of such structures are usually discussed in the open literature. Indeed, the sequence, nature and interaction of such failure process were never properly clarified. Notable exception to this rule is the early studies of Takeda et al. [20], who observed the evolution and sequence of matrix cracks and delamination failure in glass fiber composite laminates under ballistic impact. However, the equivalent situation involving low or intermediate-speed impact loading has yet to be investigated.

In the recently emerging field of soft core, sandwich structures, the first studies of failure mechanisms have again concentrated on static loading conditions. The work of Carlsson and his research group is pioneering in this aspect [21]. In perhaps the first

attempt to visualize impact failure in a real sandwich structure used in Naval applications. Samenski and Rosakis tested thin sections of such plate structures composed of PVC foam cores, sandwiched between E-glass faceplates [22]. The sections were subjected to direct impact through a steel projectile traveling at a speed of 56 m/s. A pulsed laser was used to illuminate the specimens from the back side and a high-speed camera recorded the deformation and failure events. A sequence of photographs corresponding to this process is shown in Figure 2 together with the post-mortem picture of the recorded specimen. As evident from the post-mortem picture, there are, at least, two types of failure present. Inter-layer failure demonstrates itself in the form of delamination between the face plates and the foam core at the vicinity of the impact site and free edges. On the opposite side, delamination is evident only on the top and on the bottom part of the specimen (away from the specimen center line). Intra-layer failure in the form of mode I, opening cracks in the soft core is also observed forming a highly symmetric pattern. Because the core is opaque, the high-speed pictures shown below are of limited use. What they show, however, is the emergence and propagation of the opening intra-layer (matrix) cracks inside the foam core. Indeed, these cracks seem to originate at the fiber glass/PVC interface opposite to the side of impact, and to symmetrically propagate towards the impact point. These cracks originate at the same location where the fiberglass /PVC delamination terminates. However, the time sequence and interaction between such inter-layer delaminations and the visible intra-layer, opening cracks in the core are not obvious. Indeed, the backlit real-time photographs do not show any evidence of interfacial delamination within the time window of observation. As we will show later, this observation is misleading and is due to the fact that inter-layer fractures are typically

shear-dominated. As such they do not allow for light to go through during the recording event because the shear crack faces remain in contact at the early stages of this process.

The inability of back-lit photography to visualize the failure process completely, motivates the use of partially transparent model sandwich systems which allow the use of full field optical techniques capable of capturing the nucleation and growth of both opening and shear-dominated cracks and their transition from one mode to the other. For many complex engineering problems, model experiments may prove extremely useful as intermediate steps, which reveal the basic physics of the problem and provide relatively straightforward explanations of the failure patterns observed in post-mortem observations. A striking example of this approach was provided by Riley and Dally [23], who designed a model metal/polymer layered system subjected to dynamic loading. Their model configuration was designed to simulate stress waves in layered structures. A similarly successful approach was adopted by Walter and Ravichandran [24], who designed a model aluminum/PMMA/aluminum specimen to simulate and visualize the static debonding and matrix cracking process in cemamic matrix composites.

In our experiments, we also adopt the same idea and introduce an appropriate intermediate model configuration. In order to simulate the difficult three-dimensional problem of the out-of-plane impact of real sandwich structures and to simultaneously preserve the essence of the failure phenomena involved, we introduce a two-dimensional, plane stress specimen, which represents a cross-sectional cut of the layered material as illustrated in Figure 3. For this type of model specimen, the failure process is easy to record, visualize and analyze. It is noted that although the exact impact mechanics involved in two configurations is not identical (the real case is three-dimensional while

the model specimen is closer to a plane stress state), the mechanisms of stress wave propagation and failure progression of the real and the model layered materials are quite analogous. In designing these model two-dimensional sandwich specimens, it is important to select model materials whose elastic mismatch is similar to that of materials used in real engineering applications (in our case PVC/composites). Selecting similar Dundurs' parameters [1] may ensure similarity of the elasto-static response for the interfacial mechanics problem. Meanwhile, selecting model material combinations with similar ratios of wave speeds of two constitution materials to the real structure is perhaps the most important consideration in the dynamic case, where timing of events and stress intensity are governed by the constituent material wave speeds. Also, the ratio of inter-layer and intra-layer strengths (or fracture toughnesses) is important. These three issues provide sets of similarity rules to connect the real structures to our models tests.

As schematically shown in Figure 3, matrix cracks and delamination are the two major impact failure modes in sandwich structures and composite laminates [4-5]. At some intersection points, matrix cracks and delamination are connected as also seen in the post-impact picture of Figure 2. One frequently asked question in the literature is whether the matrix cracks lead to the delamination or the delamination happens first and subsequently kinks into the adjacent layer inducing the matrix crack. This is a typical problem of sequence and failure mode transition identification. In addition to these basic failure modes and the terminology discussed above, there is also further specialized classification common in the literature [4]. Indeed, there are other types of matrix cracks called "bending matrix cracks," which are cracks that are straight and normal to the

interface while matrix cracks inclined to the interface often carry the misnomer of "shear matrix cracks." So the nature of matrix cracks needs to be investigated.

Since the nature and origin of such failure mechanisms can only be theorized by post-mortem observations, the necessity of full-field real-time, high-speed measurements becomes obvious. To this effect, the objectives of the current work are to conduct systematic experimental studies of the time evolution and nature of different dynamic failure modes and to investigate their interactions. Through these model experiments, we try to identify the basic physical phenomena, and to provide guidance for theoretical models and much needed, real-time, validation of numerical codes. To make this comparison more meaningful, we choose model material combinations that have the ratios of wave speeds very close to those used in real sandwich structures. Their properties are discussed in the following section.

I-2. Experimental procedure

I-2.1 Materials and specimens

Two kinds of materials were used in the experiments described below. A 4340-carbon steel was employed to simulate the stiff and strong fiberglass faceplates of sandwich structures. The polymeric material, which was used to simulate the weak core layer, such as the PVC foam core or balsa wood in sandwich structures or the 90^{0} plies in cross-ply laminates, is Homalite-100. Some physical properties of these model materials are listed in Table 1. The adhesive used to bond the metal/polymer interface is Weldon-10. The detailed properties of this adhesive and the effect of interfacial strength variation on dynamic failure mode selection are reported in part II of this investigation [25].

The shear wave speed is an important parameter in this investigation. The shear wave speed ratio for the core and faceplate is 3.2 for typical E-glass/PVC sandwich structures of the type that have recently been used in construction of full-scale composite ships [3] (e.g., the Swedish "Visby" class corvettes). Details on the complete set of physical and constitutive properties for E-glass composite materials have recently been discussed by Oguni et al. [18]. For comparison, the same shear wave speed ratio, for the idealized steel/Homalite model sandwiches, is about 2.7 based on the data from Table 1. Although the absolute values of these constituent properties are very different in the "idealized" versus the "real" solids, the idealized material combinations have been chosen in such a way as to have a shear wave speed ratio that is very similar to its real sandwich counterparts.

As shown in Figure 4, three different types of model sandwich specimen geometries were designed and tested. Type A specimens have equal layer widths and involve two different materials. They contain two metal layers with one polymer layer sandwiched between them. Type B specimens involve two thin metal layers (faceplates) and one polymer layer. This type of specimens is quite similar in geometry (ratio of core to face plate thickness) to realistic sandwich plates used in engineering applications. The only difference between type C and type B specimens is their lengths. Type C specimens are twice as long as type B specimens. The purpose of type C specimens is to explore the impact failure patterns with least edge effect present in the time scale of the failure process. All three types of specimens have the same out-of-plane thickness of 6.35mm (0.25 inch).

I-2.2 Experimental setup

The majority of experiments in this investigation were performed using dynamic photoelasticity. This classical method has recently found a lot of new applications such as study of the dynamic fracture processes in functionally gradient materials (FGMs) described by Parameswaran and Shukla [26]. The Coherent Gradient Sensing (CGS) method [27] was also used in a small number of cases. A schematic of the dynamic photoelasticity setup used here is given in Figure 5. Two circular polarizer sheets were placed on either side of the specimen. An Innova Sabre argon-ion pulsed laser was used as the light source. The coherent, monochromatic, plane polarized light output was collimated to a circular beam of 100 mm in diameter. The laser beam was transmitted through the specimen and the resulting fringe pattern was recorded by the high-speed camera. A Cordin model 330A rotating-mirror type high-speed film camera was used to record the images. During the impact test, a projectile was fired by the gas gun and impacted the specimen center. The generation of isochromatic fringe patterns is governed by the stress-optic law. For the case of monochromatic light, the condition for the formation of fringes can be expressed as [28]:

$$\hat{\sigma}_1 - \hat{\sigma}_2 = \frac{Nf_\sigma}{h}$$

where $\hat{\sigma}_1 - \hat{\sigma}_2$ is the principal stress difference of the thickness averaged stress tensor. f_σ is the material fringe value, N is the isochromatic fringe order and h is the half specimen thickness. The isochromatic fringe patterns observed are proportional to contours of constant maximum in-plane shear stress, $\hat{\tau}_{\max} = (\hat{\sigma}_1 - \hat{\sigma}_2)/2$.

I-3. Results and discussion

I-3.1 Failure process in type A specimens (with equal layer widths and a short length)

The diameter of the laser beam used in this investigation was 100 mm; however, the maximum length of the zone that had to be investigated was 254 mm long. In order to observe all possible dynamic failure modes present in each case, the field of view had to be moved from one location to another for each specimen configuration under the same impact condition. Figure 6 presents a series of photoelastic images of the Homalite core layer of a type A specimen. In all these experiments, the projectile impacted the center of the bottom metal layer. The dark circular spot at the upper right corner is a scaling mark (diameter 6.35 mm) bonded on the specimen. The thin horizontal dark line, seen around the center of every image, is the streak line of the camera. This line provides a stationary reference when the whole specimen moves during the impact process. At first, the field of view was centered on the middle of the specimen because it was close to the impact position and failure was expected to initiate from this zone. As shown in Figure 6 (b), about 158 μs after impact, two inter-layer cracks at the lower interface entered the field of view (from the right and left respectively) and propagated towards the specimen center. Before that time, there was no visible damage within the field of view. Later on (around 182 μs), the two inter-layer cracks, identified by the moving concentration of fringes at their tips, are seen to meet each other in Figure 6 (d). Similar to shear-dominated interfacial cracks in bimaterials [27,29-30], those inter-layer cracks are also shear-dominated. Because the Homalite and steel layers are still in contact up to that time, no visual evidence of decohesion is apparent in the images, although these cracks

have already broken the interface in a combination of compression and shear. After these two inter-layer cracks meet at the center, a bright gap between the Homalite and steel layers can be seen to appear in Figure 6 (e). Along this clearly opened interface and on the Homalite side, two Rayleigh surface waves are now seen to propagate, originating from the center and moving outwards, the specimen edges. The crack speed history for one of the two lower inter-layer cracks is plotted in Figure 7. The dynamic shear wave speed of Homalite-100 (see Table 1) is also shown as a horizontal dashed line. This value has been obtained experimentally by the procedure outlined by Xu and Rosakis [31].

Within the resolution of our measurement, the interfacial (inter-layer) crack tip speed remains very close to the shear wave speed of the core material (Homalite-100) and exhibits temporary subsonic and intersonic fluctuations. This is a phenomenon very similar to the one reported by Lambros and Rosakis [29], who looked at the dynamic fracture behavior of metal/polymer bimaterial interfaces subjected to asymmetric impact loading. Indeed, for moderate impact speeds the interfacial cracks were seen to accelerate unstably to the shear wave speed of the polymer and to fluctuate above that value before more energy was provided to the system at which instant they became clearly intersonic. The dependence of this behavior on impact speed and bond strength was recently analyzed by Needleman and Rosakis [32] with very similar conclusions. In the present case, the inter-layer crack speeds are too close to the shear wave speed of Homalite-100 to exhibit the clear shock wave structure characteristics of intersonic fracture. However, as the impact speed is increased, this structure will become clearly visible in the high-speed impact experiments to be presented in Part-II of this work [25].

Perhaps the most interesting conclusion deriving from the sequence shown in Figure 6 is the fact that delamination did not initiate in the interface directly above the impact point but did so outside our central field of view at two symmetric, off-axis, locations along the lower interface. In order to discover the location of crack nucleation, we must move our field of view off the specimen center to investigate the origins of these inter-layer cracks. To achieve this we first center our field of view to the middle between the specimen edge and the center, as shown in Figure 8 (a). The loading condition and geometry are intentionally kept identical. About 129 μs after impact, an inter-layer crack at the lower interface entered the field of view from the left and propagated towards the specimen center. This crack eventually met with its symmetric counterpart at the specimen center as shown in Figure 6. As explained earlier, the interface first broke in shear and afterwards separated to form a visible gap. A Rayleigh surface wave was then formed and propagated along the resulting free surface. The Rayleigh wave started from the specimen center and propagated towards the specimen edge as shown in Figure 8 (c). Meanwhile, as also shown in Figure 8 (c), another inter-layer crack appeared at the upper interface and also propagated towards the center. At a location close to the circular mark (dark dot), the upper inter-layer crack kinked into the Homalite core layer thus forming an intra-layer crack (matrix crack) as shown in Figure 8 (d). After a short period of acceleration, the kinked crack branched into a fan of cracks shown in Figure 8 (e). Crack branching as reported by previous researchers [33] often initiates when a crack in a homogeneous solid reaches high fractions of the shear wave speed, for example, 30-40% shear wave speed of Homalite-100. Based on this observation, we can conclude that the kinked intra-layer cracks (matrix cracks) occur after the formation of both (lower and

upper) inter-layer cracks (delamination cracks). These kinked cracks are of the purely mode-I type (opening mode) and are typical of all cracks in any homogeneous, isotropic solids. This phenomenon is indeed consistent with our early discussion of failure in real fiberglass/PVC sandwich structures presented in the introduction (see Figure 2). The photoelastic investigation merely confirms our earlier suspicion that shear-dominated delamination occurs first. It is only later followed by cracks kinking into the core layer from the side opposite to the impact point and moving towards the impact location. We suspect that this is also what happens in the fiber-reinforced composite laminates studied by Sun and Rechak [7]. Here again the cracks kinking to the central 90^{o} layer are opening-dominated rather than shear-dominated, although they are often referred to "shear matrix cracks" in the literature. Because fiber-reinforced composite materials show transversely isotropic mechanical properties [34], mode I opening cracks rather than mode II shear cracks occur in the 90^{o} central layer.

In order to conclusively identify the origins of the upper and lower inter-layer cracks, the field of view was once more moved to the specimen edge as shown in Figure 9 (a). After impact at the specimen center, the stress waves in the bottom steel layer propagated towards the edge creating a visible head wave structure on the lower wave speed polymer side (see Figure 9 (b)). Right after the stress wave reached the free edge, due to the existence of a stress singularity at the bimaterial corner [35], an inter-layer crack initiated at the lower interface as seen in Figure 9 (c). This crack propagated towards the specimen center. After around 160 μs, another inter-layer crack initiated at the upper interface also moving towards the center. This upper inter-layer crack soon kinked into the core layer and branched into a fan of multiple mode I intra-layer cracks.

This process is very consistent with the result of Figure 8 demonstrating the repeatability of this phenomenon.

The speed history of two inter-layer crack tips is presented in Figure 10 (a). It is noticed that the inter-layer crack at the lower interface can reach intersonic speeds but the inter-layer crack at the upper interface is a purely subsonic crack. It is interesting to note that the crack speed of the lower inter-layer crack reached the Rayleigh wave speed of Homalite-100 within 20 μs after the crack initiation. However, the crack speed suddenly dropped to a very low value (close to zero) around 90 μs after impact. Then, the crack speed again increased dramatically and fluctuated to intersonic and subsonic levels about the shear wave speed of Homalite-100. The maximum recorded crack tip speed was close to $\sqrt{2}\ C_s^H$, where C_s^H is the shear wave speed of the Homalite core layer. The crack speed history is obtained by numerically differentiating the crack length history, shown in Figure 10 (b). Figure 11 shows the global trends of the lower inter-layer crack tip speed plotted as a function of position from the specimen free edge. Results from all three identical specimens subjected to the same impact conditions, discussed earlier, are collectively displayed in this Figure. In these experiments, the field of view varied from the specimen edge all the way to the specimen center. The crack tip speed seems to increase as the distance from the specimen edge increases; it then decelerates at about 30 mm from the edge and then drastically accelerates to intersonic levels as the specimen centerline is approached, never exceeding $\sqrt{2}\ C_s^H$. The significance of the special speed $\sqrt{2}\ C_s^H$ is discussed by Lambros and Rosakis [29].

Based on experimental observations from your three different fields of view, the major dynamic failure modes and sequence in model three-layer materials can be

summarized in Figure 12. After the stress wave reaches the free edges, two shear-dominated inter-layer cracks initiate and propagate towards the specimen center. These shear cracks separate the whole lower interface and a Rayleigh surface wave forms on the separated free surface. This wave splits into two and travels from the specimen center to the edges. At a later stage, inter-layer cracks also originate from the upper interface at the free edge and travel towards the specimen center. However, these upper inter-layer cracks soon kink into the core layer to form opening-dominated intra-layer cracks. Under certain circumstances (e.g., if the core material is very brittle), such kinked cracks may also branch into a fan of multiple branches fragmenting the core. The model experiments described here seem to capture the basic nature of the post-mortem impact failure modes observed in real sandwich structures. Indeed, the kinked matrix crack of the core layer of the glass fiber/foam core sandwich shown in Figure 12 (e) seems to follow the same initiation and propagation process as the kinked intra-layer crack in the model three-layer specimens schematically shown in Figure 12 (d). Actually, the so-termed "shear matrix cracks" or "shear core cracks" discussed in post-mortem studies of failure in composite or sandwich structures [4,36-37] are instead opening-dominated, as clearly seen by the optical patterns of Figures 8 (e) and 9 (f) and, as such, they are inappropriately named.

I-3.2 Failure process in type B specimens (short sandwich style specimens)

Figure 13 shows a photoelasticity sequence of photographs corresponding to a type B specimen with thin metal layers. This type of specimen is quite similar to a real sandwich structure in terms of the thickness ratio of the faceplate to core. The field of view on the specimen edge is shown in Figure 13 (a). The failure process in this type of

specimens is quite similar to the process observed in type A specimens, summarized in the previous section. The failure mode occurring first is still the inter-layer crack at the lower interface. However, when the impact speed is lower (here is 10m/s compared to 33m/s in the previous case), this inter-layer crack initiates very late as shown in Figure 13 (c). The crack tip speed history of the inter-layer crack is shown in Figure 13 (e) as a function of time. The crack initiates at a high subsonic speed at around 600 m/s and accelerates monotonically to a value close to the Rayleigh wave speed of Homalite-100. In part II of this investigation [25], we briefly study the effects of impact speed and interfacial bond strength on the speed of such inter-layer cracks.

I-3.3 Failure process in type C specimens (long sandwich style specimens)

In types A and B specimens, inter-layer cracks always initiated from the specimen free edges due to the stress concentration at such locations. In order to study the impact damage modes and failure sequence in either very large structures or ones that are clamped along the edges, our model specimens featured long specimens. These specimens were long enough such that any damage from the edges, such as inter-layer cracks induced by the edge effect, arrived in the area of observation long after the local damage sequence had been completed near the impact point. To study this effect, we tested long sandwich style specimens of type C (see Figure 14). As shown in Figure 14 (d), at 79 μs after impact, an inter-layer crack tip is seen at the lower interface (fringe concentration within the dashed circle). This crack is similar in nature to our previously observed inter-layer fractures but has not originated at the specimen free edge, which for type C specimens is far away from our field of view. Indeed, if this crack originated from

the specimen free edge, it would take at least 150 μs to enter the field of view. Closer scrutiny reveals that this crack originates from a much closer location to the impact point. This location is marked here by the circle in Figure 14 (c) within which a concentration of photoelastic fringes points to the concentration of shear stresses that is responsible for its nucleation. Indeed the crack nucleates at a location where the inter-layer shear stress reaches a local maximum, whose value equals the shear strength of the bond. To rationalize this, one should consider the symmetry of our impact configuration and recall the strong wave speed mismatch between the lower faceplate and the core material. The shear stress component σ_{12} at the specimen centerline will always vanish because of this symmetry but is expected to anti-symmetrically increase away from the centerline as compressive waves begin to spread along the steel faceplate. A simple wave diagram showing the creation of intense shearing along the lower interface because of the wave speed mismatch is shown in Figure 15. The diagram clearly shows that as points P_1 and P_2 move symmetrically away from the centerline, they load it in a combination of compression and shear. This combination is what is needed to generate the intersonic shear-dominated inter-layer cracks that are consistently observed throughout this work and are similar to the original bimaterial studies of Lambros and Rosakis [29], subsequently analyzed by Needleman and Rosakis [32]. If the impact speed is high enough, or the specimen is long enough, there would be a time when the shear stresses at P_1 and P_2 will reach a critical level, high enough to nucleate two inter-layer cracks before either P_1 or P_2 reach the specimen edges. If on the other hand, the impact speed (and thus the magnitude of the induced interfacial shear) is not very high, then shear delamination would not occur until P_1 and P_2 reach the edges where the shear stresses will be amplified

by the edge singularity to cause delamination. It is this later case which dominated the failure behavior in the "short" type A and B specimens. The hypothesis presented above is indeed consistent with the previous finite element analyses of composite laminates subjected to out-of-plane impact [7,12], where two clear peak values (same magnitude) of the interlaminar shear stress were shown to symmetrically move away from the impact site (i.e., the specimen center, where the interlaminar shear stress is zero according to geometrical symmetry). Of course, the amplitude of these peaks depends strongly on the impact speed and on the stress wave mismatch between faceplates and core materials. As a result of these observations, the scenario that seems to be emerging is as follows: shear-dominated cracks are generated at two points to the right and left of the center line and more backwards towards the impact point. A series of photographs confirming the existence of an inter-layer crack coming from the right-hand side of the impact point is shown in Figure 14. Indeed Figure 14 (c) corresponds to the nucleation of this crack while Figures 14 (d) (e) and (f) confirm its high-speed motion towards the impact site. As this inter-layer crack and its symmetric companion from the left meet above the impact point, they create a central shear delamination between the core and the bottom faceplate. The speed of this crack is very high as evident from the shear shock wave that appears as a dark inclined line radiating from its moving tip (Figures 14 (e) and (f)). This is confirmed by the crack length and speed histories shown in Figure 16.

Figure 17 corresponds to another impact experiment which featured the same load condition as shown in Figure 14. The end point of the central delamination described above is denoted by A. Figure 18 shows the variations of the inter-layer shear and normal stress at the interface of this model sandwich specimen simulated by Yu et al. [38]. As

shown in Figure 18, the inter-layer normal stresses near the impact point are compressive while the inter-layer shear stresses exhibit two clear peak values (same magnitude) moving symmetrically away from the centerline. Point A in Figure 17 is corresponding to the old location of the maximum inter-layer shear stress. This point can now acts as a stress concentration from which further damage (to the core as well as to the rest of the interface) will subsequently evolve. Indeed as seen in Figure 17, intra-layer cracks now are generated and propagated into the core (along AC), also accompanied by a new inter-layer debond (along AB) also originating at point A. The high-speed snapshot that appears in the same photograph confirms this scenario. Figure 19 summarizes the proposed failure evolution sequence for the long sandwich style specimens described above. One point that should be made clear here is that following the formation of the central (shear) delamination, the choice of the inclination angle β and the possibility of further delamination along the bottom interface depend on the impact speed and on the relative values of the matrix material and interfacial bond strengths. The same is true for the exact locations of points A and B. However, we expect that if impact speeds are high enough to promote this localized failure mode, the general features described here will continue appearing even as the projectile speed increases further. An extension of the present work concentrating on the effect of bond strengths and impact speeds on dynamic failure is presented in Part II of this investigation. For the initiation of intra-layer cracks (matrix cracks), previous researchers theorized that such cracks initiated from the center of the weak layer and propagated toward adjacent interfaces to lead to inter-layer cracks or delaminations [7,12,39]. However, no real-time experimental evidence was ever observed to support such a scenario. Here, we clearly show that the intra-layer cracks

always initiate at the interfaces immediately following the shear-dominated delamination fracture, which kinks into the core layer resulting in intra-layer core cracking.

I-4. Conclusions

In all cases described in this paper, inter-layer crack growth (delamination) is the dominant dynamic failure mode for layered materials and sandwich structures. These cracks appear to be shear-dominated and proceed with intersonic speeds. Intra-layer cracking always occurs soon after some amount of inter-layer delamination has already happened and proceeds through the spreading and branching of local mode I cracks into the core layer. Intra-layer or core cracking often initiates at the interface as a result of inter-layer crack kinking into the core. If the speed of the kinked intra-layer crack reaches a critical value, multiple crack branching may also occur inside the core layer. If free edge effects at the bimaterial corners are eliminated, the failure sequence is slightly modified. Specifically, the inter-layer cracks initiate from positions where the inter-layer shear stress reaches a local maximum equal to the shear strength of the bond. These cracks create a local shear driven delamination directly above the point of impact. Intra-layer cracks following this process also kink from these positions into the sandwich core.

Acknowledgements

The authors gratefully acknowledge the support of the Office of Naval Research (Dr. Y. D. S. Rajapakse, Project Monitor) through a grant (#N00014-95-1-0453) to Caltech. The assistance of Dr. Demir Coker and Dr. David Owen is greatly appreciated.

References

[1] Hutchinson J W, Suo Z. Mixed mode cracking in layered materials. Advances in Applied Mechanics 1998; 29:63-191.

[2] Rajapakse Y D S. Recent advances in composite research for marine structures. Sandwich Construction 3, Vol. II, 1998, pp. 475-486.

[3] Valenti M. Stealth on the water. ASME Mechanical Engineering 2001; 123:56-61.

[4] Abrate S. Impact on laminated composites: recent advances. Applied Mechanics Reviews 1994;47:517-544.

[5] Cantwell W J, Morton J. The impact resistance of composite materials—a review. Composites 1991;22:347-362.

[6] Mines R A W, Roach A M, Jones N. High velocity perforation behaviour of polymer composite laminates. International Journal of Impact Engineering 1999;22 (6):561-588.

[7] Sun C T, Rechak S. Effect of adhesive layers on impact damage in composite laminates. In:Whitcomb JD, editor. Composite materials: testing and design (eighth conference). ASTM STP 972, American Society for Testing and Materials, Philadelphia, 1988; 97-123.

[8] Gioia G, Ortiz M.. Delamination of compressed thin films. Advances in Applied Mechanics 1997;33:119-192.

[9] Vizzini A J, Lagace P A. The buckling of a delaminated sublaminate on an elastic foundation. Journal of Composite Materials, 1987;21:1106-1117.

[10] Kadomateas G A. Post-buckling and growth behavior of face-sheet delaminations in sandwich composites. AMD-Vol. 235, Thick Composites for Load Bearing Structures, (Y.D.S. Rajapakse and G.A. Kadomateas, Ed.) 1999;51-60.

[11] Wu H T, Springer G S. Measurements of matrix cracking and delamination caused by impacted on composite plates. J. of Composite Materials 1988;22:518-532.

[12] Choi H Y, Wu H T, Chang F.-K. A new approach toward understanding damage mechanisms and mechanics of laminated composites due to low-velocity impact : part II—analysis. J. Composite Materials 1991;25:1012-1038.

[13] Lambros J, Rosakis A J. An experimental study of the dynamic delamination of thick fiber reinforced polymeric matrix composite laminates. Experimental Mechanics 1997;37:360-366.

[14] Lee J.-W, Daniel I M. Progressive transverse cracking of crossply composite laminates. J. Composite Materials 1990;24:1225-1243.

[15] Karandikar P, Chou T.-W. Characterization and modeling of microcracking and elastic moduli changes in nicalon-CAS composites. Comp Sci Tech. 1992;46: 253.

[16] Shenoy V B, Schwartzman A F, Freund L B. Crack patterns in brittle thin films. International J. of Fracture 2000;103:1-7.

[17] Hahn H T, Williams J G. Compression failure mechanisms in unidirectional composites. Composite Materials: Testing and Design (7th Conf.), ASTM STP 893, J.M. Whitney, Ed., American Society for Testing and Materials, 1986;115-139.

[18] Oguni K, Tan C Y, Ravichandran G. Failure mode transition in unidirectional E-Glass/Vinylester composites under multiaxial compression. J. of Composite Materials 2000;34:2081-2097.

[19] Ju J W. A micromechanical damage model for uniaxially reinforced composites weakened by interfacial arc microcracks. J. of Appl Mech 1991;58:923-930.

[20] Takeda N, Sierakowski R L, Ross C A, Malvern L E. Delamination-crack propagation in ballistically impacted glass/epoxy composite laminates. Experimental Mechanics 1982;22:19-65.

[21] Li X, Carlsson L A. The tilted sandwich debond (TSD) specimen for face/core interface fracture characterization. Journal of Sandwich Structures and Materials 1999;1(1):65-75.

[22] Semenski D, Rosakis A J. Dynamic crack initiation and growth in light-core sandwich composite materials. Proceedings of the 17th Danubia-Adria Symposium on Experimental Mechanics in Solid Mechanics, Prague, 1999;297-300.

[23] Riley W F, Dally J W. A photoelastic analysis of stress wave propagation in a layered model. Geophysics 1966;31:881-99.

[24] Walter M E, Ravichandran G. Experimental simulation of matrix cracking and debonding in a model brittle matrix composite. Experimental Mechanics. 1997;37:130—135.

[25] Xu L R, Rosakis A J. Impact failure characteristics of sandwich structures; part II: effects of impact speeds and interfacial bonding strengths. In preparation (2001).

[26] Parameswaran V, Shukla A. Dynamic fracture of a functionally gradient material have discrete property variation. J. of Material Science 1998;33:3303-3311.

[27] Rosakis A J, Samudrala O, Singh R P, Shukla A. Intersonic crack propagation in bimaterial systems. Journal of the Mechanics and Physics of Solids 1998;46:1789-1813.

[28] Dally J W. Dynamic photoelastic studies of fracture. Experimental Mechanics, 1979;19:349-61.

[29] Lambros J, Rosakis A J. Shear dominated transonic growth in a bimaterial –I. experimental observations. J. Mech Phys Solids 1995;43:169-188.

[30] Singh R P, Shukla A. Subsonic and intersonic crack growth along a bimaterial surface. Journal of Applied Mechanics 1996;63:919-924.

[31] Xu L R, Rosakis A J. An experimental study on impact-induced failure events in homogeneous layered materials using dynamic photoelasticity and high-speed photography. Submitted to Optics and Lasers in Engineering (2001).

[32] Needleman A, Rosakis A J. The effect of bond strength and loading rate on the conditions governing the attainment of intersonic crack growth along interfaces. J. Mech Phys Solids 1999;47:2411-2449.

[33] Ravi-Chandar K, Knauss W G. An experimental investigation into dynamic fracture: III. on steady-state crack propagation and crack branching. International J. of Fracture 1984;26:141-54.

[34] Vinson J R, Sierakowski R L. The behavior of structures composed of composite materials. Martinus, Nijhoff Publishers, Dordrecht (1986).

[35] Williams M L. Stress singularities resulting from various boundary conditions in angular corners in extension. J. Applied Mechanics 1952;19:526-528.

[36] Wen H M, Reddy T Y, Reid S R, Soden P D. Indentation, penetration and perforation of composite laminates and sandwich panels under quasi-Static and projectile loading, Key Engineering Materials 1998;141-143:501-552.

[37] Karbhari V M, Rydin R W. Impact characterization of RTM composites—II: damage mechanisms and damage evolution in plain weaves. J. of Material Science 1999;34:5641-5648.

[38]. Yu C, Ortiz M. Pandolfi A. Rosakis A. Private communications. 2001.

[39] Geubelle P H, Baylor J S. Impact-induced delamination of composites: a 2D simulation. Composites Part B 1998;29B:589-602.

List of table

List of figures

Figure 9. An edge view of damage evolution. Inter-layer delaminations are shown to form at the intersection of, first lower, and then upper interfaces with the specimen edge. A fan of kinked intra-layer cracks branches into the core layer from the upper interface.

Figure 10. Crack speed history (a) of two inter-layer cracks and crack length (b) history of the lower inter-layer crack. Cs and C_R are the shear wave and Rayleigh wave speeds of the Homalite-100.

Figure 11. Crack speed distribution as a function of distance from the specimen edge. Results from three experiments under the same conditions are shown.

Figure 12. Conceptual summary of typical failure modes and sequence in a short three-layer specimen with equal layer widths. Figure (e) is a comparison with a post-impact picture of a real sandwich specimen.

Figure 13. Inter-layer crack initiation and propagation at the lower interface of a model sandwich-style specimen (type B specimens).

Figure 14. Nucleation of an intersonic inter-layer crack at the vicinity of the impact area. The specimen (type C specimens) is long enough to eliminate the edge interference.

Figure 15. Crack length history (a) and crack speed history (b) of the lower interfacial crack nucleated at the central part of a long model sandwich specimen.

Figure 16. Wave diagram (b) and picture demonstrating the mechanism of compression/shear loading of the lower interface of a sandwich structure subjected an impact loading at the center of lower faceplate.

Figure 17. Local view of the post-mortem damage in a long sandwich-style specimen (a) and high-speed snap shot capturing the formation of intra-layer cracks (b).

Figure 18. Variations of inter-layer normal and shear stress along the interface of a long sandwich style specimen after impact (Yu and Ortiz).

Figure 19. Failure sequence observed in long sandwich-style specimens with minimal edge effects.

Table 1. Material properties used in model experiments

Property	Homalite 100		Steel 4340
	static	Dynamic*	Static
Young's Modulus E (GPA)	3.9	5.3	208
Poisson's Ratio ν	0.35	0.35	0.3
Dilatational wave speed c_l (m/s) (plane stress)	1890	2119	5500
Shear wave speed c_s (m/s)	1080	1208	3320
Rayleigh wave speed c_r (m/s)	1010	1110	2950
Density ρ (kg/m^3)	1230	1230	7830

*Dynamic properties correspond to an average equivalent strain rate of 10^3 /s.

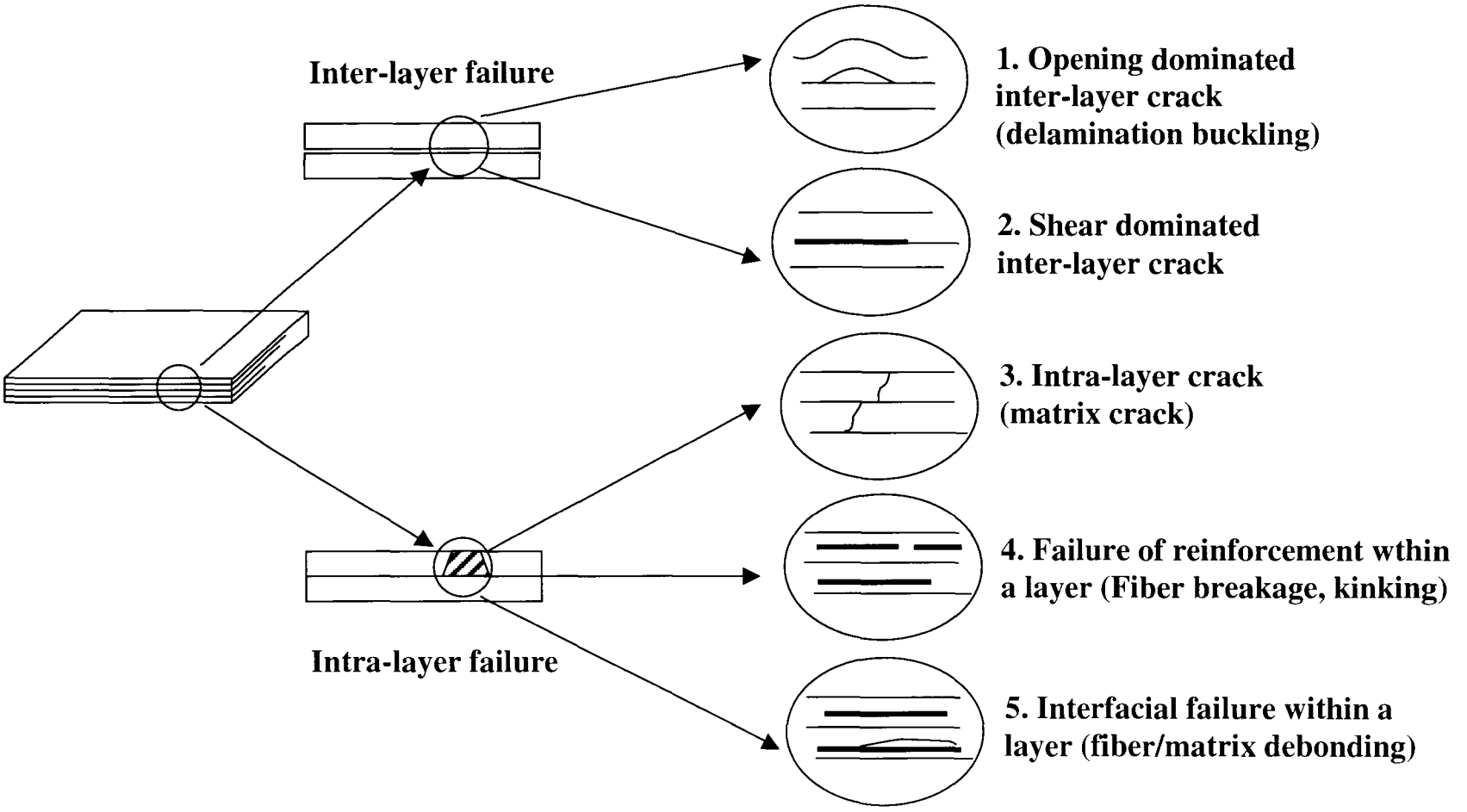

Figure 1. Possible failure modes for layered materials based on material constitution

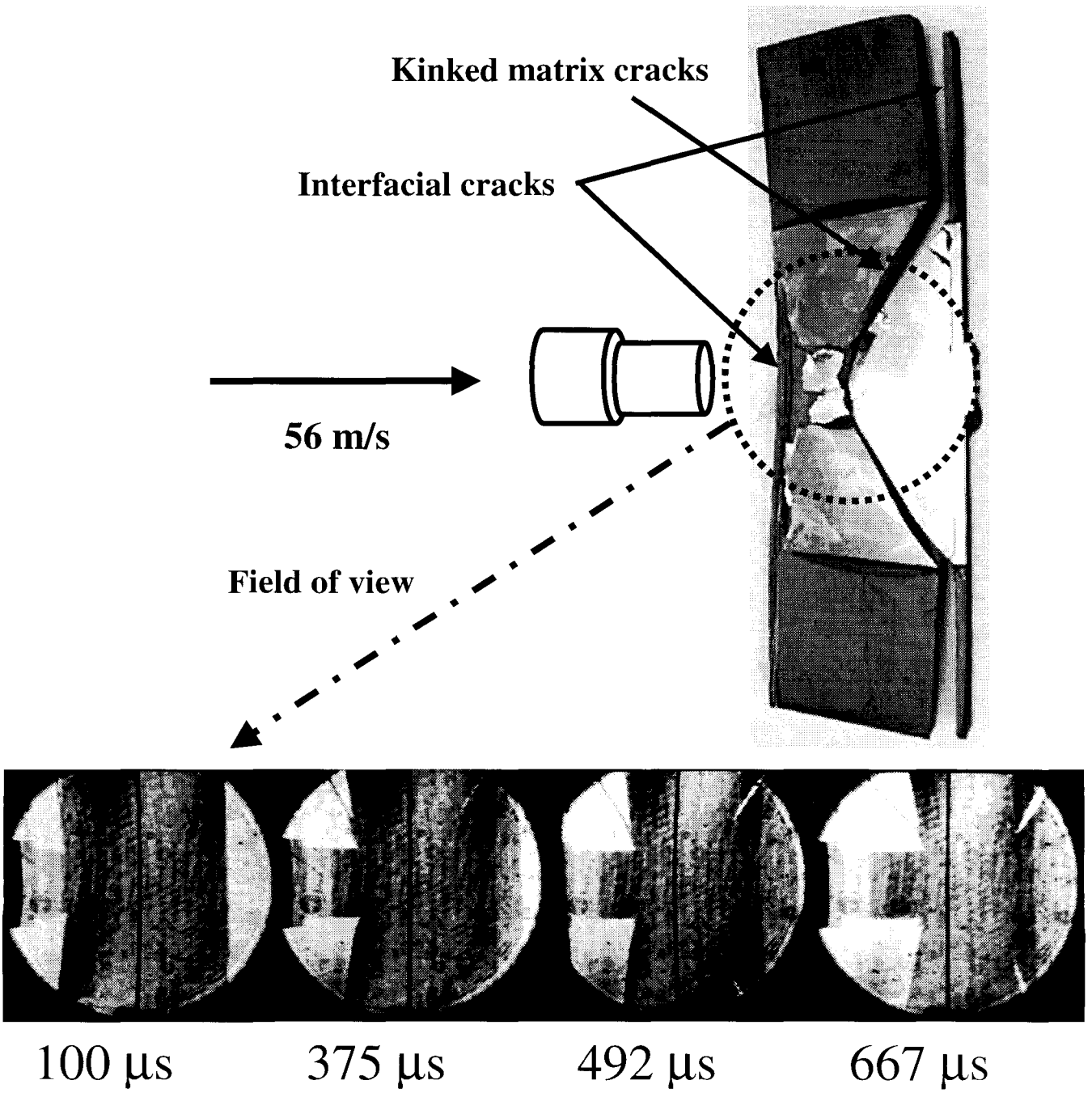

Figure 2. A series of back lit photos showing the dynamic failure process for a fiberglass face plates /PVC foam core sandwich structure.

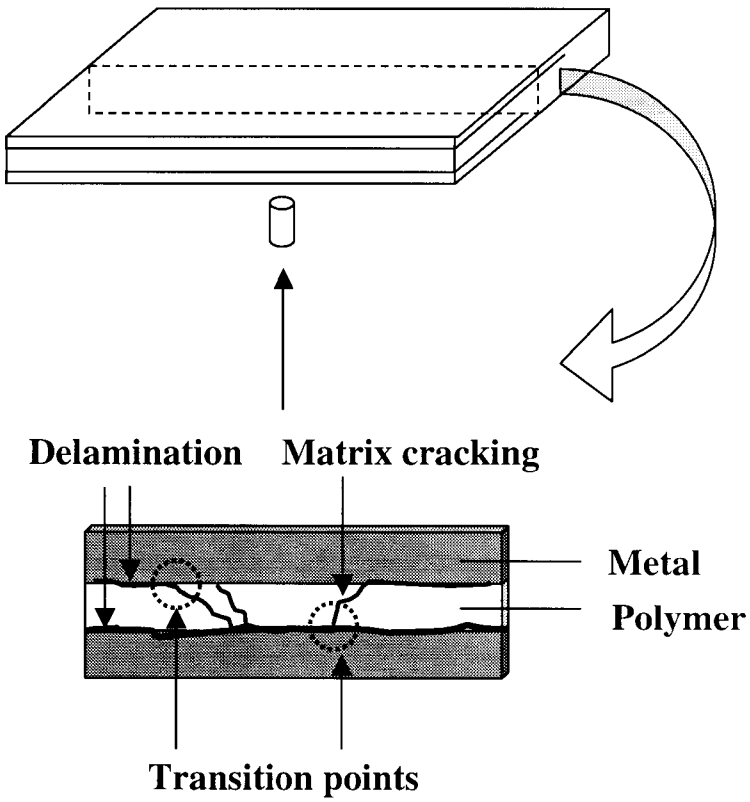

Figure 3. Model layered specimens are idealized cross sections of real structure subjected to out-of-plane impact

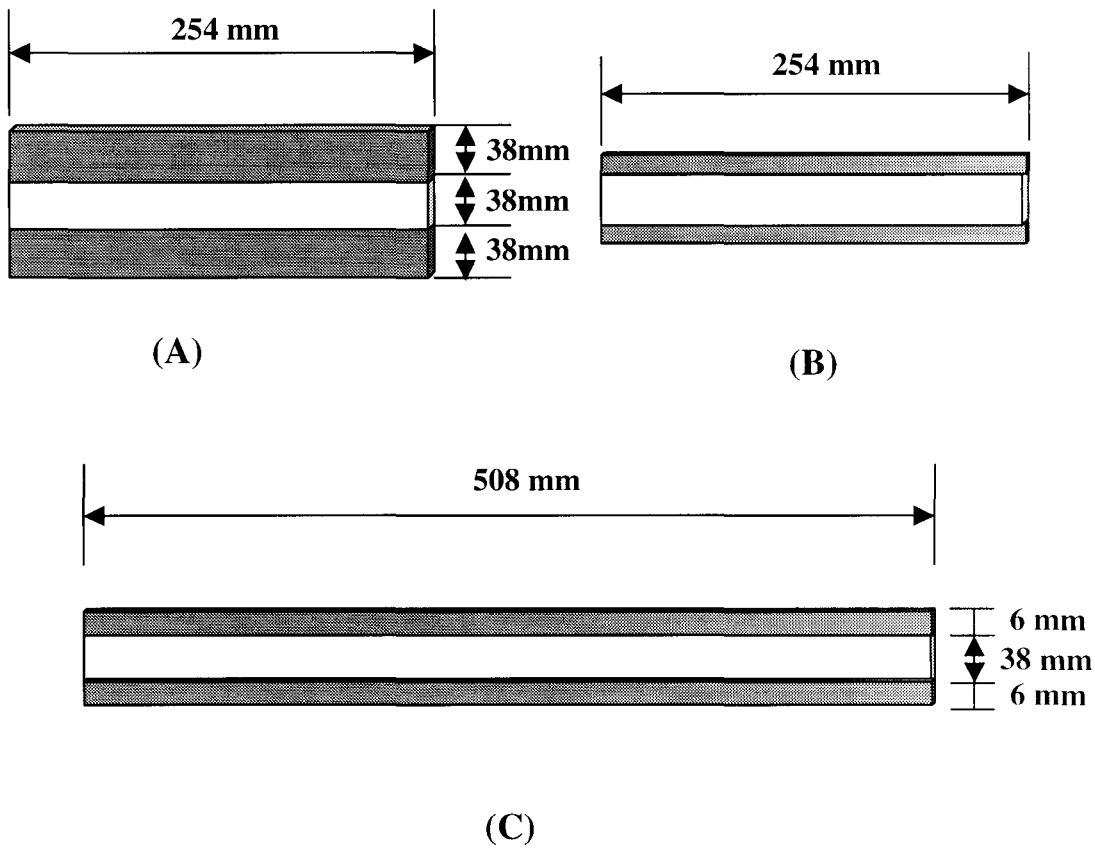

Figure 4. Model specimens simulating sandwich structures
(shaded layers—metals; transparent layers---polymers)

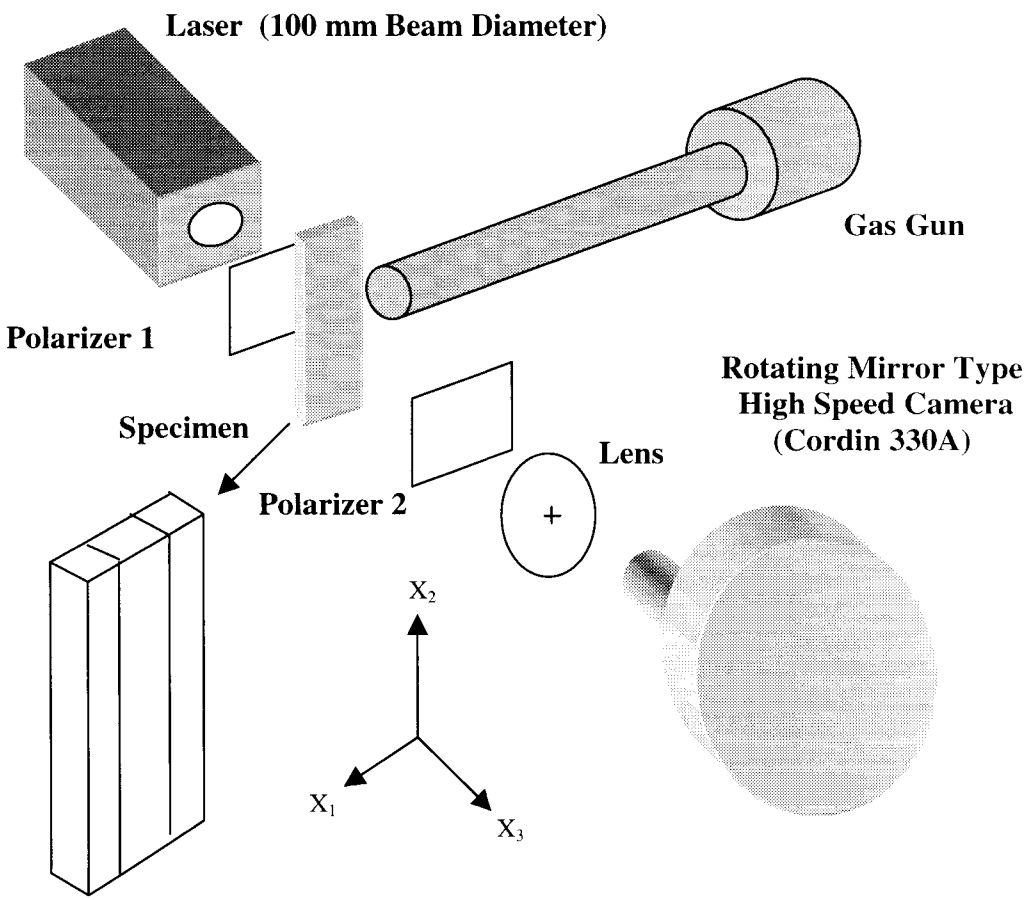

Figure 5. Schematic of the dynamic photoelasticity setup

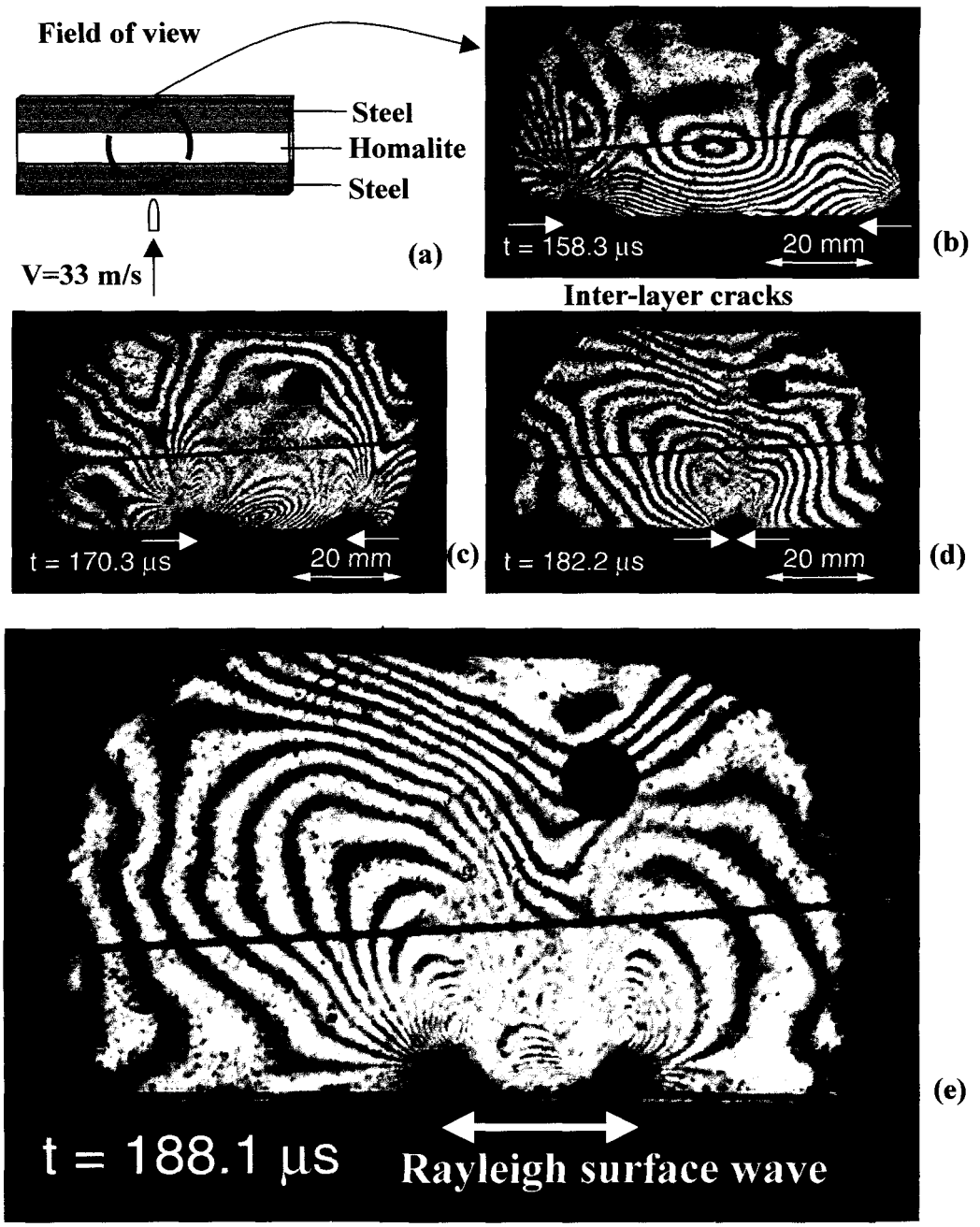

Figure 6. Early stages of the failure process of a three-layer specimen with equal layer widths. The central field of view reveals the early occurrence of shear-dominated delamination at the lower interface. At later times (Figures e), the debonding becomes clearly visible at the lower interface.

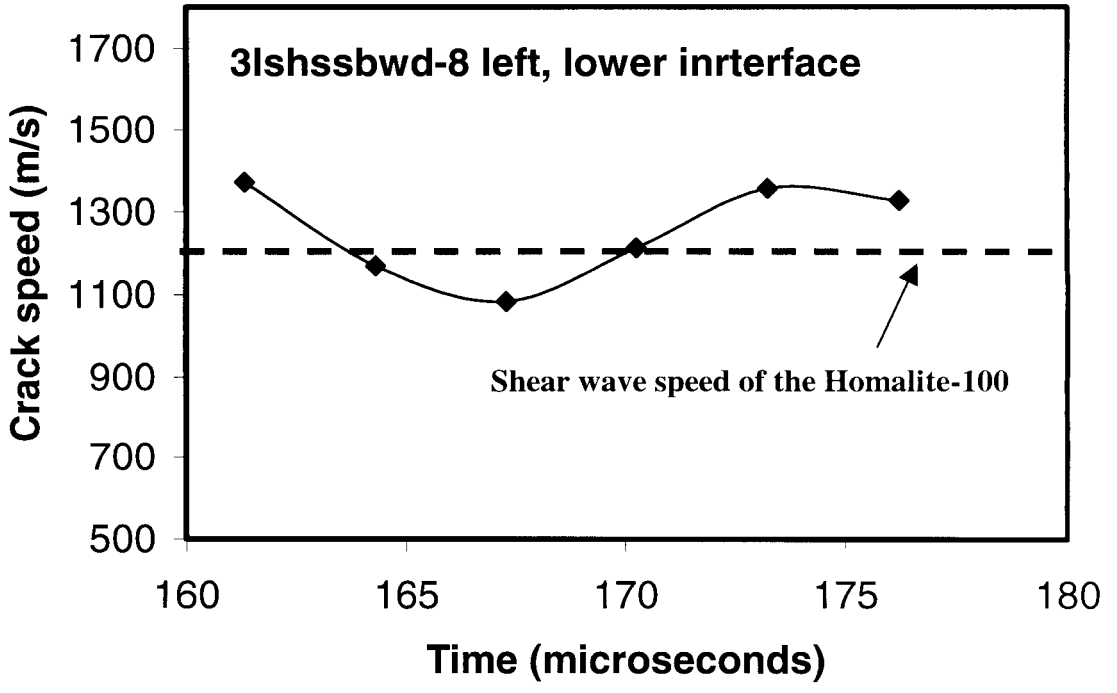

Figure 7. Crack speed history of one of the two inter-layer cracks at the lower interface

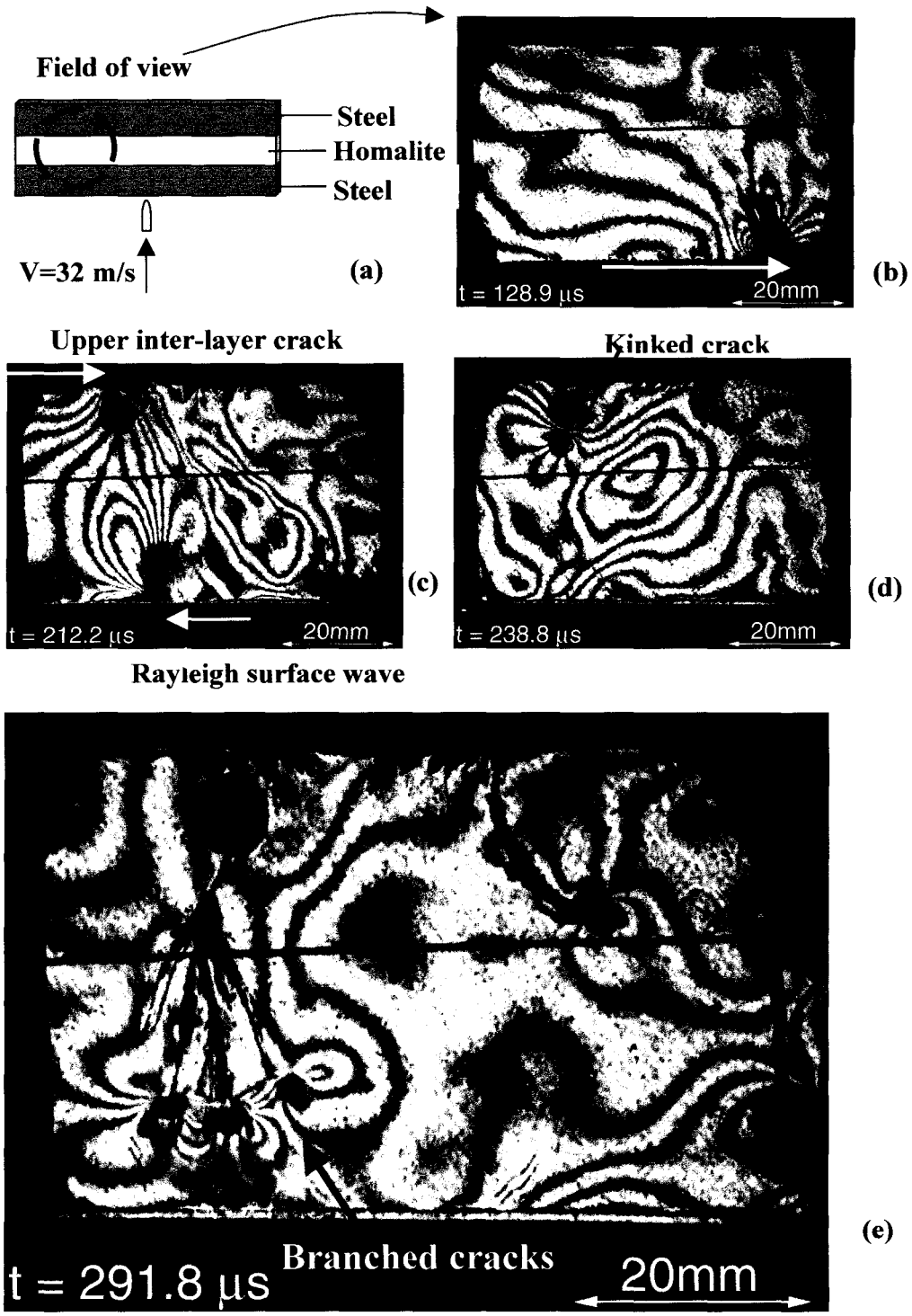

Figure 8. Dynamic failure modes and sequence in a layered specimen from a different field of view. Following interfacial delamination at the lower then the upper interfaces, cracks kink into the core layer to form intra-layer damage.

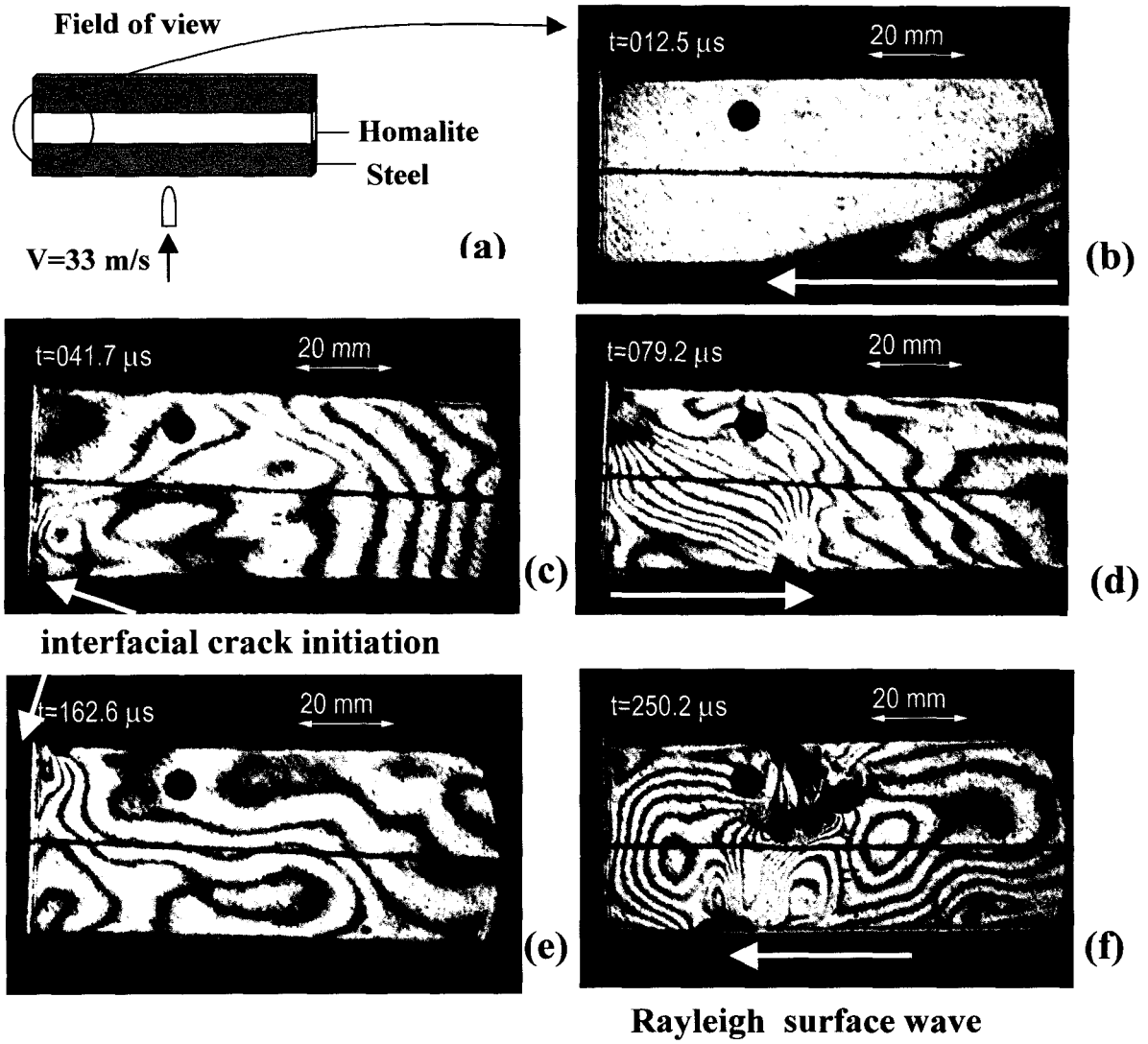

Figure 9. An edge view of damage evolution. Inter-layer delaminations are shown to form at the intersection of, first lower, and then upper interfaces with the specimen edge. A fan of kinked intra-layer cracks branches into the core layer from the upper interface.

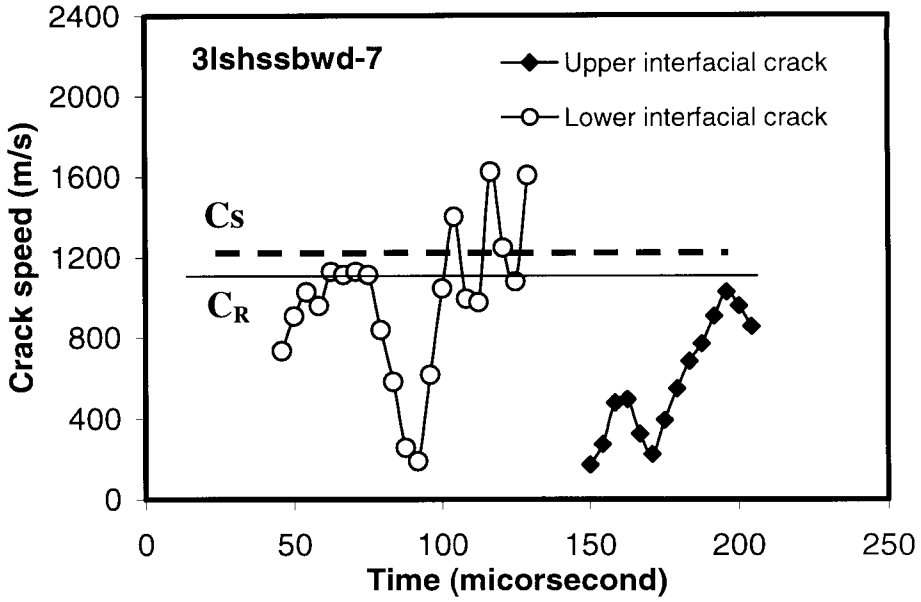

(a)

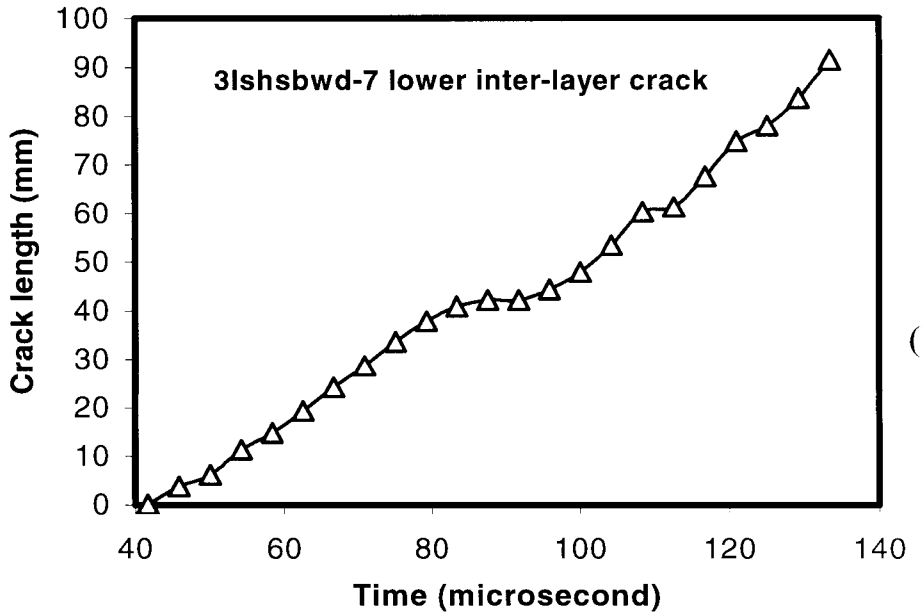

(b)

Figure 10. Crack speed history (a) of two inter-layer cracks and crack length (b) history of the lower inter-layer crack. Cs and C_R are the shear wave and Rayleigh wave speeds of the Homalite-100.

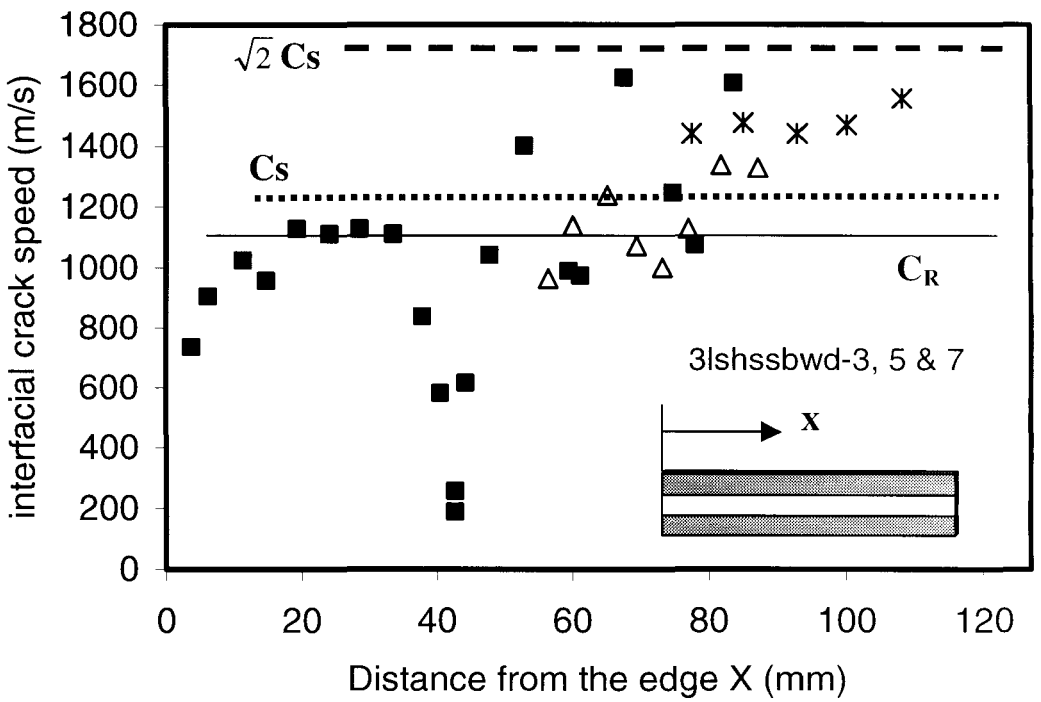

Figure 11. Crack speed distribution as a function of distance from the specimen edge. Results from three experiments under the same conditions are shown.

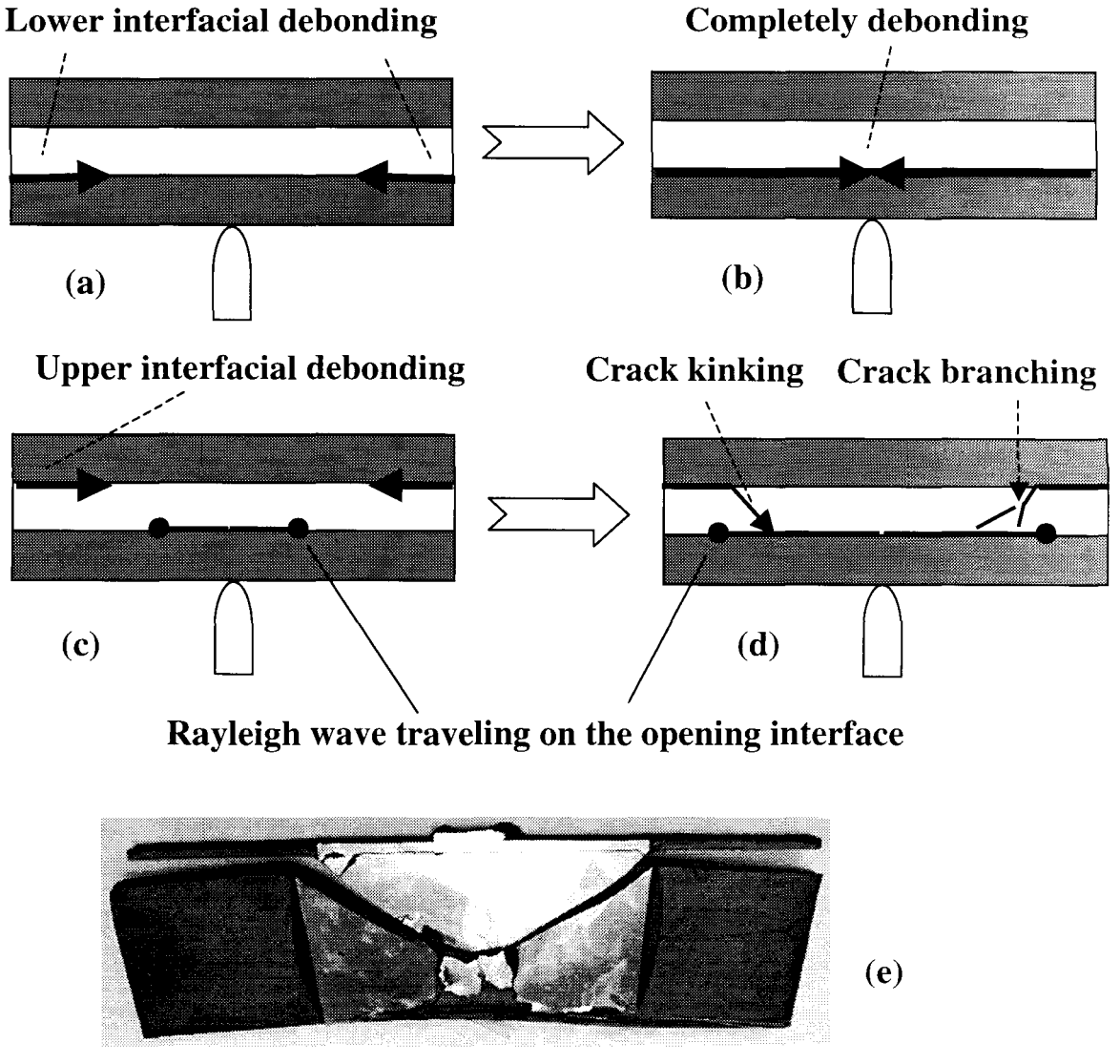

Figure 12. Conceptual summary of typical failure modes and sequence in a short three-layer specimen with equal layer widths. Figure (e) is a comparison with a post-impact picture of a real sandwich specimen.

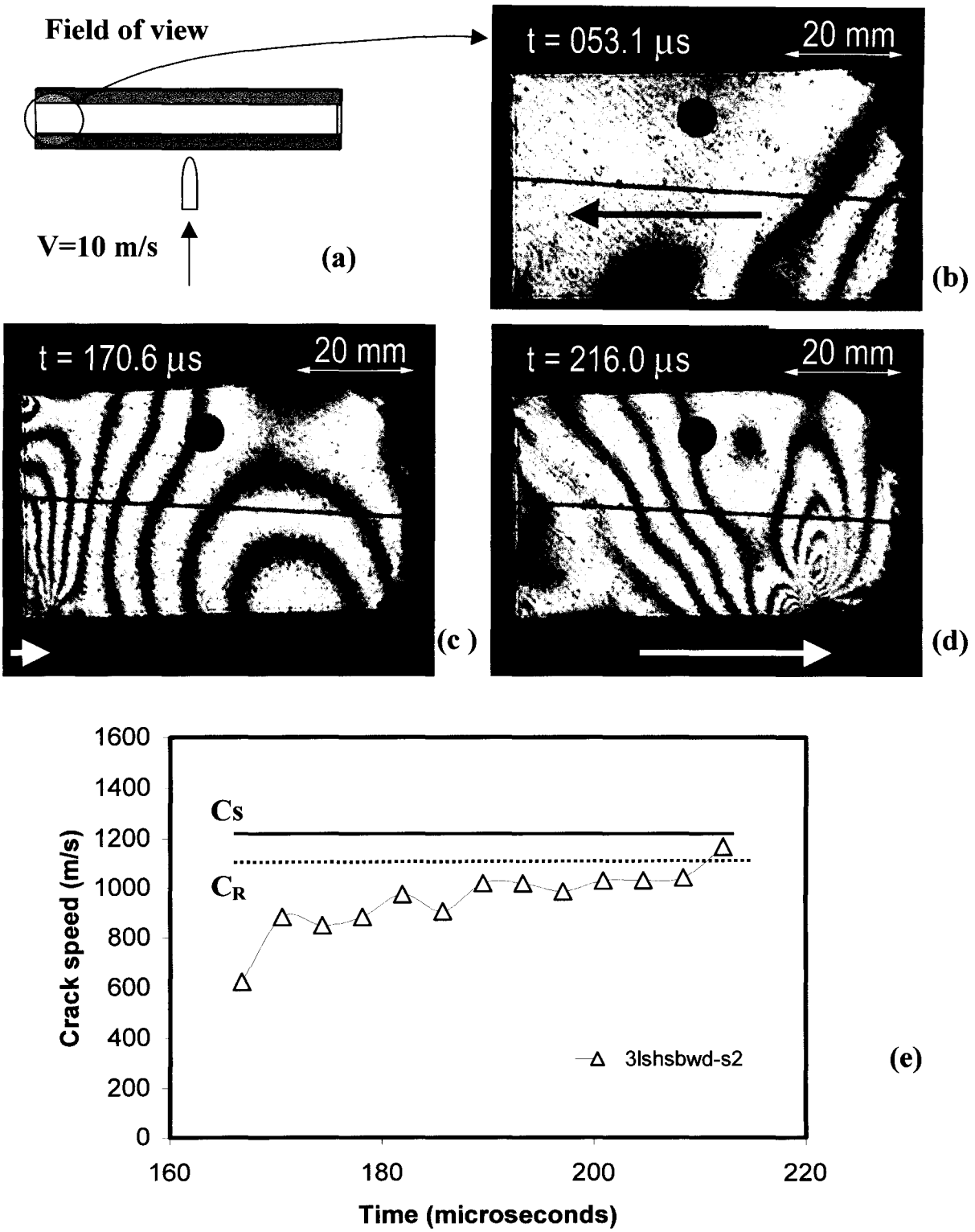

Figure 13. Inter-layer crack initiation and propagation at the lower interface of a model sandwich-style specimen (type B specimens)

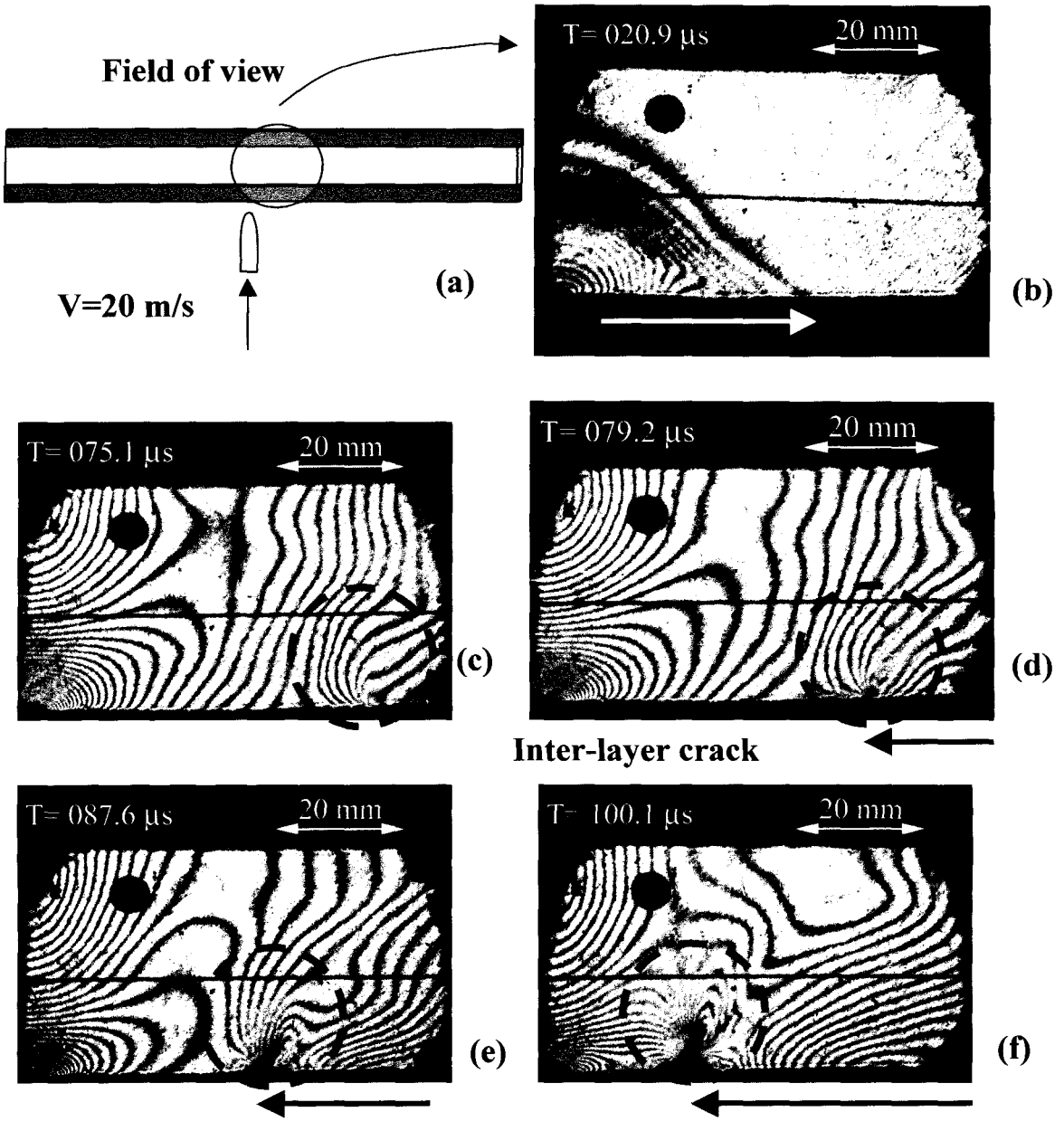

Figure 14. Nucleation of an intersonic inter-layer crack at the vicinity of the impact area. The specimen (type C specimens) is long enough to eliminate the edge interference.

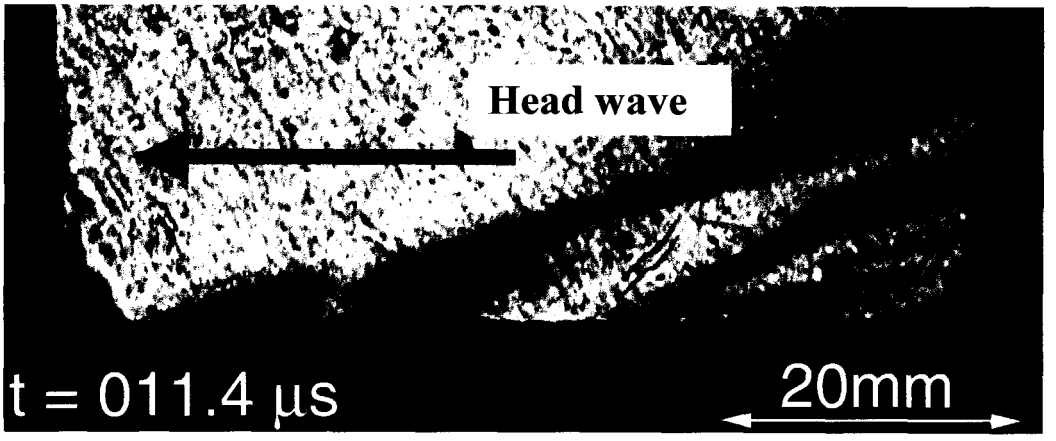

(a)

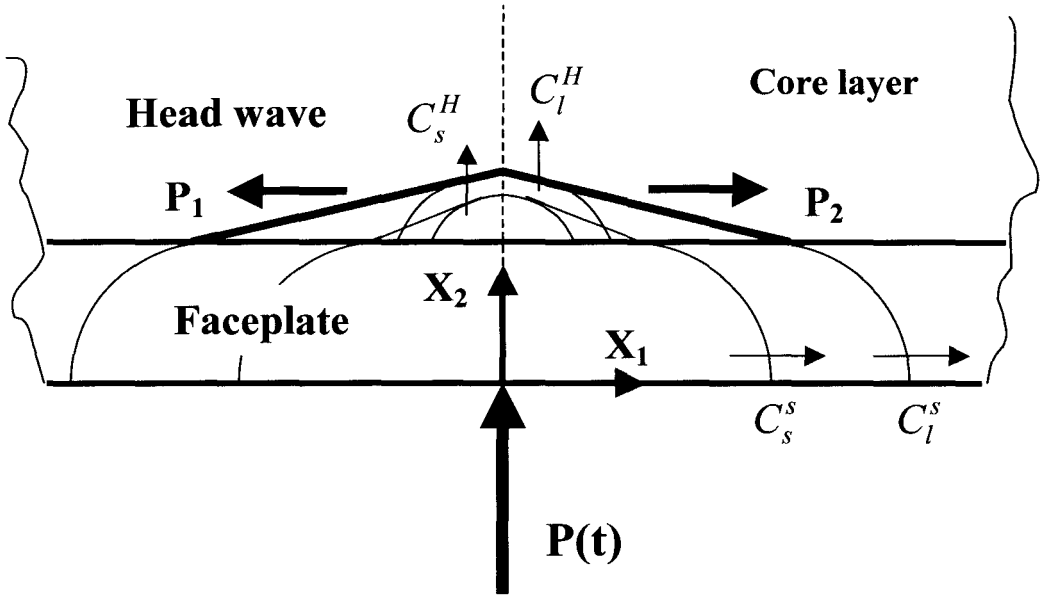

(b)

Figure 15. Wave diagram (b) and picture demonstrating the mechanism of compression/shear loading of the lower interface of a sandwich structure subjected an impact loading at the center of lower faceplate.

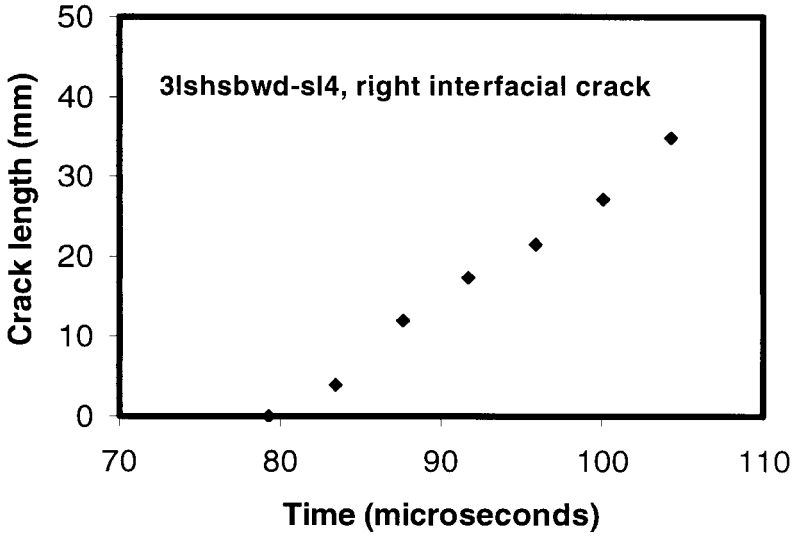

(a)

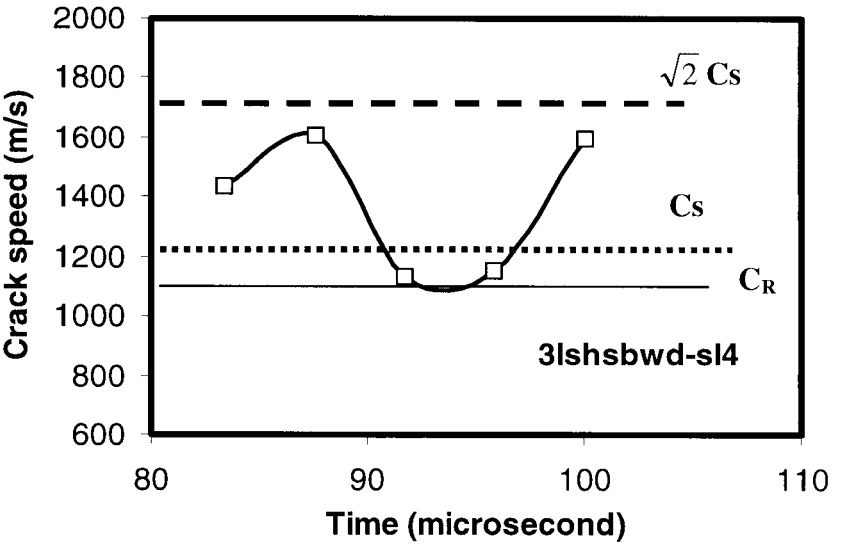

(b)

Figure 16. Crack length history (a) and crack speed history (b) of the lower interfacial crack nucleated at the central part of a long model sandwich specimen.

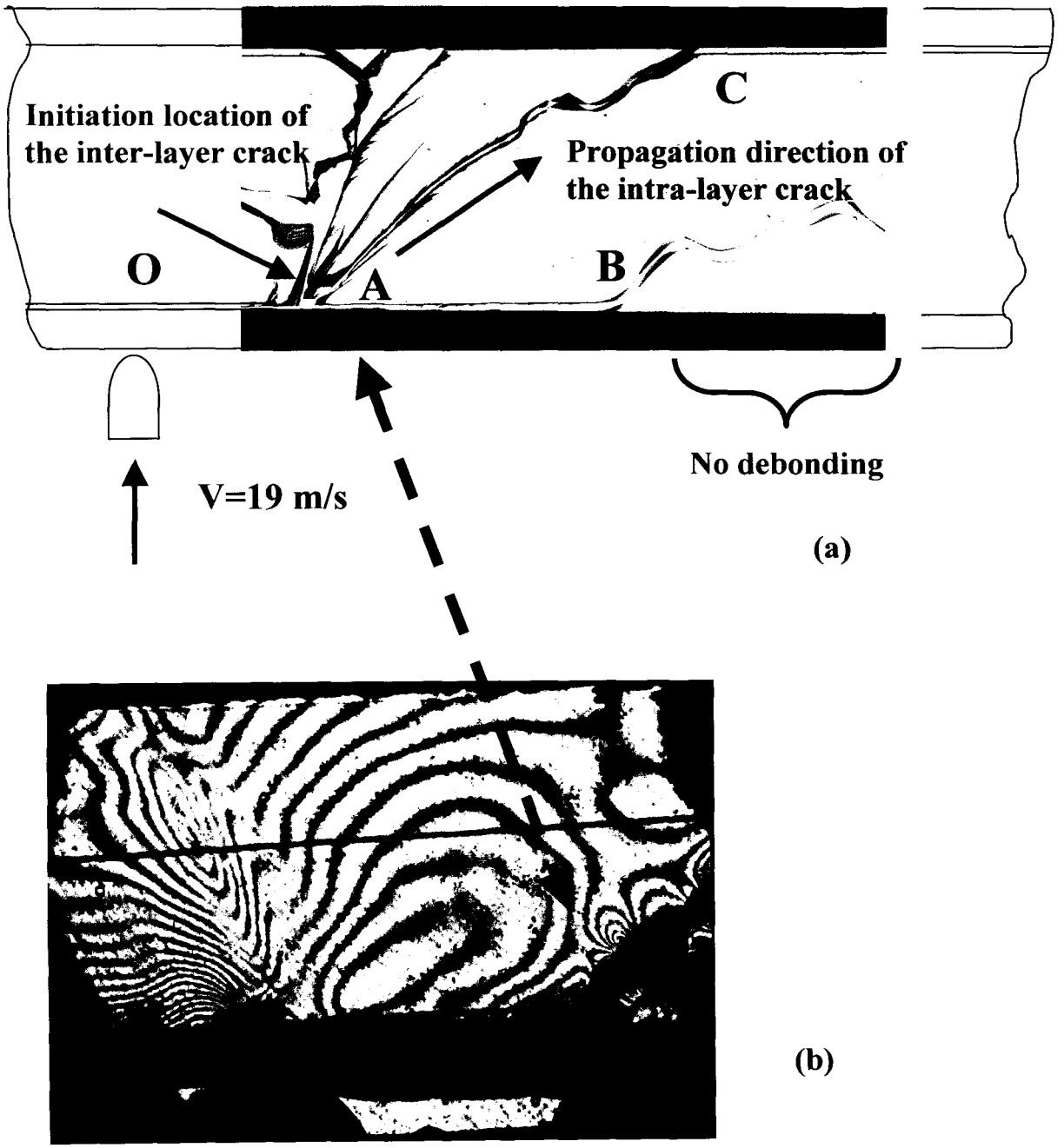

Figure 17. Local view of the post-mortem damage in a long sandwich-style specimen (a) and high-speed snap shot capturing the formation of intra-layer cracks (b).

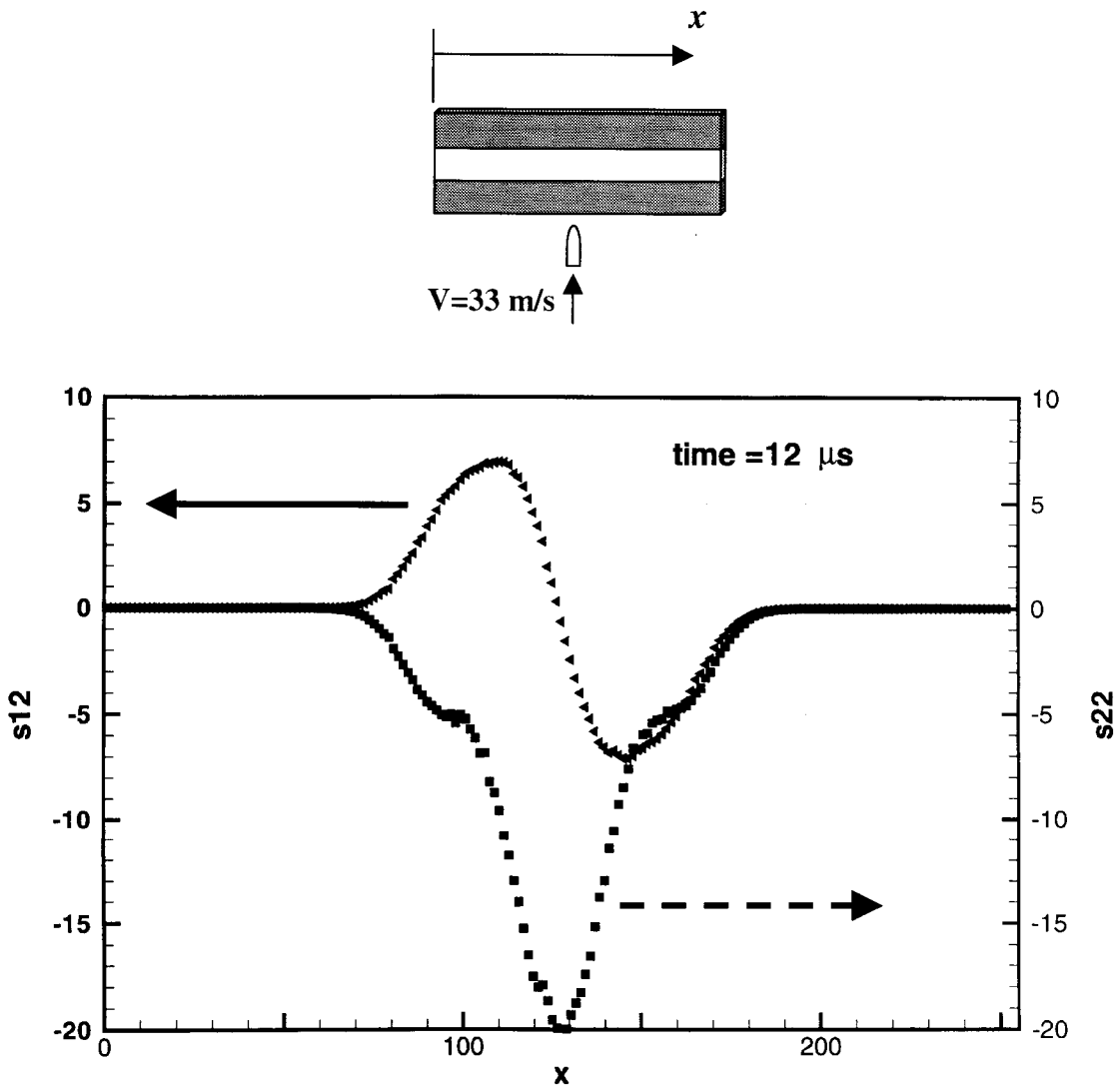

Figure 18. Variations of inter-layer normal and shear stress along the interface of a long sandwich style specimen after impact (Yu and Ortiz).

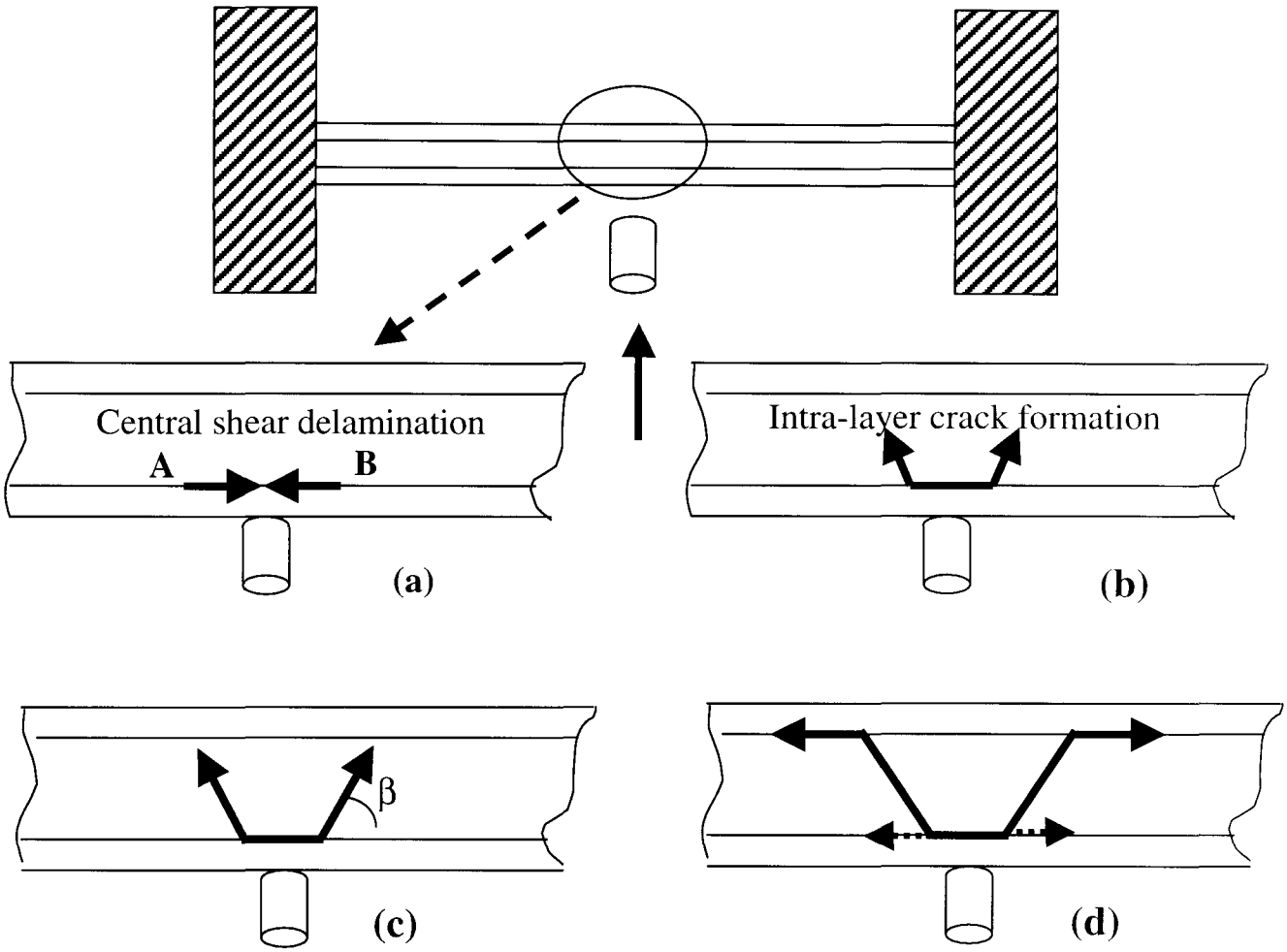

Figure 19. Failure sequence observed in long sandwich-style specimens with minimal edge effects.

Chapter II

Impact Failure Characteristics in Sandwich Structures; Part II: Effects of Impact Speed and Interfacial Strength

Abstract

In this paper, we describe the second part of an experimental investigation concentrating on the study of the effects of impact speed and interfacial bond strength on the dynamic failure of model sandwich structures. Results show that even small variations in impact speed and bond strength substantially influence the initiation behavior of delamination (location and nucleation time) and lead to substantially different inter-layer crack speed histories. These changes in inter-layer failure history influence the timing, sequence and final extent of subsequent intra-layer damage within the sandwich structures.

II-1. Introduction

In Part I of this investigation, we have presented and discussed the basic nature and sequence of failure modes in simple layered materials and sandwich structures [1]. Results show, that although the dominant failure mechanisms remain unchanged, their sequence and interaction may be strong functions of specimen geometry. Indeed, inter-layer cracking followed by intra-layer cracking remain the two major mechanisms of dynamic failure. One of the major conclusions of Part I of this study is that shear-dominated inter-layer (or interfacial) cracks are the ones that initiate first and that such

cracks grow very dynamically, their speeds and shear nature being enhanced by the large wave mismatch between the core and the faceplates. It is the kinking of these cracks into the sandwich core that triggers the complex mechanism of intra-layer failure. It is perhaps intuitively expected that the bond strength between the faceplates and the core as well as the magnitude of the impact pulse will influence the growth characteristics (initiation time and speed) of the interfacial fractures and thus will influence the subsequent failure history.

In the past years, dynamic interfacial failure in simple metal/polymer systems has received considerable attention because of its unique characteristics [2-4]. Early studies revealed that dynamic interfacial cracks are shear-dominated, are often intersonic and they seem to propagate stably and at discreet speeds that are dictated by multiples of the shear wave speed of the slower wave speed constituent of the bimaterial (e.g., Cs). Samudrala and Rosakis [5], Needleman and Rosakis [6] also showed that if the interfacial bond strength is changed, the initiation, transition and final choice of stable propagation speeds of interfacial cracks are also dramatically altered. Meanwhile, if the external loading is changed, i.e., the impact speed or pulse duration is altered, significant interfacial crack speed variations were also observed [5]. In a recent paper on the impact of laminated and assembled composite plates, Liu et al. [7] showed that the interface bond strength plays an important role in determining impact resistance.

Based on these preliminary results of the effects of impact speed and interfacial strength on interfacial cracks in simple systems, we try to understand the influence of these important parameters on the impact failure in more complex layered materials and sandwich structures. The major objective of this investigation is to study the effects of

different interfacial strengths, impact speeds and projectile lengths (hence impact momentum and energy) on inter-layer crack initiation and propagation and on the subsequent transition to intra-layer core damage.

II-2. Description of experiments

A gas gun impact set up, along with the high-speed photography and photoelasticity arrangements described in Part I of this study, were employed to investigate the dynamic failure phenomenon [1]. In order to compare different impact speeds and interfacial strengths, one baseline specimen geometry is chosen, i.e., the short three-layer specimen with equal layer widths (type A specimens in Part I) with two Weldon-10 strong bonds. The baseline impact speed with which the results of this work will be compared to is 33 m/s. This impact situation was extensively discussed in Part I of this study. The specimen, whose length, total width and thickness are 254 mm, 114 mm and 6 mm respectively, is illustrated in Figure 1 (a). The material constitution is steel/Homalite/steel and hence dynamic photoelasticity is employed. The details of experimental arrangements were reported in early work by the same authors [1]. A limited number of experiments using a sandwich style geometry (type B specimens of Part I) were also tested. The goal of these experiments was to study the effect of impact momentum.

II-3. Results and discussion

II-3.1 Effect of impact speeds

In Part I of this study, we investigated the nature and sequence of failure mechanisms in relation to model sandwich specimens of the above described geometry

and for an impact speed of 33 m/s. This impact speed situation will be taken as the baseline for our comparisons. Figure 1 describes an experiment of the same geometry that corresponds to an impact speed is 45 m/s. The field of view is the specimen edge.

After impact at the specimen center, the dilatational stress wave propagated towards the edge. Right after the stress wave reached the free edge (due to the existence of stress singularity at the bimaterial corner [8-9]), an inter-layer crack initiated at the lower interface at around 34 μs as seen in Figure 1 (b). This happened at approximately the same time as in the baseline specimen. This interfacial crack propagated dynamically towards the specimen center. After approximately 148 μs, another inter-layer crack initiated at the upper interface as shown in Figure 1 (c). Compared to a crack initiation time of 160 μs for the baseline specimen, this initiation time is slightly shorter but is still within the measurement error range (0~10 μs). This upper inter-layer crack soon interacted with the Rayleigh wave at the lower interface and kinked into the core to form an intra-layer crack. The kinked crack branched into a fan of intra-layer cracks shown in Figure 1 (d). This sequence is very similar to the result of the baseline specimen discussed in section 3 of Part I.

Despite their apparent similarities, there also exists some noticeable difference between the baseline and the 45 m/s impact cases. The major difference is in the recorded inter-layer, or interfacial crack tip speeds displayed in Figures 2 (a) and (b). Figure 2 (a) compares the speeds of inter-layer cracks propagating at the lower interface. For an impact speed of 45 m/s, the lower inter-layer crack initially propagated close to the shear wave speed of Homalite-100 becoming clearly intersonic (crack speed less than the longitudinal wave speed but greater than the shear wave speed of Homalite) at

approximately 60 μs. Throughout its recorded history this crack was clearly faster than its "baseline" counterpart. It should be recalled that at longer time, the baseline crack also became intersonic and reached speeds as high as $\sqrt{2}\,C_s$ as discussed extensively in section 3.1 of Part I. Figure 2 (b) compares crack tip speeds at the upper interfaces. Here again the level of the crack speed corresponding to 45 m/s impact speed is consistently higher than its baseline counterpart. In both cases, the inter-layer cracks remained purely sub-Rayleigh within our time window of observation.

In order to investigate the crack speed history at the central part of the specimen, the field of view was moved to the specimen center as shown in Figure 3. The same higher impact speed (45m/s compared to 33 m/s of the baseline) was employed. As seen from Figure 3 (b), two inter-layer cracks appeared at the lower interface and propagated towards the center, racing towards each other with intersonic speeds. At a later time, inter-layer cracks at the upper interface also appeared propagating towards the center (Figure 3 (c)). The locations of these four inter-layer cracks (two at the top and two at the lower interfaces) are indicated by the white arrows. As clearly seen from Figure 3 (e), intra-layer damage also spreads from the interface in to the core in the form of a periodic series of mode-I cracks inclined at a small angle to the vertical axis. These cracks are nucleated at the upper interface at locations that are behind the horizontally moving inter-layer shear crack. Their nucleation and growth result in the eventual fragmentation of the specimen core. The inter-layer cracks propagating at the lower bimaterial interface and facing towards each other in Figures 3 (d)-(e) feature clearly formed shock-like or Mach-like discontinuities (shear shock waves) which are emitted from their crack tips. These discontinuities in photoelastic patterns represent traveling discontinuities in maximum

shear stress and are clear proofs that crack tips have exceeded the shear wave speed of Homalite [2-4]. These shock waves formed a clear testimony to the intersonic nature of the inter-layer crack growth even before any detailed crack measurement was ever attempted.

The crack speed history for the lower, right inter-layer crack is plotted in Figure 4 as a function of distance from the free edge. The figure shows that the crack speed of the higher impact speed case (45 m/s) is always higher than the baseline equivalent remaining always intersonic within the window of observation. To complete the picture, Figure 5 displays collected experimental results from three identical specimens subjected to the same impact speed, which have areas of observations ranged from the specimen edge all the way to its center. As evident from Figure 5 (a), the inter-layer crack initiated at very high speeds and fluxuated close to the shear wave speed of Homalite, often becoming intersonic but never exceeding $\sqrt{2}\,C_s$. On the other hand, in the baseline case (33m/s) and as discussed in Part I, the crack became intersonic only when it approached the specimen centerline. Indeed, before it did so, it almost came to a complete stop at a distance of above 45 mm from the edge.

II-3.2 Effect of interfacial strengths

In order to compare the effect of different interfacial bond strengths on dynamic failure in layered materials and sandwich structures, four different kinds of adhesives were used to construct interfacial bonds of various strengths. The bond strengths for Homalite/adhesive/Homalite interfaces are listed in Table 1. Due to the stress singularity at bimaterial corners [8-9], it is hard to obtain the intrinsic bonding properties of

bimaterial interfaces based on current specimen configurations [10]. Instead in Table 1, we only list the strengths of these adhesives when they are used to bond identical Homalite pieces. This is done to provide relative levels of strengths of these adhesives. The Weldon-10 and Loctite 330 are considered to be "strong" adhesives. The Loctite 384 can form an "intermediate strength" bond while the Loctite 5083 gives a "weak bond." The Loctite 5083 is considered to be a kink of ductile adhesive because its elongation at failure in cured bulk form is as high as 170%. The average thickness of the adhesive layer is less than 20 μm. Here, in order to investigate the relative effect of various interfacial bond strengths, the baseline specimen configuration is chosen as the one shown in Figure 3, which features the Weldon-10 strong bonding and is subjected to an impact speed of 45 m/s.

Figure 6 shows a sequence of images of the specimen featuring the second strongest interface, i.e., that of Homalite/330/steel. The field of view is that of the specimen center as shown in Figure 6 (a). The initial failure characteristics in this type of a specimen are quite similar to the ones observed in the baseline specimen with strongly bonded interfaces (i.e., Homalite/Weldon-10/steel), subjected to the same impact conditions as shown in Figure 3. The first failure mode encountered is still the inter-layer crack at the lower interface. However, for the current case, the two inter-layer cracks separated the entire lower interface at 176 μs after impact as shown in Figure 6 (c) compared to 148 μs in Figure 3 (e). Following inter-layer failure, two intra-layer cracks initiated from the upper interface. Later on and as evident from Figure 6 (d), another mode I intra-layer crack stemmed from the lower interface revealing a locally symmetric fringe pattern and propagating along the specimen centerline. It is speculated that this

mode I crack is a result of symmetric specimen bending established at long times after impact. It should be recalled that the shear strength of the 330 bond is much lower than that of the Weldon-10 bond as seen in Table 1. However, the interfacial tensile strength of the 330 bond is only 10% below that of the strong Weldon-10 bond. The differences between these cases discussed here suggest that the interfacial shear strength is vital to the evolution of impact damage in layered materials and sandwich structures.

Figure 7 presents a series of fringe patterns showing the evolution of failure in a specimen featuring intermediate strength 384 adhesive bonds subjected to the same impact condition of 45 m/s. The two lower inter-layer cracks completely dobonded the lower interface at 154 μs, slightly later than in the baseline specimen featuring two strong bonds. The upper inter-layer cracks separated the whole upper interface at 207 μs as clearly shown in Figure 7 (e), compared to 157 μs for the specimen featuring the strong Weldon-10 bonds. Similar to the previous case, intra-layer cracks initiated from the upper interface as evident from Figure 7 (f). Although the 384 interfacial bonding is called "intermediate strength bonding," its interfacial tensile strength is only 15% lower than that of the baseline strong bonds. However, its shear strength is substantially lower than that of the strong bonding as listed in Table 1. Here again, it becomes evident that the interfacial shear strength is by itself as an important parameter in controlling the detailed evolution of failure. This is perhaps not very surprising since inter-layer fracture is clearly shear-dominated for the layered materials and structures subjected out-of-plane impact loading.

Figure 8 corresponds to a case where both the interfacial shear and tensile strengths are reduced significantly by using the weak but ductile 5083 adhesive, whose

characteristics are also described in Table 1. As shown in Figures 8 (a) and (b), an inter-layer crack generated at the specimen edge is seen propagating towards the impacted point at the specimen center. A thin shear shock line inclined at an angle slightly above 45° to the horizontal interface (Figure 8 (b)) marks the position of this crack which clearly moves intersonically to the right. Since the bond strengths are both very low, the stress concentration appears less strong than in the baseline case (see Figure 3). Crack tip speed in this case, however, is very much higher than all other cases and, at the initial stages, is very close to $\sqrt{2}\,c_s$. To illustrate the strong difference in crack initiation time and in crack tip speed history between otherwise identical specimens featuring strong and weak bonds, Figure 9 compares results from the two extreme cases (Weldon-10 and 5083). In both cases, the field of view is concentrated at the specimen edges. It is observed that the weak but ductile 5083 adhesive results in longer initiation time and very high crack tip speeds. These speeds are initially close to $\sqrt{2}\,c_s$ then decrease to c_s, and finally pick up as the specimen center is approached. On the hand, the strong Weldon-10 bond features a short initiation time and more moderate speeds ranging from the Rayleigh wave speed to just above the shear wave speed as the distance from the edge increases.

II-3.3 Dynamic crack arrest and re-initiation

In Part I of this work, we observed that the speed of an inter-layer crack decreased to a very low value at around 90 μs after impact (the corresponding position is about 40 mm from the free edge) [1]. This phenomenon repeated in other specimens subjected to different loading and bonding conditions. Figure 10 shows the fringe pattern development of an inter-layer crack at the lower interface of a specimen featuring the second strongest

bond in Table 1. A high impact speed of 46 m/s was used, compared to the 34 m/s baseline impact speed in Part I of this paper. After comparing the crack tip characteristics in Figures 10 (b) and (c), we can see that the fringe concentration delineating the crack tip hardly moved between 98.5 μs and 117.5 μs. Moreover, the fringe pattern reveals a visibly reduced fringe concentration, which indicates local unloading at the arrested crack tip. The time history of crack lengths and associated crack speeds of two identical specimens subjected to the same impact loading are shown in Figure 11. The clear plateau of the crack length versus time record reveals the existence of very low crack speeds at a repeatable time and location. It is interesting to notice that crack speed almost drops to zero at around the same time of 90 μs, as is also reported in Part I of this paper. The location of near crack arrest is also around a distance of 40-50 mm from the specimen edge, exactly as in the strong bond case.

It is theorized here that this phenomenon is associated with the complicated wave interaction and the special characteristics of interfacial cracks at bimaterial interfaces. In previous research on interfacial cracks, Lambros and Rosakis [3] and Needleman and Rosakis [6] showed that as soon as an interfacial crack accelerates to the Rayleigh wave speed, it keeps a stable speed as long as constant energy supply is provided to the crack tip. If the energy supply is suddenly increased (perhaps by the arrival of a loading reflected wave from the specimen boundaries), the crack accelerates unstably to an other discreet constant level within the intersonic regime. If, however, an unloading wave reaches the crack tip, the crack quickly arrests. We believe that the temporary arrest behavior observed here is a demonstration of the same type of behavior in a more complex structure than the one tested by Lambros and Rosakis [3] and modeled by

Needleman and Rosakis [6]. Here the complex wave interaction and the structural vibration response of the specimen, which gradually establish themselves with time, result in temporary loss of driving force that accounts for the observed crack arrest and re-initiation. Recently, Yu et al. successfully simulated this phenomenon [11].

II-3.4 Different impact damage in sandwich structures subjected to the same impact energy

Figure 12 compares the final impact failure patterns of two identical specimens subjected to the same impact energy (kinetic energy, K, of the projectile) but different impact momentum and impact loading duration time. In both cases, the air gun pressure was kept the same to ensure that the resulting projectile energy was the same. In case (a), a heavy and long projectile was employed hence a lower projectile speed was achieved with the same air gun chamber pressure. While case (b) is corresponding to a light and short projectile, so a higher impact speed can be achieved under the same air gun pressure. The two projectiles used in two cases are identical in materials and dimensions except for the projectile lengths. The projectile length in case (a) is about 2.5 times the length in case (a). As shown in Figure 12 (a), both inter-layer cracks and intra-layer cracks appeared after impact. However, for case (b), only inter-layer cracks at both interfaces occurred resulting to complete shear-induced delamination before any matrix or intra-layer cracks had the chance to form. Although for the impact case (b), a higher bullet speed was obtained; the impact damage seems to correlate to the impact momentum and impact loading duration under the same impact energy.

$$\frac{1}{2}(m_1 v_1)v_1 = \frac{1}{2}(m_2 v_2)v_2 \Longrightarrow \frac{m_1 v_1}{m_2 v_2} = \frac{v_2}{v_1} > 1$$

In case (a), the impact momentum is high and the loading duration is long, and the post mortem impact damage is severe. The history of two inter-layer cracks for these two different cases is presented in Figure 13. In both cases, these cracks originated from the specimen edges. However, substantially different propagation features were observed: for the specimen subjected to high impact momentum and long loading duration, the crack speed increases moronically and reaches a steady speed around the Rayleigh wave speed of Homalite-100. However, for the specimen subjected to low impact momentum and short loading duration, at the initiation stage, the crack speed can initially be very high. However, the crack speed drops to a lower value and fluctuates widely reaching again the Rayleigh wave speed of Homalite-100 at a late stage. In previous impact studies of composite laminates and sandwich plates [12], researchers often used impact energy as an indicator of the extent of final (post-mortem) impact damage (e.g., delamination size). Indeed impact momentum and loading duration are also important in controlling impact damage in layered materials and sandwich structures subjected to the same impact energy. The exact role of impact momentum and loading duration merits further investigation.

II-4. Concluding remarks

High impact loading leads to high inter-layer crack speeds in layered materials and sandwich structures. Strongly bonded specimens subjected to high impact speeds are

shown to feature intersonic cracks depending accompanied by the formation of clearly visible shear shock wave (Mach lines) emitted from the crack tips. Also, under the same impact energy, two specimens may show quite different final impact damage patterns if they are subjected to different impact momentum and load duration. Reduced interfacial strengths (especially interfacial shear strengths) will result in visible changes of failure sequence. Also, inter-layer cracks at intermediate strength interfaces feature crack speeds slightly slower than those at strong interfaces. However, cracks at weak but ductile interfaces, initiate very late and have a very high speed at the first stage of crack propagation compared to their strong interface counterparts. Finally, highly transient crack arrest and re-initiation phenomenon were observed and analyzed.

Acknowledgements

The authors gratefully acknowledge the support of the Office of Naval Research (Dr. Y. D. S. Rajapakse, Project Monitor) through a grant (#N00014-95-1-0453) to Caltech.

References

[1] Xu L R, Rosakis A J. Impact failure characteristics in sandwich structures; part I: basic failure mode selection. Submitted to International Journal of Impact Engineering 2001.

[2] Rosakis A J, Samudrala O, Singh R P, Shukla A. Intersonic crack propagation in bimaterial systems. Journal of the Mechanics and Physics of Solids 1998;46:1789-1813.

[3] Lambros J, Rosakis A J. Shear dominated transonic growth in a bimaterial –I. experimental observations. J Mech Phys Solids 1995;43:169-188.

[4] Liu C, Huang Y, Rosakis A J. Shear dominated transonic crack growth in a bimaterial –II. asymptotic fields and favorable velocity regimes. J Mech Phys Solids 1995;43:189-206

[5] Samudrala O, Rosakis A J. in preparation 2001.

[6] Needleman A, Rosakis A J. The effect of bond strength and loading rate on the conditions governing the attainment of intersonic crack growth along interfaces. J Mech Phys Solids 1999;47:2411-2449.

[7]. Liu D, Basavaraju B, Dang X. Impact perforation resistance of laminated and assembled composite plates. International Journal of Impact Engineering. 2000;24(6-7):733-746

[8] Williams M L. Stress singularities resulting from various boundary conditions in angular corners in extension. J Applied Mechanics 1952;19:526-528.

[9] Pageau S S, Gadi K S, Biggers S B, Joseph P F. Standardized complex and logarithmic engensolutions for N-material wedges and junctions. International Journal of Fracture 1996; 77:51-76.

[10] Xu L R, Rosakis A J. Comparison of static tensile and shear strengths and fracture toughness of various adhesive bonds between elastic solids. 2001 In preparation.

[11] Yu C, Ortiz M. Pandolfi A. Rosakis A. J. Private communication 2001.

[12] Abrate S. Impact on laminated composites: recent advances. Applied Mechanics Reviews 1994;47:517-544.

List of table

List of figures

Figure 8. Intersonic inter-layer crack in a three-layer specimen with weakly bonded interfaces (3lshssb583-1). The crack initiation is delayed but the crack speed is intersonic resulting in a clearly visible shock structure seen in Figs. (b) to (c).

Figure 9. Crack speed history (a) and crack speed distributions along the specimen length direction (b) for two specimens with different interfacial bond strengths subjected to the same impact loading.

Figure 10. Visual evidence of the transient inter-layer crack arrest mechanism at the lower interface (3lshssb330-5).

Figure 11. Time history of crack length (a) and crack speed (b) for two identical specimens featuring the second strongest bonding subjected to the same impact loading.

Figure 12. Different post-impact failure patterns of two identical specimens subjected to the same impact energy but different impact momentum loading duration.

Figure 13. Crack speed history of two inter-layer cracks at the lower interfaces of two identical specimens subjected to the same impact energy but different impact momentum and loading duration.

Table 1. Interfacial strengths and model I fracture toughnesses of different bonds

Interface	Tensile strength (MPa)	Shear strength (MPa)	Fracture Toughness ($MPa*m^{1/2}$)
Homalite//Weldon-10// Homalite	7.74	>21.65	0.83
Homalite//330// Homalite	6.99	12.58	0.93
Homalite//384// Homalite	6.75	7.47	0.38
Homalite//5083// Homalite	1.53	0.81	0.19

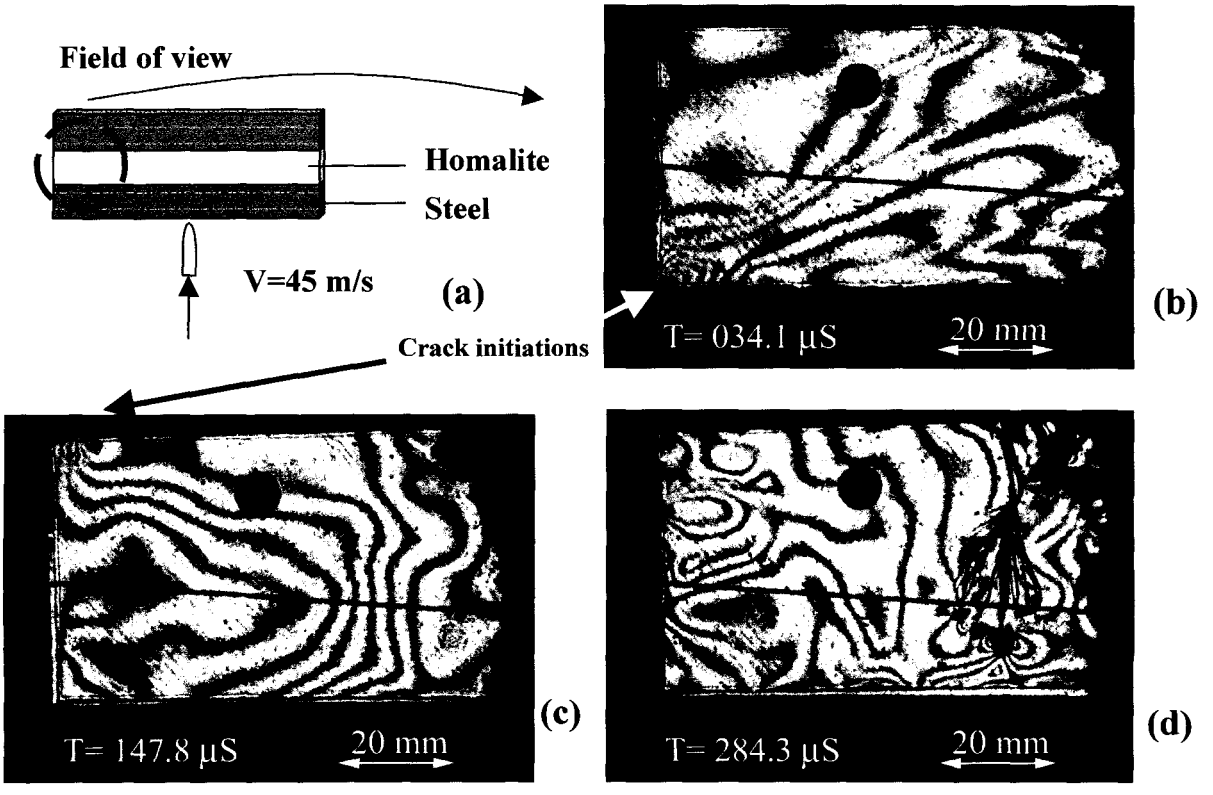

Figure1. Failure process at the edge of a specimen featuring two strong interfacial bonds

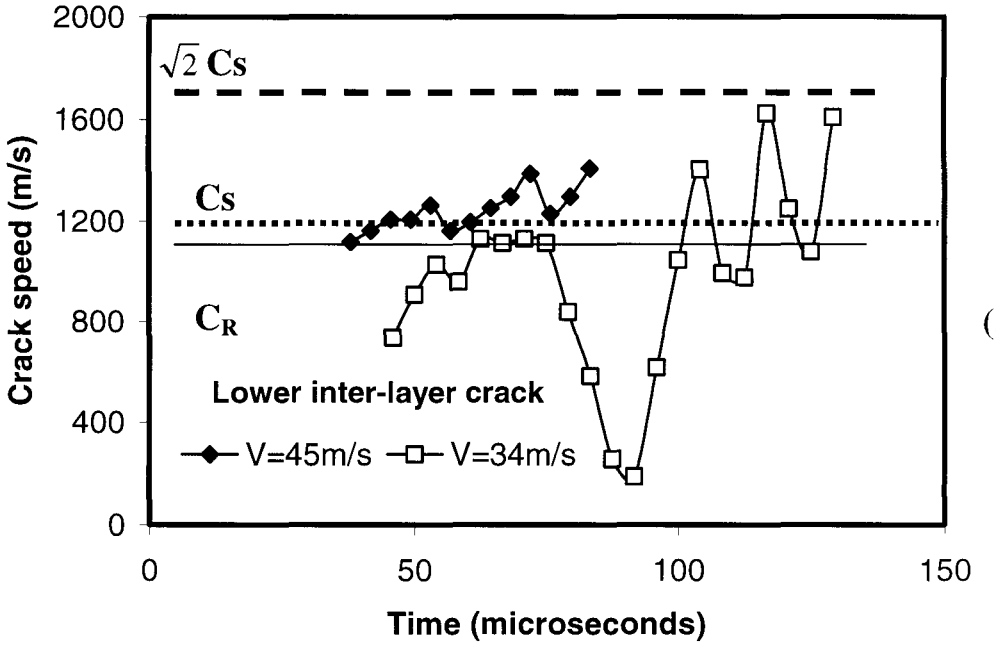

(a)

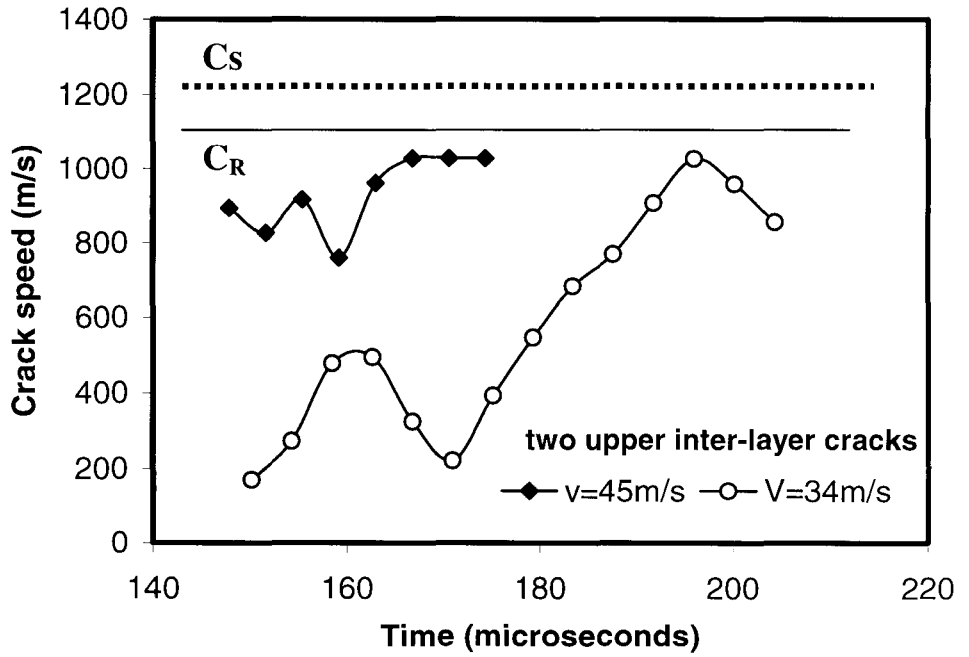

(b)

Figure 2. Comparison of interfacial crack speeds of two identical specimens subjected to different impact speeds. The interfacial bonds are strong Homalite/Weldon-10/steel bonds.

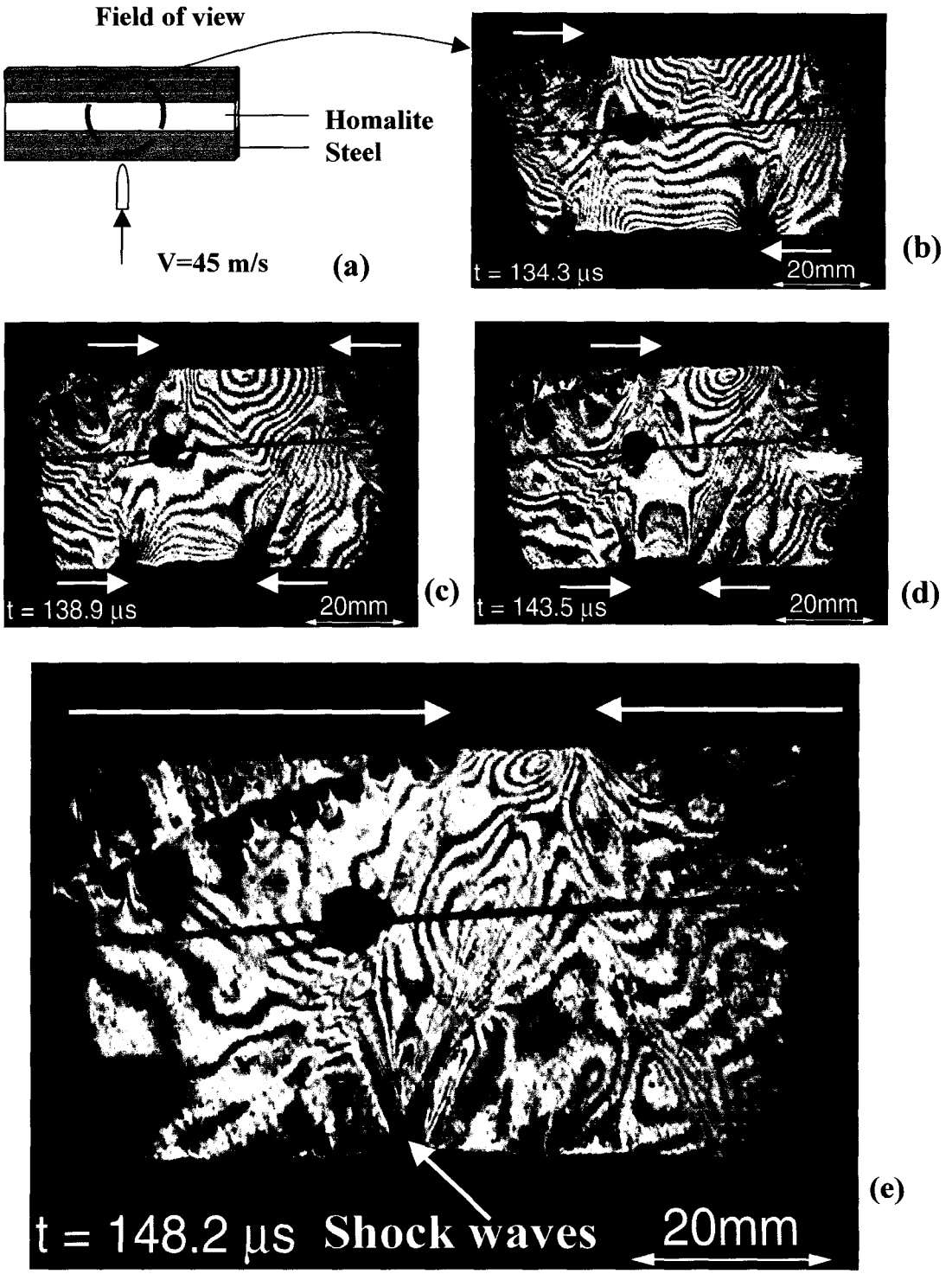

Figure 3. Growth of four inter-layer cracks at the center of a three-layer specimen (3lshssbwd-6)

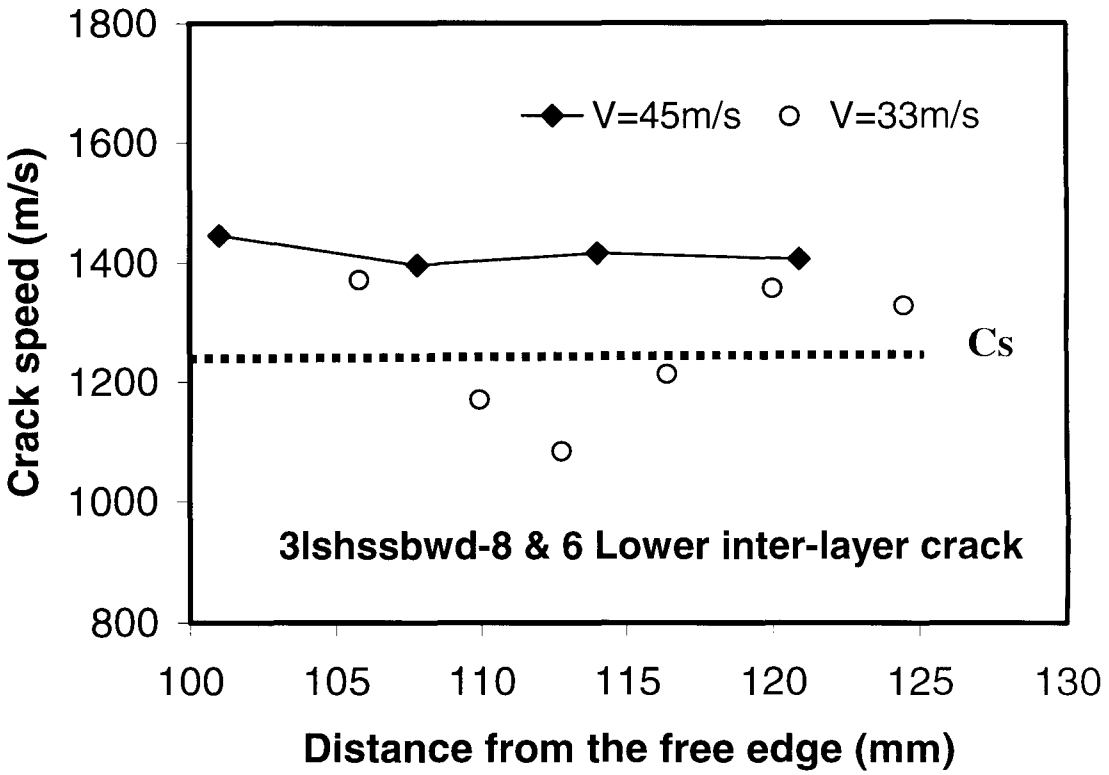

Figure 4. Comparison of crack speed distributions of two identical specimens subjected to different impact speeds. The dash line is the dynamic shear wave speed of Homalite-100.

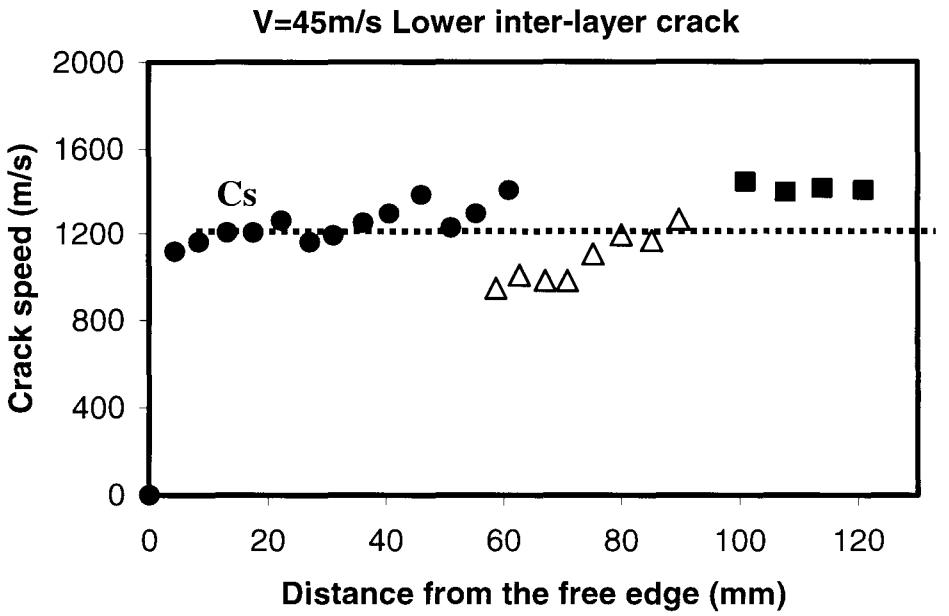

(a)

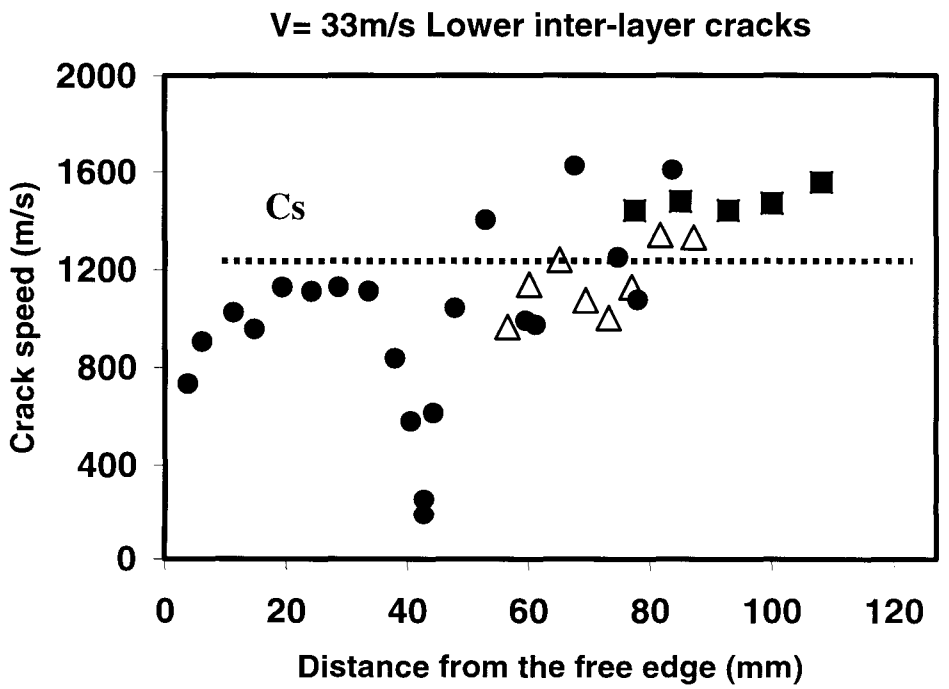

(b)

Figure 5. Comparison of the crack speed distribution along the bond length for identical specimens subjected to different impact speeds.

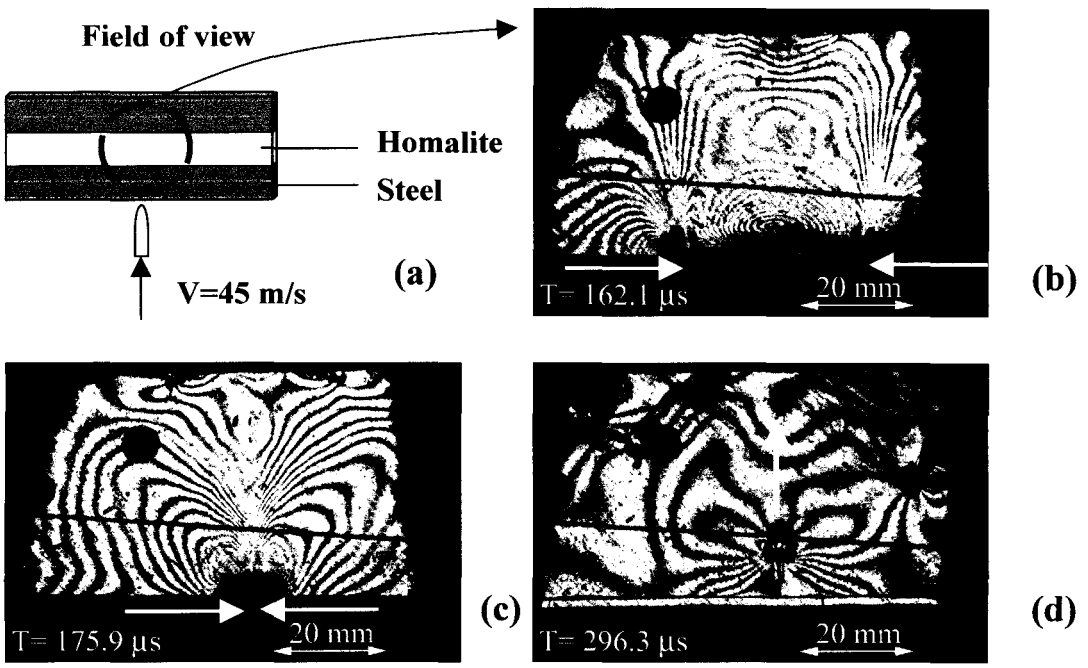

Figure 6. Different failure modes and sequence in a three-layer specimen with second strongest bonding (3lshssb330-6). Intra-layer cracks initiated from the upper interface in a symmetric pattern (Fig. (c)) and later on, one intra-layer crack stem from the lower interface (Fig. (d)).

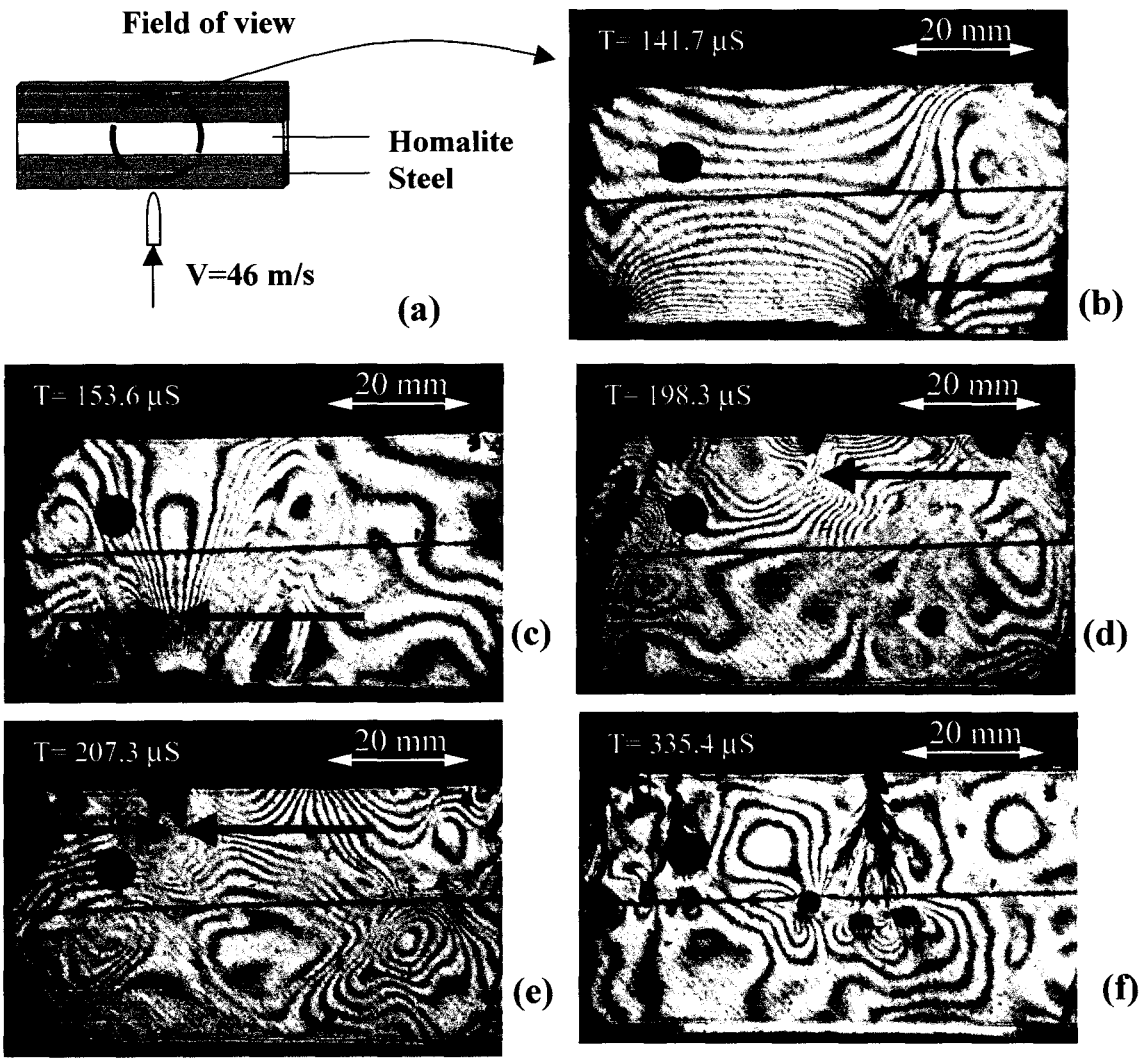

Figure 7. Failure process of a three-layer specimen with two intermediate strength bonds (3lshssb384-2). After upper interface debonding, two intra-layer cracks initiated from the upper interface and propagated towards the lower interface.

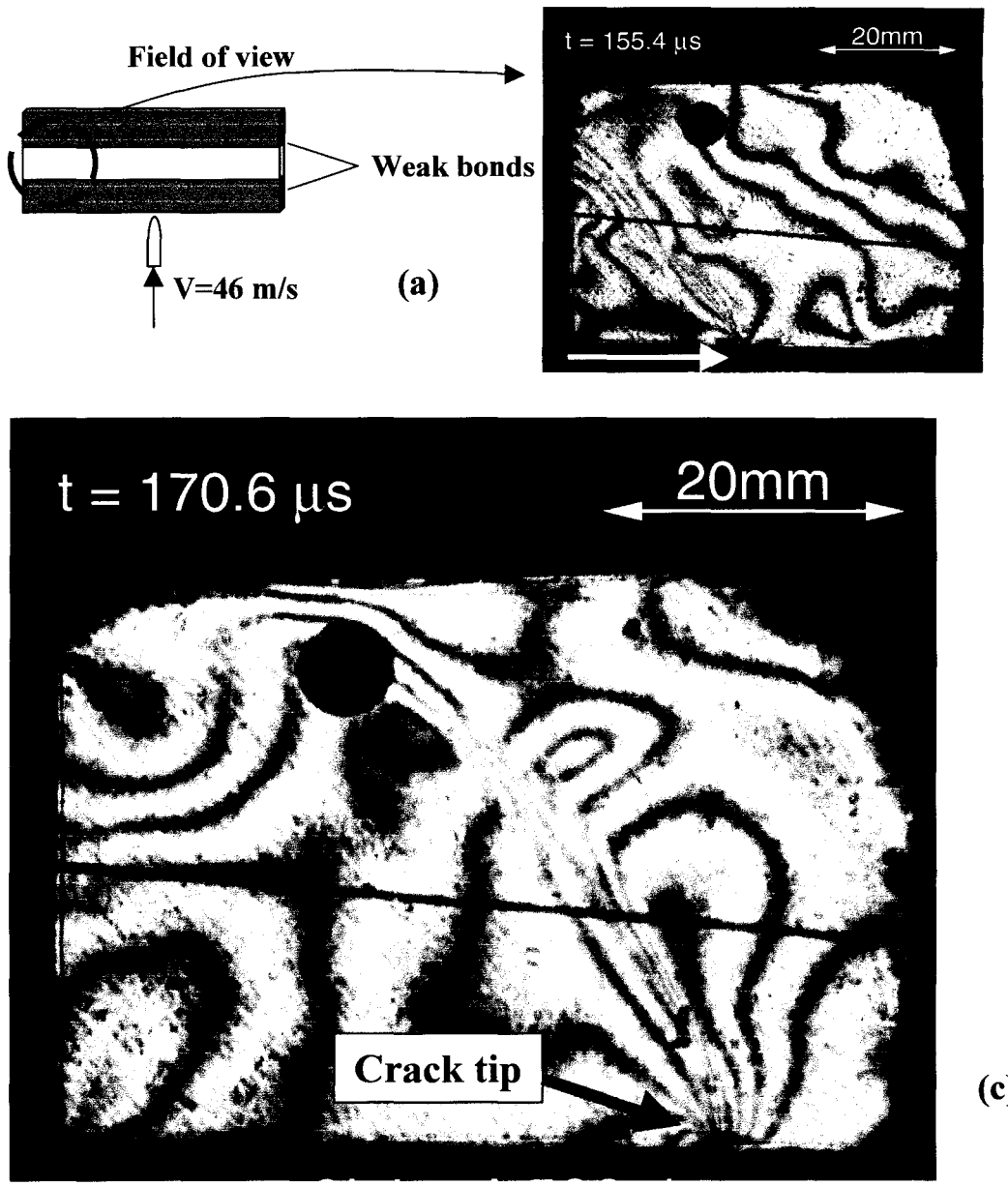

Figure 8. Intersonic inter-layer crack in a three-layer specimen with weakly bonded interfaces (3lshssb583-1). The crack initiation is delayed but the crack speed is intersonic resulting in a clearly visible shock structure seen in Figs. (b) to (c).

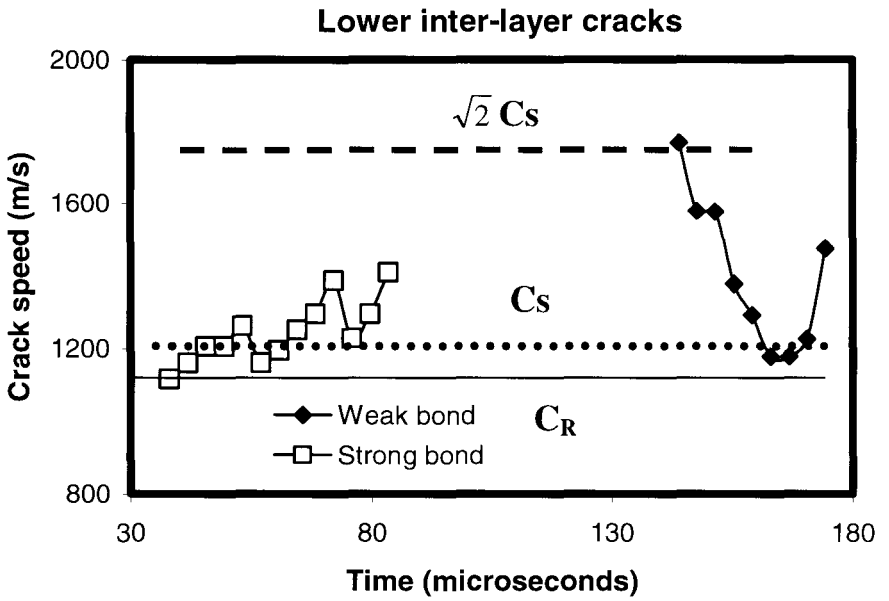

(a)

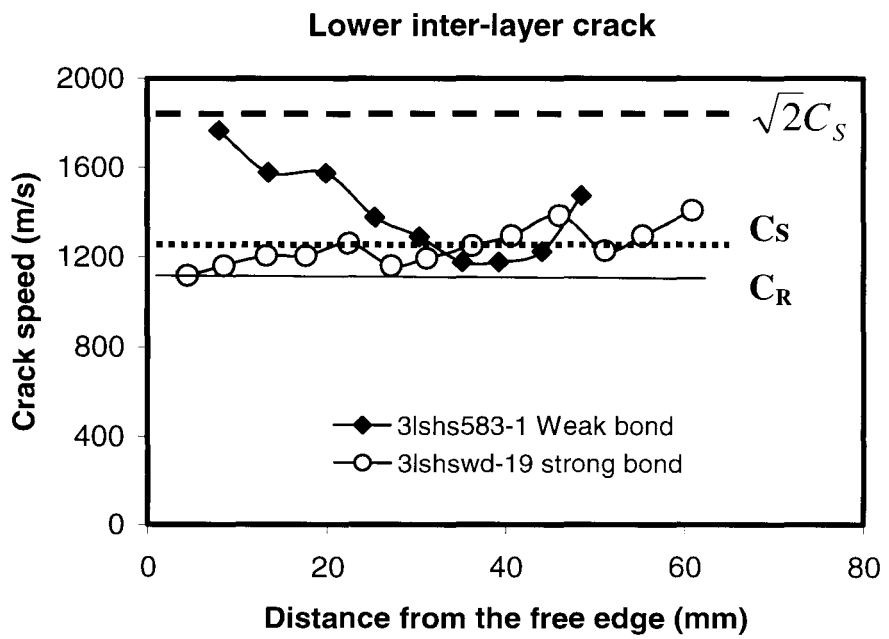

(b)

Figure 9. Crack speed history (a) and crack speed distributions along the specimen length direction (b) for two specimens with different interfacial bond strengths subjected to the same impact loading.

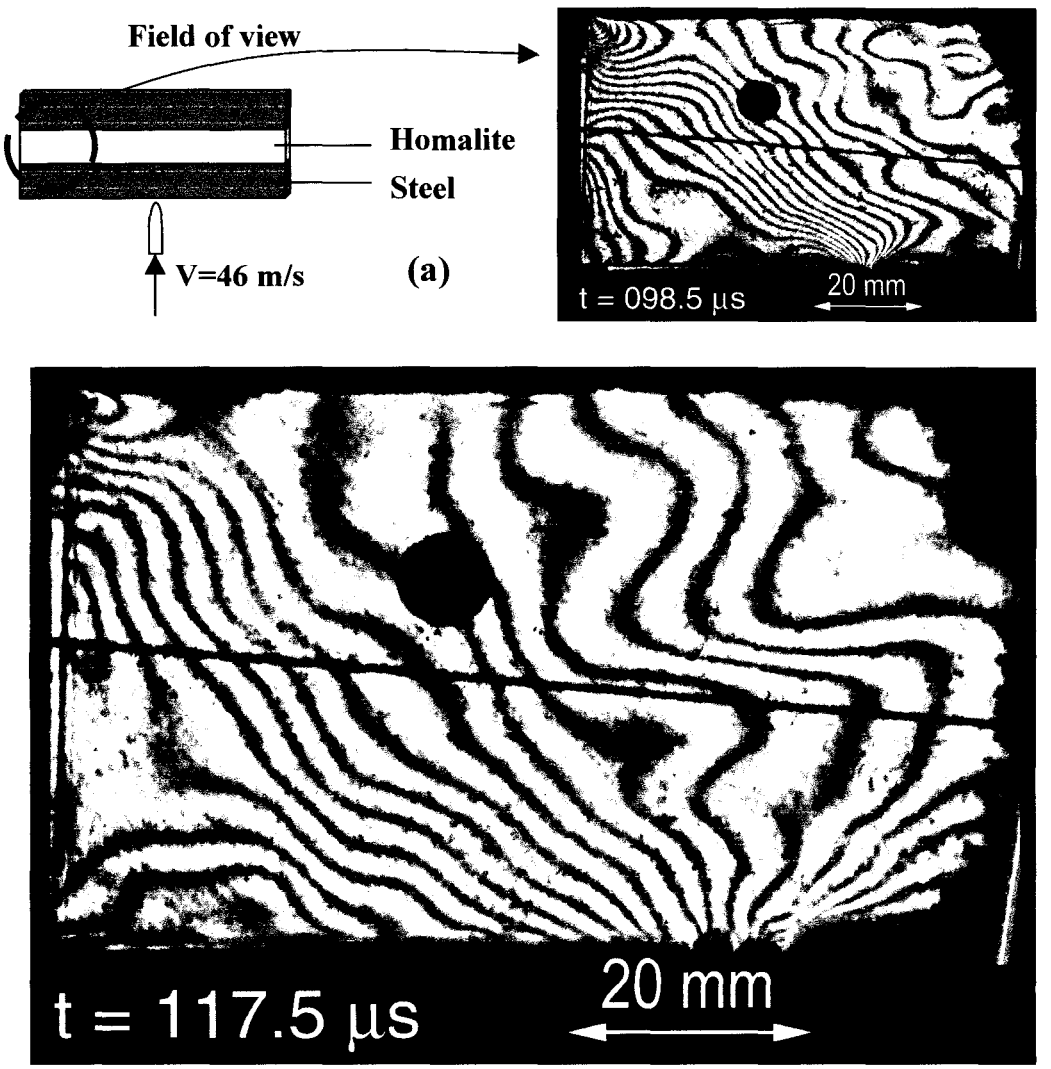

Figure 10. Visual evidence of the transient inter-layer crack arrest mechanism at the lower interface (3lshssb330-5).

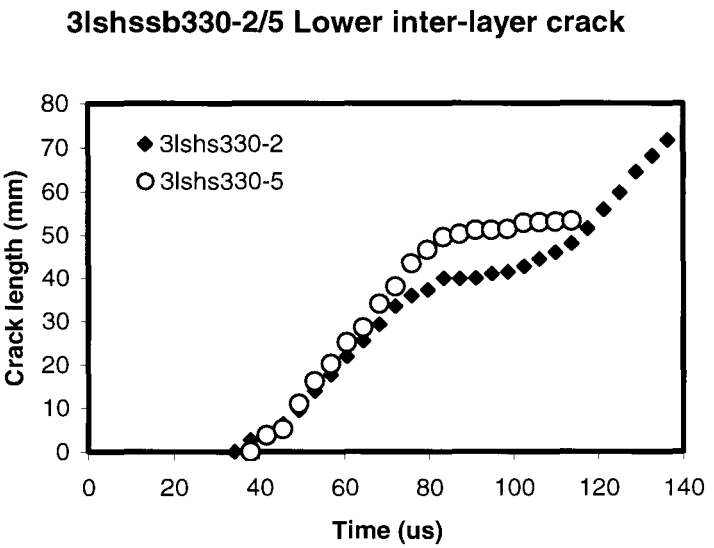

(a)

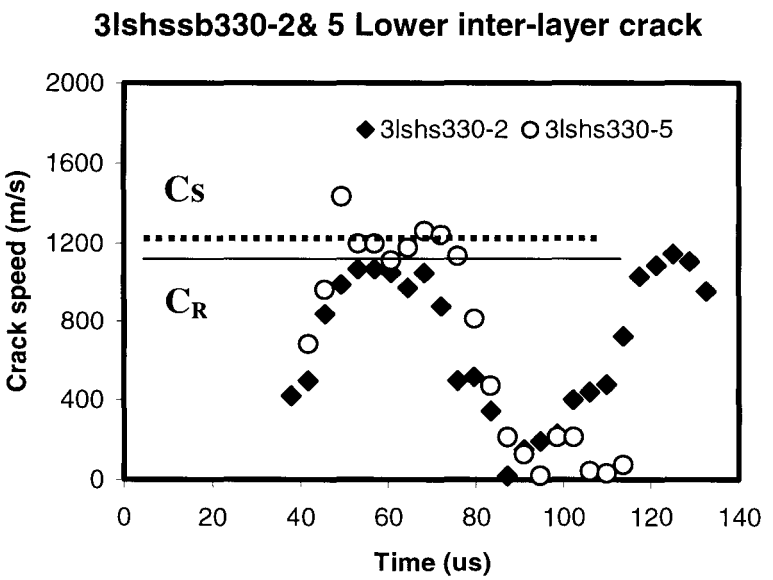

(b)

Figure 11. Time history of crack length (a) and crack speed (b) for two identical specimens featuring the second strongest bonding subjected to the same impact loading.

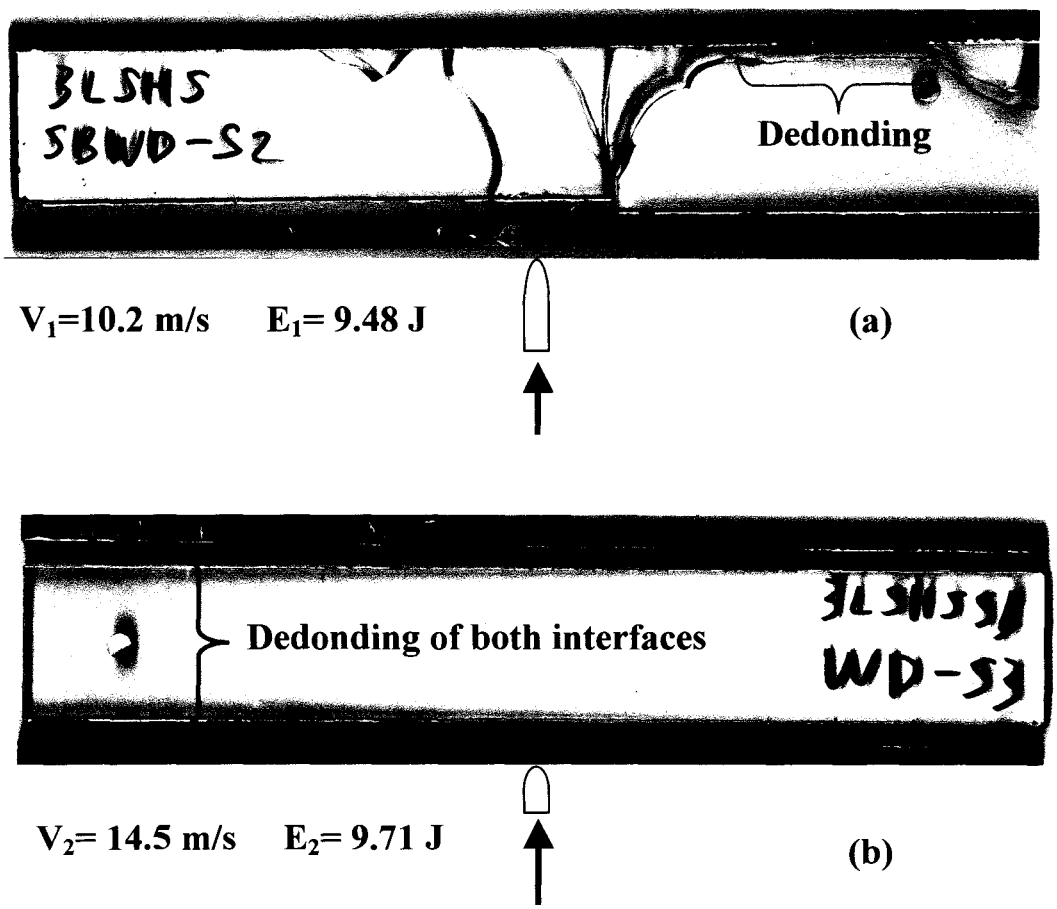

Figure 12. Different post-impact failure patterns of two identical specimens subjected to the same impact energy but different impact momentum and loading duration.

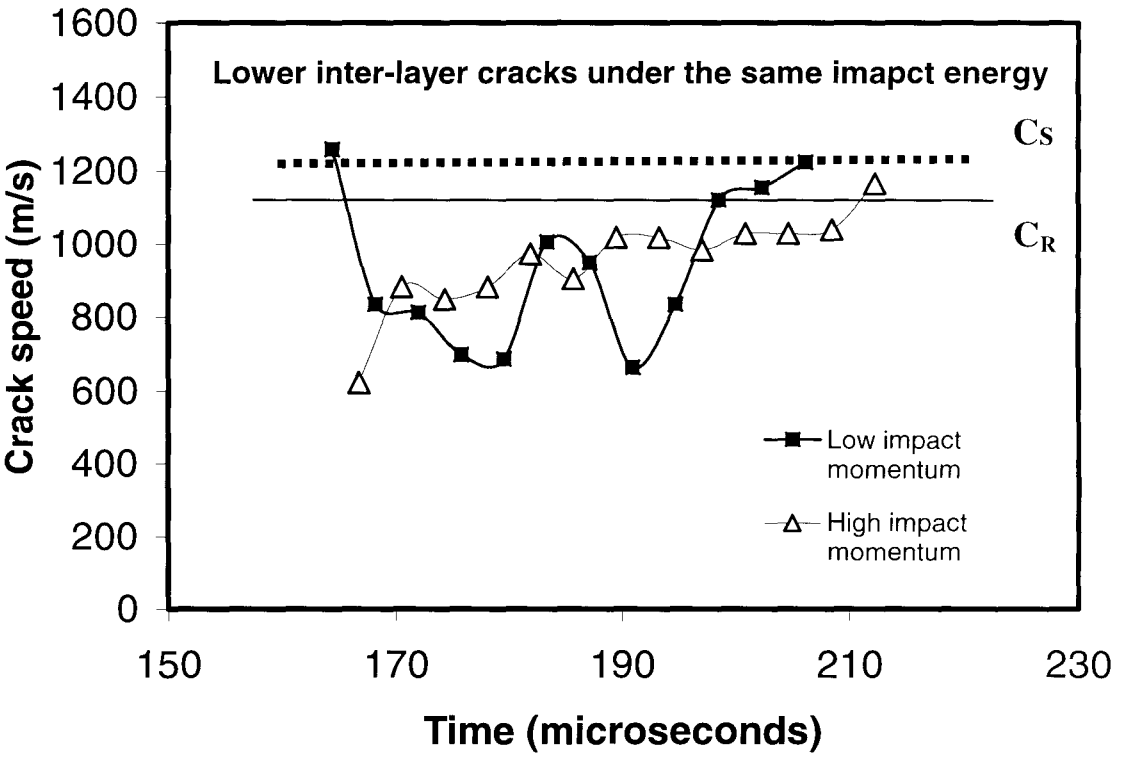

Figure 13. Crack speed history of two inter-layer cracks at the lower interfaces of two identical specimens subjected to the same impact energy but different impact momentum and loading duration.

Chapter III

An Experimental Study of Impact-induced Failure Events in Homogeneous Layered Materials Using Dynamic Photoelasticity and High-speed Photography

Abstract

The generation and the subsequent evolution of dynamic failure events in homogeneous layered materials that occur within microseconds after impact were investigated experimentally. Tested configurations include three-layer and two-layer, bonded Homalite specimens featuring different bonding strengths. High-speed photography and dynamic photoelasticity were utilized to study the nature, sequence and interaction of failure modes. A series of complex failure modes was observed. In most cases, and at the early stages of the impact event, intra-layer failure (or bulk matrix failure) appeared in the form of cracks radiating from the impact point. These cracks were opening-dominated and their speeds were less than the crack branching speed of the Homalite. Subsequent crack branching in several forms was also observed. Mixed-mode inter-layer cracking (or interfacial debonding) was initiated when the intra-layer cracks approached the interface with a large incident angle. The dynamic interaction between inter-layer crack formation and intra-layer crack growth (or the so-called "Cook-Gordon Mechanism") was visualized for the first time. Interfacial bonding played a significant role in impact damage spreading. Cracks arrested at weak bonds and the stress wave intensity was reduced dramatically by the use of a thin but ductile adhesive layer.

III-1. Introduction

Layered materials and structures have promising applications in many important fields of engineering. These include, among others, the use of advanced composite laminates in aerospace engineering; sandwich structures in naval engineering; and multi-layered thin film structures in micro-electronic-mechanical systems. In an entirely different length scale such materials are also found in the complex layered rock structures of earth's crust. While failure characteristics of layered materials subjected to static loading have been investigated extensively in past years[1], their dynamic counterparts have remained elusive. Our current research interest focuses on studies of such dynamic failure events in layered materials and, in particular, on the identification of the chronology and sequence of these events. For most layered materials, the presence of highly complicated dynamic failure modes and the inaccessibility of internal damage to real-time scrutiny has resulted in experimental studies of only the final impact damage characteristics and to the measurement of post-mortem residual strengths[2-4]. Hence, the sequence and nature of failure process have never been properly clarified.

For many simple engineering structures subjected to static or dynamic loading, computational and analytical models can be employed to provide realistic approximations of the physical failure processes under investigation. However, this may not be possible when more complex geometries, involving layered materials or configurations, need to be investigated. For such more complex cases, model experiments may prove extremely useful as intermediate steps, which reveal the basic physics of the problem and provide relatively straightforward validation of computational models before such models are applied to predictions of the fully complex failure situations. A striking example of the role of model experiments was provided by Riley and Dally[5], who designed a model

metal/polymer layered specimen subjected to dynamic loading. Their model configuration was designed to simulate dynamic loading and stress wave evolution in complex layered structures.

In our experiments, we adopt and extend the same concept and to that effect we introduce an appropriate intermediate model configuration, which allows us, in addition to stress wave loading, to study the basic dynamic failure mechanisms involved in a layered structure. Indeed, in order to simulate the difficult three-dimensional problem of the out-of-plane impact of real layered structures and in the same time preserve the essence of the failure phenomena involved, we propose a two-dimensional, plane stress specimen, which represents a cross-sectional cut from a layered structure as illustrated in Figure 1. For this type of model specimens, failure processes are easy to record, visualize and analyze. It is noted that although the exact impact mechanics involved in these two configurations are not identical (mainly because of dimenionality constraints), the general mechanisms of stress wave propagation and failure progress of the real and model layered materials are quite similar.

As discussed by Xu and Rosakis[6], in designing these model two-dimensional specimens, it is important to select model materials whose elastic mismatch is similar to that of materials used in real engineering applications. Selecting similar Dundurs' parameters[1] may ensure similarity of the elasto-static response. Meanwhile, selecting model material combinations with similar ratios of wave speeds as the real structure is important in considering similarity of their elasto-dynamic behaviors. These two issues form similarity rules to connect real structures and experimental models. In the present investigation, we only study layered materials composed of one kind of homogeneous

material. For this zero stiffness-mismatch case, both Dundurs' parameters vanish and the ratio of wave speeds is unity. The resulting layered structure is constitutively homogeneous and it only features planes of strength and fracture toughness inhomogeneity (bonds lines) between layers. In the absence of constitutive material property mismatch, our major purpose is only to explore the effect of interfacial bonding on the development of dynamic failure mechanism in layered materials.

The objectives of the current work are to conduct systematic experimental studies of the time evolution and the nature of different failure events and to investigate the interaction of these dynamic failure modes in real-time. Through these model experiments, we try to provide guidance for the construction of theoretical models and validation of numerical codes.

III-2. Experimental Program

III-2.1 Materials and Specimens

Homalite-100 was selected as our model photoelasticity materials. Some of its physical properties are listed in Table 1. The quasi-static values are obtained from the literature while the dynamic values are measured by the procedure outlined in section 3. The dynamic fracture characteristics of bulk Homalite-100 have been well investigated in the past decades[7-10]. Here, we mainly pay attention to the dynamic failure modes of Homalite in layered form. To provide different interfacial strengths and fracture toughnesses, four kinds of adhesives, Weldon-10 and Loctite 330, 384 and 5083, were used to bond the interfaces[11]. The interfacial bond strengths and the fracture toughness for those adhesives are listed in Table 2. The Weldon-10 and Loctite 330 are considered to be "strong" adhesives. The Loctite 384 can form an "intermediate strength" bond while

the Loctite 5083 gives a "weak bond." The thickness of the final adhesive layer is less than 20 μm. Loctite 5083 adhesive is also considered to be a ductile adhesive since its elongation at failure (as measured by the manufacturer) in cured bulk form is 170% or two orders of magnitude higher than the rest of the adhesives.

Three different types of specimens were designed and tested. As shown in Figure 2, type-A specimens have two layers with equal layer widths, and type-B specimens involve two layers with one layer twice as thick as the other. Type-C specimens were designed to have two bonding interfaces and three equal-width layers. All three types of specimens have the same out-of-plane thickness of 6.35mm (0.25 inch) and the same length of 254 mm (10 inches). In general, each layer width is 33 mm except for a few specimens in which w_1=38.1mm.

III-2.2 Experimental Setup

A schematic of the dynamic photoelasticity setup used in this study is given in Figure 3. Two sheets of circular polarizer were placed on either side of the specimen. An Innova Sabre argon-ion pulsed laser was used as the light source. The laser was set to operate on a single wavelength—514.5 nm (blue-green light). At this wavelength, the continuous power output of the laser is 8 W. The laser emits an intense beam of 2 mm diameter which is 100:1 vertically polarized. An acousto-optic modulator (Bragg cell) is placed in front of the laser to produce a pulsed output. The duration of each laser pulse can be varied between 8 ns and 20 ns. During the impact experiment, the acousto-optic modulator is driven by the high-speed camera to control the timing of each laser pulse, so that it coincides with the times the camera optics are aligned to expose a particular frame

on the film track. An electro-mechanical shutter is placed in front of the laser to prevent the light "leaking" through the Bragg cell from exposing the film before or after the experiment. A wide gap sensor mounted on the gas gun barrel about 1 inch from the end is used to trigger the shutter opening for a short duration (around 10 ms). A strain gage bonded to the specimen at the impact side was used to trigger recording by the high-speed camera. The coherent, monochromatic, plane polarized light output is collimated to a beam of 100 mm diameter. The laser beam is transmitted through the specimen. The resulting fringe pattern is recorded by the high-speed camera.

A Cordin model 330A rotating mirror type high-speed film camera was used to record the images. The high-speed camera contains a rotating mirror which directs the image on to the film mounted on a film track surrounding it. The rotating mirror is driven by a gas turbine running on compressed helium. Individual frames are exposed sequentially by inducing the laser to produce a high-powered pulse of short duration and when the rotating mirror is aligned to a particular frame. The camera records 80 distinct images at frame rates of up to 2 million per second. A feedback signal from the turbine is fed to a 10 KHz frequency counter, which allows a precise monitoring of the turbine speed. Also, the synchronizing signal sent by the camera to the acousto-optic modulator is simultaneously routed to a HP digital oscilloscope to obtain a record of the timings of each individual laser pulse. Kodak TMAX 400 black and white film was used to record the fringe patterns. The optical system in the high-speed camera introduces an elliptical distortion to the recorded films. For a circular original image, the recorded image is an ellipse with its major axis about 15% larger in comparison with the minor axis. The

developed negatives were scanned using a negative scanner and the elliptical distortion was removed digitally.

During the impact test, a projectile was fired by the gas gun and hit the specimen or a steel buffer to trigger the recording system. Under the dynamic deformation, the generation of isochromatic fringe patterns is governed by the stress optic law. For the case of monochromatic light, the condition for the formation of isochromatic interference fringes can be expressed as[7]

$$\hat{\sigma}_1 - \hat{\sigma}_2 = \frac{Nf_\sigma}{h}$$

where $\hat{\sigma}_1 - \hat{\sigma}_2$ is the principal stress difference of the thickness averaged stress tensor. f_σ is the material fringe value which is listed in Table 1, N is the isochromatic fringe order and h is the half specimen thickness. The isochromatic fringe patterns observed are proportional to contours of constant maximum shear stress, $\hat{\tau}_{\max} = (\hat{\sigma}_1 - \hat{\sigma}_2)/2$.

III-2.3 The Three-lens System

In order to observe remote failure event interactions, a large field of view is necessary. However, our Cordin 330A camera has a long front optical tube and its maximum view angle 2β is 4 degrees as shown in Figure 4. If a single lens is used, the maximum size of the field of view is 2 f tan (β), were f is the focal length of the lens. In order to minimize shadow spot formation, f should be chosen to be a small value based on our practical experience. As a result, the resulting field of view will be too small for full specimen visualization. To remedy this problem, a three-lens system is employed as shown in Figure 4. In this system, the first lens facing the 100 mm laser beam is a Plano-

convex lens whose focal length is 380 mm. The second lens is a Plano-concave lens whose focal length is 100 mm. Lenses 1 and 2 share the same focal point at one side and, as a result, a parallel beam of reduced diameter is formed. This beam passes through a bi-convex lens (lens 3) of focal length 500 mm. The resulting converging beam incident angle is less than 2 degrees and satisfies our stated requirement. Hence, the full 100 mm beam can enter the long camera tube.

Another restriction governing the choice of lens types and focal lengths comes from aberration balancing. Here, the convex side of lens 1 and the planar side of lens 2 must face the laser beam to cancel part of the aberration. The most significant shortcoming for this three-lens system is its alignment sensitivity. In addition, light intensity is somewhat reduced after the beam passes from this multiple lenses arrangement. So, this system was used only for those experiments which required a large field of view.

III-3. Results and Discussion

Homalite-100 is a rate sensitive viscoelastic solid and its wave speeds depend on stain rate as indicated in Table 1. Wave speed differences of approximately 17% are expected over six orders of magnitude differences in equivalent strain rate. In order to obtain a more accurate measure of the wave speed levels relevant to our impact experiments, a calibration test was undertaken. A Homalite plate was impacted at a projectile speed of 24 m/s and the impact area was imaged by the high-speed camera. The photoelastic fringe pattern corresponding to this dilatational front spread through the material and the location of its front was traced and plotted as a function of time (see

Figure 5). The resulting linear variation reveals a constant dilatational wave speed of approximately 2119 m/s which, for a Poisson's ratio of 0.35, corresponds to a shear wave speed of 1208 m/s and a Rayleigh speed of 1110 m/s. Fringe patterns of the type shown in Figure 5 have also allowed us to estimate the local strain rate at the impact point. For the impact speeds used in this paper, the strain rate was found to be of the order of 10^3/s. As expected these values are higher than the ones corresponding to a quasi-static loading (strain rate ~ 10^{-3}/s) and are listed in a separate column of Table 1. From now on indicated wave speeds will correspond to the above measured dynamic values.

III-3.1 The Two-layer Specimen with Equal Layer Widths Subjected to Mitigated Projectile Impact

Figure 6 shows a series of photoelasticity snap shots following impact of a type-A specimen. In all experiments reported in this section, the projectile impacted the center of the bottom layer on a steel buffer as shown in Figure 6 (a). The horizontal line in the field of view reveals the position of the interface in which the dark circular spot, at the lower left-hand side just below the interface, is a scaling mark of 6.35 mm in diameter. Figure 6 (b) shows a fan of mode I cracks (symmetric fringe patterns) appearing from the upper free edge at approximately 93.8 μs after impact. Generally, the whole recording system has a delay and its timing error is within 10 μs. After impact, the longitudinal compressive stress wave traveled from the lower impact side towards the upper free edge. This compressive stress wave reflected from this edge as a tensile wave and its intensity was sufficient to nucleate a fan of branched cracks from the free edge. As time goes on

(Figure 6 (c)-(f)), the nucleated fan of cracks widens significantly by producing a multiplicity of both successful and unsuccessful branches (for a discussion of crack branching phenomenon in bulk Homalite, see Ravi-Chandar and Knauss[10]), some of which move towards the still coherent interface. The average speed of these locally mode I, branched cracks is 0.41 C_S, which is the branching speed in bulk Homalite.

Well before the branched cracks reached the interface, a central inter-layer crack was nucleated at the intersection of the specimen center line and the bond line as seen in Figure 6 (c). This interfacial crack propagated in both directions off the center as shown in Figure 6 (d). At the specimen centerline, the shear stresses vanish because of symmetry. As a result, the nucleated inter-layer crack is initially and, for a very short time, mode I dominated. Its nucleation is induced by the stress field produced by the fan of branched cracks approaching the interface. As this crack spreads symmetrically, opening up the interface (see distinct evidence of decohesion in Fig. 6 (f)), the fan of branched cracks discelerates and arrests just before these cracks reach the decohered interface. The above described scenario is perhaps the first real-time visualization of the dynamic equivalent of the "Cook-Gordon Mechanism"[12] describing the remote decohesion of an interface due to the approach of a matrix (intra-layer) crack.

As the interfacial crack spreads away from the specimen centerline, it almost immediately encounters increasing amount of interfacial shear stress, which quickly converts it to a mixed-mode and eventually to a mode II dominated crack. Unlike propagating cracks in bulk Homalite, interfacial cracks are constrained to propagate along the weak interface and, as a result, they can do so under mixed-mode or primarily mode II conditions. They can also propagate at very high (even intersonic) speeds compared to

their bulk (intra-layer) counterparts. This phenomenon has recently been investigated experimentally by Rosakis et al.[13] and numerically by Needleman[14] and by Geubelle and Kubair[15]. To illustrate this point, the variation of the left interfacial crack tip position versus time and the corresponding crack tip speed are plotted in Figure 7 (a) and (b) respectively. Indeed this figure shows very high interfacial crack tip speeds initially well within the intersonic regime (crack speed is greater than the shear wave speed but less than the longitudinal wave speed of the bulk material), later decelerating to a large fraction of the Rayleigh wave speed. This observation is consistent with the surmised shear-dominated nature of this crack (see Geubelle and Kubair[15]). If this inter-layer crack is, at least for short times, intersonic, the photoelastic images obtained here should reveal the existence of shear shock wave discontinuities emitted from the propagating crack tips and inclined at an angle $\beta = \sin^{-1}(Cs/V)$ to the interface (Rosakis et al.[13]). Indeed, a close look at Figure 6 (d) and (e) reveal the existence of such shear shock waves which are shown in detail in Figures 8 (a) and (b). The angle β can now be used to provide an independent measure of the ratio; V/Cs of the instantaneous crack tip speed to the shear wave speed. This ratio is plotted in Figure 8(c) as a function of time (black triangles). For comparison purposes, the same ratio, obtained from the independent measurement of the crack length record is also shown. The two sets of points are obtained by using crack speeds from Figure 7 and the quasi-static and the dynamic values of Cs, from Table 1, respectively. As evident from this composite plot, the trends are very consistent. Differences are due to experimental errors introduced through differentiating the crack length record, and uncertainties in shear wave speed choice. Indeed very near the crack tip where the strain rates are very high, the dynamic values of shear wave speed should

be used; while further away the static values may be more appropriate for shock angle estimation (Abraham and Gao[16]).

Additional evidence of the shear-dominated nature of the interfacial cracks is provided by the nucleation and growth of a periodic array of secondary microcracks observed to occur along the bond at a certain distance from the centerline of the specimen (see Figure 6 (f)). These microcracks are generated just behind the propagating shear crack tip (see Figure 9) and spread at a steep angle of approximately 11 degrees to the normal of the bonded interface. They are locally mode I cracks and they grow only at the bottom layer side of the interface indicating that this layer is primarily in tension along the horizontal direction. Their opening nature is evident from the existence of symmetric and almost circular caustics surrounding their tips (see Figure 9). The generation of such secondary cracks following shear interfacial crack growth was first discussed by Rosakis et al.[17] and Samudrala, Huang and Rosakis[18] in connection to intersonic shear rupture of Homalite/Homalite interfaces. As discussed in these references, their 11 degrees inclination indicates the existence of frictional contact and sliding behind the growing shear crack faces, which slightly change the principal stress directions responsible for path selection for the microcracks.

For the present discussion, the existence of such secondary cracks in impacted layered specimens is also very important. It shows how different failure modes (some symmetric and others shear-dominated) may interact and trigger each other in a non-straightforward way to result in the final brittle failure of a layered structure. Indeed in the processes discussed above, damage was first initiated by the mode I dominated fan of branched cracks moving towards the interface. Without penetrating the interface, this fan

of opening crack induced inter-layer failure which in turn transitioned from an opening mode to a shear mode as it moved away from the centerline and as it delaminated the interface. Finally, it was this shear-dominated delamination stage which made it possible for the periodic sequence of opening microcracks to penetrate the bottom layer and cause its final fragmentations.

III-3.2 The Two-layer Specimen With Equal Layer Widths Subjected to Direct Projectile Impact

Figure 10 shows a series of images for a two-layer specimen subjected to direct projectile impact. Stress wave propagation and reflection from the top free edge is shown in Figure 10 (b). The fringe pattern at the bonded interface is continuous and does not even exhibit any discontinuities in slope. This implies a good bonding and matched material properties of the Homalite and the bonding adhesive. Unlike the previous specimen with a mitigating steel buffer at the impact point, a dark zone of diffuse damage was observed at the impacted side. This dark zone is a highly compressed zone of comminuted material created by the direct projectile impact. Due to the large out-of-plane deformation, the light rays transmitted through this area cannot be collected by the high-speed camera thus producing a massive shadow spot. It is also noticed that a "plastic deformation ring," initially propagating at approximately 118 m/s, appeared at approximately 76 μs (Figure 10 (c)). Across this ring, permanent discontinuities of the fringe pattern were observed, indicating the irreversible damage nature within this semi-circular region. At the first stages of its evolution, the plastic semi-circle was smooth and

transparent. As time evolved several radial mode I cracks radiating from the impact point crossed the ring boundary moving towards the upper free edge of the specimen. With increasing time, the initial transparency of the plastically deformed area surrounded by the ring was compromised by the spreading of more complex three-dimensional damage modes. This became obvious through post-mortem inspection of the impacted plates where large 3-D surface cracks propagating in the specimen thickness (parallel to the plate free surface) were identified. It is their evolution of such cracks and their slightly wavy nature that produce the "shell" like structure of the further damaged plastic semi-circle in Figure 10 (e) and (f).

III-3.3 Failure Process in A Two-layer Specimen with Unequal Layer Widths

Post-mortem pictures of damage resulting from impact of two, type-B, specimens are shown in Figures 11 (a) and (b). The only difference between these two specimens, subjected to identical impact histories, is the strength of interfacial bonding. It is obvious from this figure that the interfacial bonding plays a significant role in the overall dynamic failure process. For the specimen with the intermediate strength interface as shown in Figure 11 (a), there are many branched, locally mode I, cracks radiating from the site of impact. Some of these I cracks only passed through the interface and did not cause any debonding. In contrast, the specimen with the weak interface, shown in Figure 11 (b), features fewer cracks radiating from the site of impact. Two of these cracks arrested at the weak interface, while the third produced only partial interfacial debonding.

Figure 12 shows a sequence of real-time images of the dynamic failure progress of the layered Homalite structure (type-B) featuring only one weak interface bond. This

case corresponds to the post-mortem pattern of Figure 11 (b). In this sequence, the top horizontal line is the interface while the bottom line is a camera streak line of no significance to the physical process. Figure 12 (b) reveals that the number of fringes or the stress wave gradient across the interface was dramatically reduced by the thin but soft adhesive film of 20 μm in thickness. After a long time period (380 μs) of wave motion within these two layers, a crack initiated from the dark impact zone was observed near the site of impact. This crack accelerated and eventually branched as shown in Figure 12 (d). As soon as the resulting branches approached the interface, they either arrested or turned into it producing partially interfacial debonding as shown in Figures 12 (e) and (f). The exact reasons of the inability of these cracks to penetrate the upper layer are complex and are currently under investigation. However, the pivotal role of the weak interface in triggering this behavior is clearly evident. This may provide a useful design methodology to prevent the spread of impact damage resulting from low speed projectiles. In an early study of impact mechanisms of composite laminates, Sun and Rechak[19] investigated a similar phenomenon by placing adhesive layers between plies, and thus delaying or even suppressing dynamic delamination.

In the case discussed above, the impact side was far away from the interface. If we now use the same specimen geometry and projectile loading history but instead impact the side close to the bonded interface, the resulting failure patterns are very different. This is evident from the post-mortem reconstructions of three bi-layer specimens (impacted close to the interface) with the same geometrical dimensions but different interfacial bonding strengths, which are presented in Figure 13. It should first be emphasized that two identical specimens with the same interfacial bonding have quite

different failure patterns if the impact location is reversed. This is evident by comparing Figure 11 (a) with Figure 13 (b) as well as Figure 11 (b) with Figure 13 (c). Differences are most pronounced for specimens with intermediate strength bonding shown in Figures 11 (a) and 13 (b). Indeed more radial cracks were found and more extensive interfacial debonding occurred when the specimen was impacted closer to the bond. In the case shown in Figure 13 (b), it is also observed that cracks radiating from the impact point approached the bond with different incident angles (the angles between the crack path and the interface) and triggered a variety of subsequent failure behaviors. Those cracks with large incident angles penetrated the interface, but those cracks with small incident angles deflected into the interface and led to shear-dominated debonding, similar to the shear decohesion phenomenon discussed in section 3.1. Here again, a close look at the upper side of the decohered interface reveals a periodic sequence of tensile microcracks inclined at small angles to the interface normal. These tensile microcracks are again generated as some of the radial cracks deflect into the interface, becoming shear-dominated and decohering it through a process of dynamic shear failure. The microcracks are generated just behind the growing shear interfacial cracks at the tension side of the interface. A real-time view of the failure process corresponding to an intermediate strength bond is provided in Figure 14. The first failure event visualized in this sequence is the zone of comminuted and plastically deformed materials (dark area) as evident from Figure 14 (b). As time progresses, more than ten intra-layer radiating cracks appear and most of them pass through the interfacial bonding. The radial cracks that approached with a smaller incident angle, and were deflected into the interface, moved along it with

higher speeds as evident by the elongated shape of the failure front arc shown in Figure 14 (c).

III-3.4 Failure Process in A Three-layer Specimen with Equal Layer Widths

Failure patterns became more complicated as a second interface was introduced to construct the three-layer specimens (type-C), shown in Figure 15. Figures 15 (a) and (b) display post-mortem images of damage of two identical specimens featuring a strong bottom interface and a top interface of two different (intermediate and weak) strengths respectively. For the specimen with intermediate top interface (Figure 15 (a)), radial cracks initiated at the impacted layer and passed through the lower (strong) and the upper (intermediate) interfaces. Also, several cracks were able to cross all the way to the layer farthest from the impact side. In contrast, the specimen with the weak top interface, shown in Figure 15 (b), featured fewer radial cracks on the impacted side. Also those cracks arrested at the upper weak interface and did not penetrate into the upper layer. Extensive interfacial debonding at the upper interface was observed. The two specimens in Figure 15 (a) and (c) are identical except for the choice of impact side. In Figure 15 (a), the impact side is closer to the strong interface. So the radiating cracks mainly passed through this strong interface, causing debonding, only in the central portion of the specimen. Again debonding is shear-dominated because microcracks are visible along this decohered part of the strong bond.

A real-time view of the failure process of the specimen in Figure 15 (a) was presented in Figure 16. In Figure 16 (b) the stress wave propagates through both upper and lower interfaces without experiencing any strong fringe or weak fringe slope

discontinuities. In these photographs, the central thin line adjacent to the small circular mark is the camera streak line and is an artifact of the optical setup. The other two thin lines represent strong and intermediate strength interfaces. A group of radial cracks soon propagate through the lower, strong, interface as shown in Figure 16 (d) and (e). Those radiating cracks with large incident angles passed through the lower, strong interface and subsequently penetrated the upper, intermediate strength interface. Those few cracks that approached with smaller incident angles were deflected into the interface and one of them (moving to the right) is clearly shown in Figure 16 (d). To illustrate this phenomenon, an enlarged part of the specimen shown in Figure 15 (c) is presented in Figure 17. For two cracks with different incident angles, different failure events were observed. The crack with the large incident angle of 78 degrees passed through the interface. However, the crack with the small incident angle of 50 degrees could not penetrate the interface and created interfacial debonding. A systematic study of this problem is presently underway by the authors[20].

We now turn attention to tri-layer specimens involving at least one weak bond (the 5083 adhesive in Table 2). As clearly shown in Figure 18, this adhesive is weak and ductile enough (see section 2.1) never to allow crack penetration into the next layer under low-speed impact. In Figure 18 (a) some radial cracks from the impact region penetrate the intermediate strength bond of the lower interface (primarily near the center where the incident angle is large). Some interfacial debonding also occurs and is triggered by the radial cracks that approach the interface with more shallow angles. However, the situation at the upper, weak interface is very different. As radial cracks approach the weak bond, they are completely arrested neither penetrating nor causing debonding of

this second interface. This is also found to be true in all other cases (such as Figure 18 (b) and (c)) where such a weak and ductile bond is involved. In all of these cases, the bond was never penetrated nor was there any visible decohesion, at least at an impact speed of 21 m/s. This speaks of an apparent ductility of this bond whose extend will be investigated next.

In order to further test the impact resistance of specimens with 5083 weak but ductile adhesive bonds, a three-layer specimen containing two identical 5083 interfaces was designed and subjected to different impact speeds. The post-mortem pictures are shown in Figure 19. The impact speeds were 20 and 46 m/s respectively. Although the size of the local impact damage zone is quite different, in both cases the bond was again neither penetrated nor compromised. The impact damage is still limited inside the layer impacted directly by the projectile. The other two layers are still perfectly bonded.

To understand the effect of the introduction of a ductile adhesive bond as a mechanism for failure prevention, real-time visualization was undertaken in Figure 20. As shown in Figure 20 (b), the stress wave intensity across the interface was reduced dramatically after the first interfacial 5083 bonding was encountered. In Figure 20 (c), the stress wave intensity was further reduced after the second 5083 interface was crossed. Meanwhile, complicated stress wave movement is seen in Figure 20 (d) and the dark contact zone is continuously growing. Radial cracks are initiated from the impact point very early (around 70 μs) compared to the other three-layer specimens shown in Figure 16. However, those cracks soon arrested at the interface as seen in Figure 20 (e) and (f). No interfacial debonding was found in this type of specimens. In our investigation, only low impact speed tests were conducted.

III-4. Summary and Conclusions

We investigate the generation and time evolution of dynamic failure modes in layered materials composed of bonded layers of Homalite-100. We observe a variety of dynamic failure mechanisms in the form of either intra-layer (matrix) cracks or inter-layer (interfacial) cracks or debonding. Dynamic intra-layer failure is always of the symmetric (mode I) type and it often involves multiple branching events. Dynamic inter-layer fracturing or debonding is almost always shear-dominated and spreads at much faster speeds that intra-layer failure. One of the themes common to all cases studied here is the interrelation and interaction between these different symmetric and asymmetric failure modes. Indeed it is often the case that symmetric (mode I) intra-layer cracks approaching an interface (even if they never penetrate it) trigger mixed-mode or mode II interfacial delaminations, which in turn laterally spread mode I damage by an interesting mechanism of microcrack formation. In other cases, and depending on relative bond strengths and angles of incidence, intra-layer (matrix) cracks may clearly penetrate an interface without delaminating it.

In this paper, we explore some of these phenomena, and their interrelation, in perhaps the simplest, non-trivial, setting possible. We intentionally choose layers of identical material constitution in order to eliminate wave speed and other property mismatches across interfaces. We instead concentrate in varying bond strengths, layer geometry and to some extend impact speed. The above described, real-time observations of failure modes in layered solids, in addition to identifying some new basic failure

phenomena, can perhaps serve as benchmark experiments for the validation of complex numerical codes designed to model dynamic failure of layered structures.

Acknowledgements

The authors gratefully acknowledge the support of the Office of Naval Research (Dr. Y. D. S. Rajapakse, Project Monitor) through a grant (#N00014-95-1-0453) to Caltech.

.

References

1. Hutchinson, J. W. and Suo, Z., Mixed Mode Cracking in Layered Materials. *Advances in Applied Mechanics*. 29 (1992) 63-191.

2. Abrate, S., Impact on Laminated Composites: Recent Advances. *Applied Mechanics Reviews*. 47 (1994) 517-544.

3. Takeda, N., Sierakowski, R. L., Ross, C. A. and Malvern, L. E., Delamination-crack Propagation in Ballistically Impacted Glass/Epoxy Composite Laminates. *Experimental Mechanics*. 22 (1982) 19-65.

4. Espinosa, H., Lu, H.-C., and Xu, Y. A Novel Technique for Penetrator Velocity Measurement and Damage Identification in Ballistic Penetration Experiments. *J. of Composite Materials*, 32 (1998) 722-43.

5. Riley, W. F. and Dally, J. W., A Photoelastic Analysis of Stress wave Propagation in a Layered Model. *Geophysics,* 31 (1966) 881-99.

6. Xu, L. R. and A. J. Rosakis, Impact Failure Characteristics in Sandwich Structures; Part I: Basic Failure Mode Selection, Submitted to *International Journal of Impact Engineering* (2001).

7. Dally, J. W., Dynamic Photoelastic Studies of Fracture. *Experimental Mechanics*, 19 (1979) 349-61.

8. Kobayashi, A. S. and Mall, S., Dynamic Fracture Toughness of Homalite-100. *Experimental Mechanics*, 18 (1978) 11-18.

9. Ramulu, M. and Kobayashi, A. S., Mechanics of Crack Curving and Branching ---A Dynamic Fracture Analysis. *International J. of Fracture*, 27 (1985) 187-201.

10. Ravi-Chandar, K., and Knauss, W. G., An Experimental Investigation into Dynamic Fracture: III. On Steady-state Crack Propagation and Crack Branching. *International J. of Fracture*, 26 (1984) 141-54.

11. Xu, L. R. and Rosakis, A. J. Comparison of Static Tensile and Shear Strengths and Fracture Toughness of Various Adhesive Bonds between Elastic Solids. (2001), In preparation.

12. Gordon, J. E., *The New Science of Strong Materials*. Second Edition, Pitman Publishing Limited. London, UK. 1976.

13 Rosakis, A.J., Samudrala, O. and Coker, D., Cracks Faster than Shear Wave Speed. *Science*, 284 (1999) 1337-1340.

14. Needleman, A. An Analysis of Intersonic Crack Growth under Shear Loading. *J. of Applied Mechanics*, 66 (1999) 847-857.

15. Geubelle, P. H. and Kubair, D. Intersonic Crack Propagation in Homogeneous Media under Shear-dominated Loading: Numerical Analysis. *J. Mech. Physics Solids, 49* (2001) 571-587.

16. Abraham, F. F. and Gao, H., How fast can cracks propagate? *Physical Review Letters*, 84 (2000) 3113-3116.

17. Rosakis, A.J., Samudrala, O. and Coker, D., Intersonic Shear Crack Growth along Weak Planes, *Material Research Innovations,* 3 (2000) 236-243.

18. Samudrala, O., Huang, Y., and Rosakis, A.J., Subsonic and Intersonic Shear Rupture of Weak Planes with a Velocity Weakening Cohesive Zone, Submitted to *Journal of Geophysical Research* (2001).

19. Sun, C. T. and Rechak, S. Effect of Adhesive layers on Impact Damage in Composite Laminates. *Composite Materials: Testing and Design (Eighth Conference)*. ASTM STP 972, J.D. Whitcomb, Ed., American Society for Testing and Materials, Philadelphia, pp. 97-123, 1988.

20. Xu, L. R., Huang, Y. Y. and Rosakis, A. J. Dynamic Crack Deflection and Penetration at Interfaces in Homogeneous Materials: Experimental Studies and Model Predictions. In preparation.

List of Tables

List of Figures

Figure 9. A detailed view of the formation of secondary opening microcracks following shear dominated interfacial delamination.

Figure 10. Failure process of a two-layer specimen (2lhhsp384-1) subjected to direct projectile impact.

Figure 11. Post-mortem failure patterns of two identical specimens with different interfacial bond strengths subjected to the same impact speed of V=20 m/s. (a) 2LHHSP384-LT1 (two-layer system with 384 intermediate strength bonding and impact at the large width layer) (b) 2LHHSP5083-LT1 (with 5083 weak bonding).

Figure 12. Crack propagation and arrest at a two-layer specimen with 5083 weak bonding. The central black line is the camera streak reference line. The upper horizontal line is the only interface.

Figure 13. Post-mortem failure patterns of three bi-layer specimens with different interfacial bonding strengths subjected to the same impact speed of V=21 m/s. (a) 2LHHSP330-ST1 (b) 2LHHSP384-ST1 (c) 2LHHSP5083-ST2.

Figure 14. A group of cracks initiated and propagated in a bi-layer Homalite specimen (2lhhsp384-st1) with intermediate strength bonding. The lower thin line is the bonded interface. The upper horizontal line is a camera streak line.

Figure 15. Failure patterns of the three-layer specimens with different bonding and impact sides. (a) 3LHHSP330384-3302 (b) 3LHHSP330583-3301 (c)

3LHHSP330384-3841. Notice specimens (a) and (c) are identical cases except for the different impact sides.

Figure 16. Failure process of specimen 3LHHSP450384-3302. (The lower and upper thin lines are intermediate and strong interfaces.)

Figure 17. Intra-layer cracks hit the interface with different angles (specimen 3LHHSP330384-3841). The crack with a large incident angle penetrated the interface while the crack with a small incident angle deflected at the interface.

Figure 18. Comparison of final pattern of the three-layer specimens with 5083 bonding with the same impact speed of 21m/s. (a) 3LHHSP384583-3841 (b) 3LHHSP330583-5831 (c) 3LHHSP384583-5831.

Figure 19. Effect of the impact speed to failure patterns of the three-layer specimens featuring two weak but ductile adhesive bonds.

Figure 20. Impact damage progress and wave propagation in a three-layer specimen featuring two 5083 weakly bonded interfaces (3LHHSP583-2).

Table 1. Material properties of Homalite –100

Property	Homalite 100	
	Static (Strain rate ~ 10^{-3}/s)	Dynamic (Strain rate ~ 10^{3}/s)
Density ρ (kg/m^3)	1230	1230
Young's modulus (GPa)	3.45	
Dilatational wave speed c_l (m/s) (plane stress)	1890	2119
Shear wave speed c_s (m/s)	1080	1208
Rayleigh wave speed c_R (m/s)	1010	1110
Poisson's Ratio ν	0.35	0.35
Material fringe constant f_σ (kN/m)	23.7	

Table 2. Interfacial strengths and model I fracture toughness of different bonds

Interface	Tensile strength σ_c (MPa)	Shear strength τ_c (MPa)	Fracture Toughness ($MPa*m^{1/2}$)	G_{IC} (J/m^2)
Homalite//Weldon-10// Homalite	7.74	>21.65	0.83	199.7
Homalite//330// Homalite	6.99	12.58	0.93	250.7
Homalite//384// Homalite	6.75	7.47	0.38	41.9
Homalite//5083// Homalite	1.53	0.81	0.19	10.5

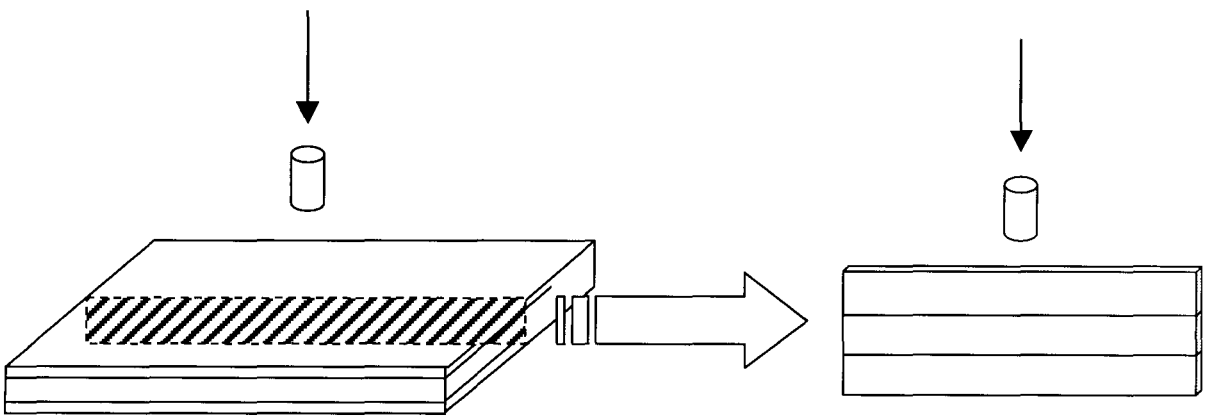

(a) 3-D out-of-plane impact problem

(b) 2-D impact problem

Figure 1. 3-D problem and plane stress idealization

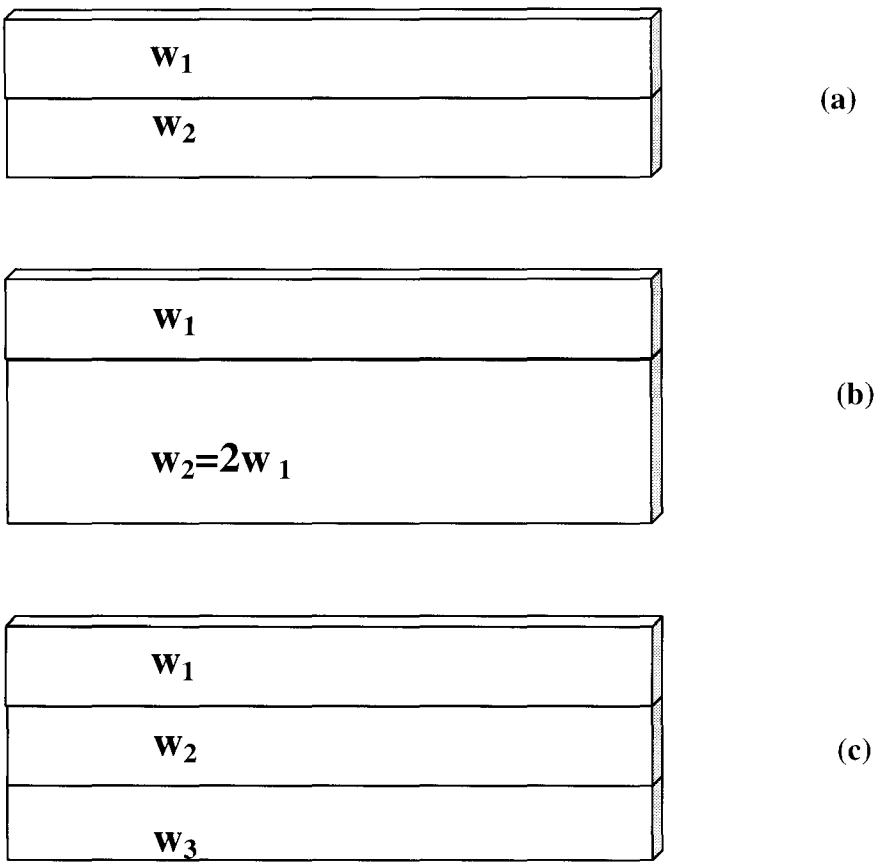

Figure 2. Model specimen geometries: (a) Two-layer specimens with equal widths (type-A) (b) Two-layer specimens with $W_2 = 2\ W_1$ (type-B) (c) Three-layer specimens with equal widths (type-C)

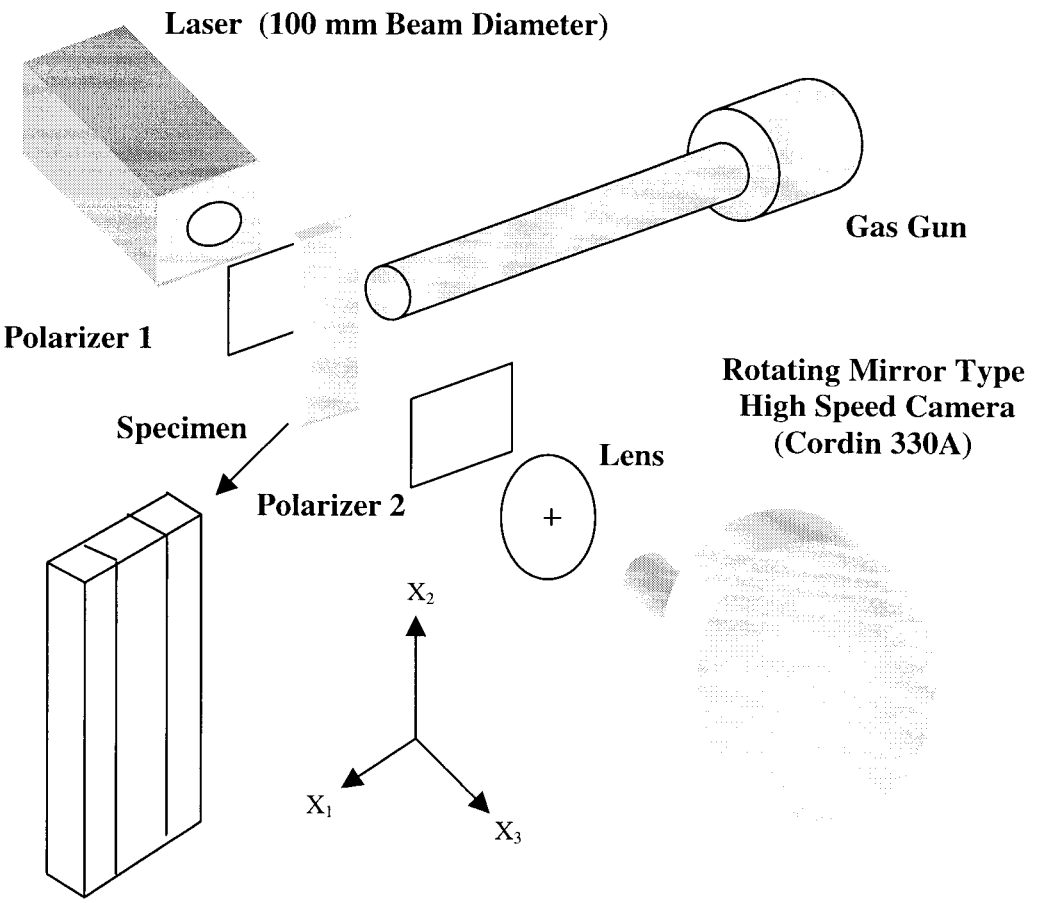

Figure 3. Schematic of the dynamic photoelasticity setup

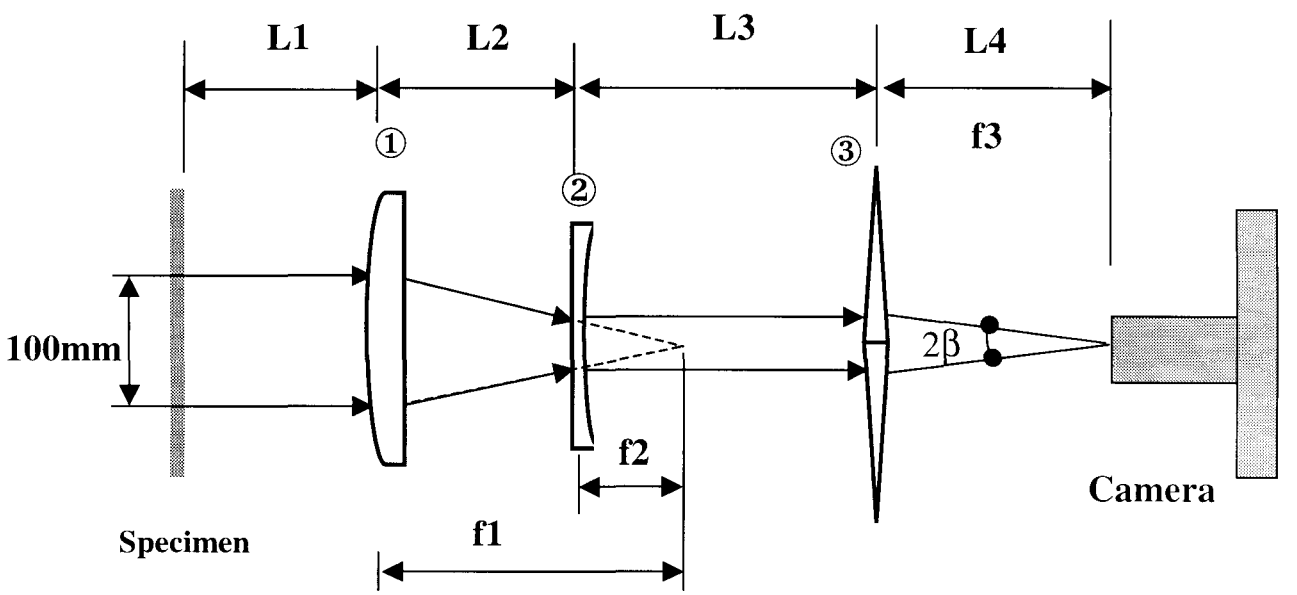

Figure 4. The three-lens system used in large field of view experiments. 1--- Plano-Convex lens. 2——-Plano-Concave lens. 3-----Bi-Convex lens

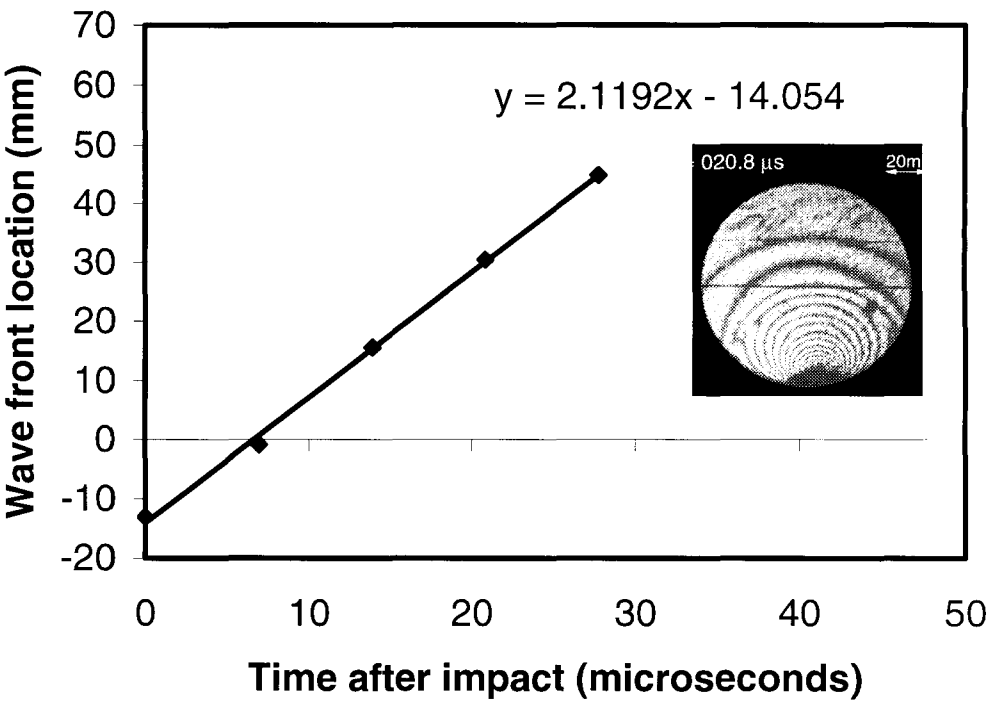

Figure 5. Measured stress wave front location verses time used to estimate the longitudinal wave speed of the Homalite-100 subjected to the current impact strain rate regime.

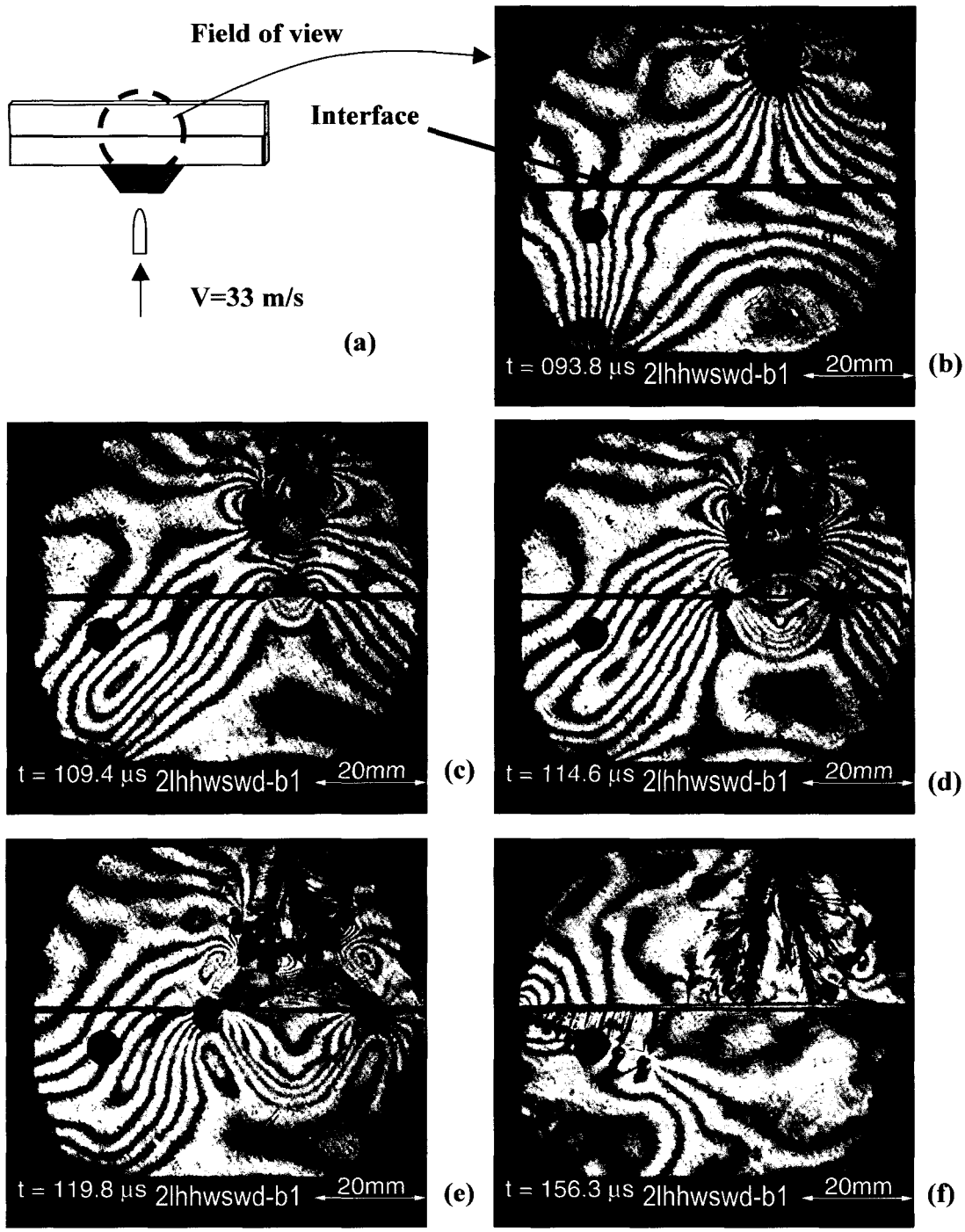

Figure 6. Dynamic failure process in a two-layer specimen showing the interaction of a fan of mode I incident cracks and the resulting interfacial crack. The thin horizontal line is the weak interface. The circular dot at the left low position in every photo is the scaling mark bonded on the specimen.

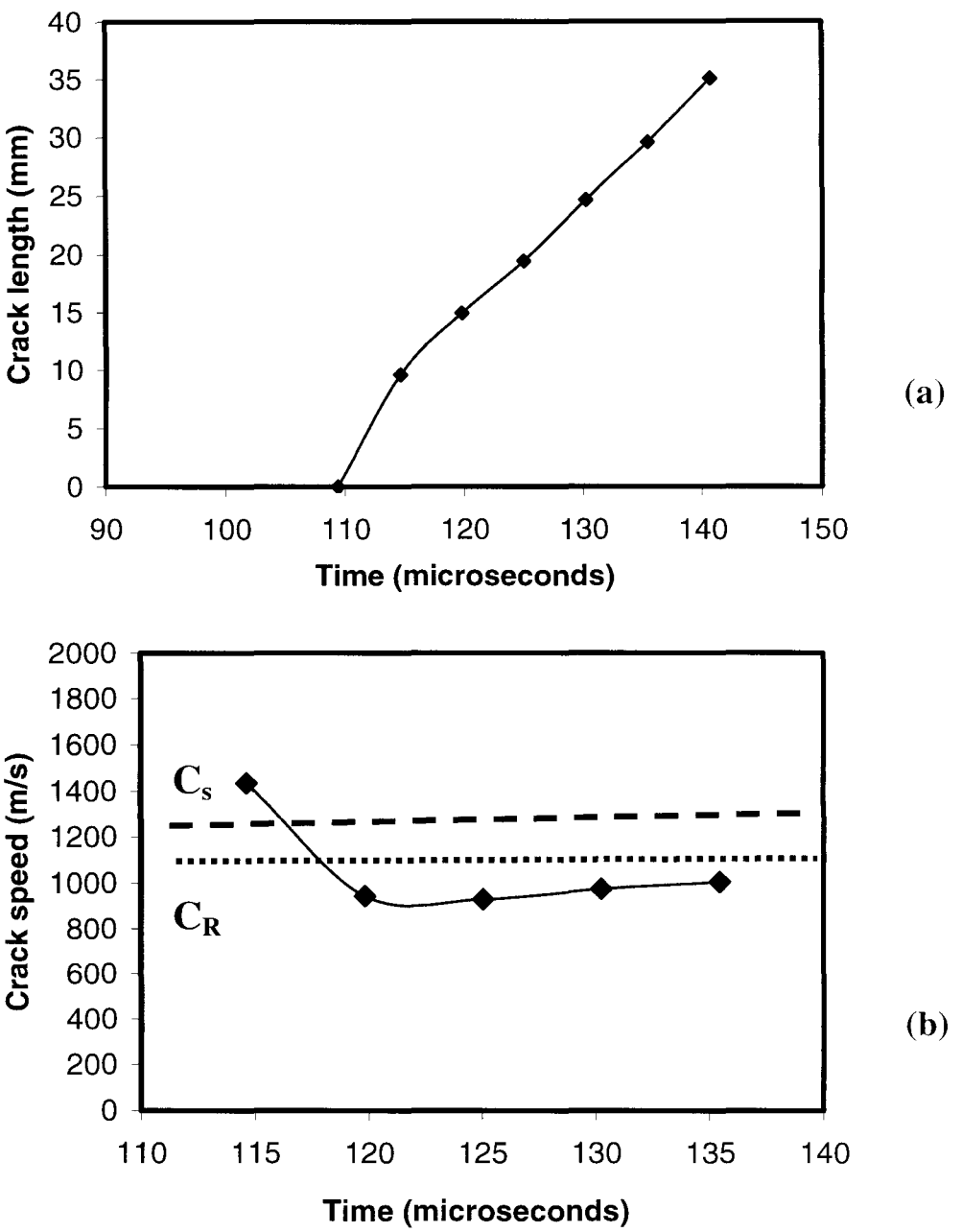

Figure 7. History of inter-layer crack length (a) and speed (b) of the two-layer specimen (2lhhwswd-b1). The two horizontal lines correspond to the dynamic values of the shear and Rayleigh wave speeds of the Homaite-100 shown in Table 1.

(a)

(b)

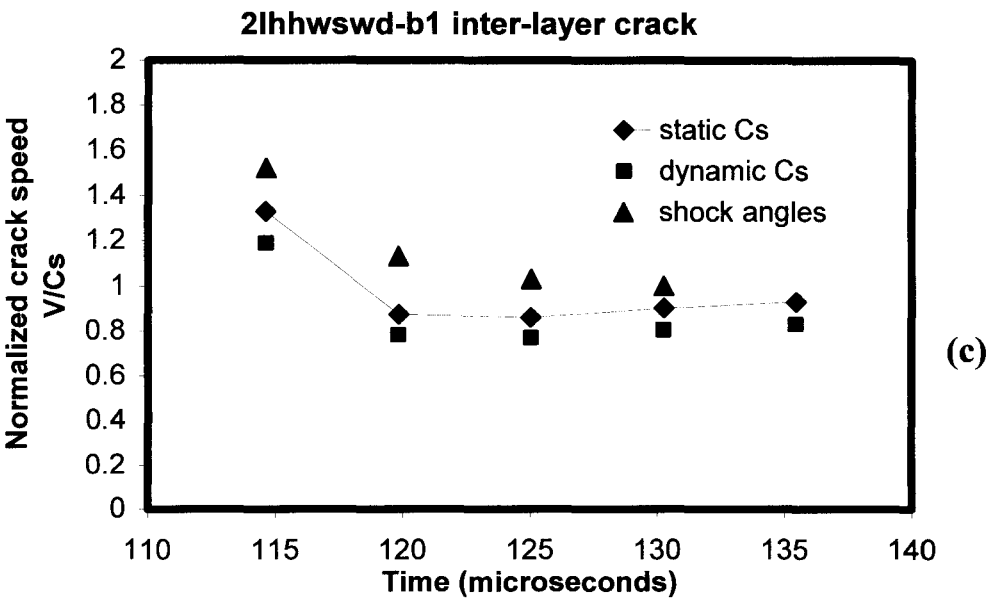

(c)

Figure 8. Early stages of intersonic, interfacial crack growth revealing the existence of shear shock waves (Figures (a) and (b)) and the estimated interfacial crack speeds using different methods (Figure (c)).

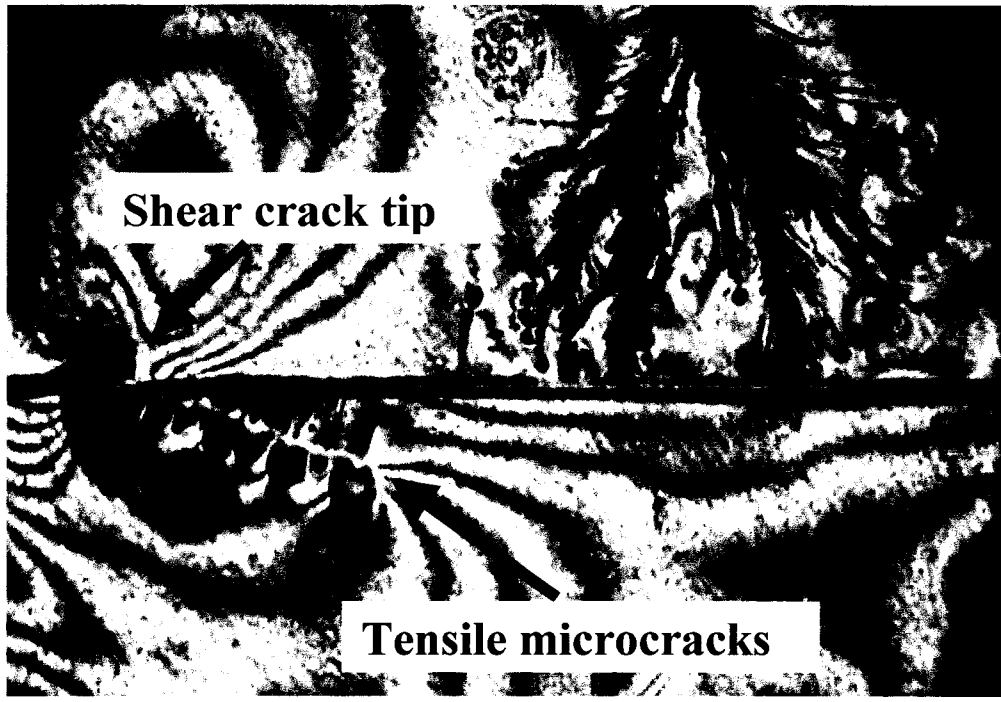

Figure 9. A detailed view of the formation of secondary opening microcracks following shear dominated interfacial delamination.

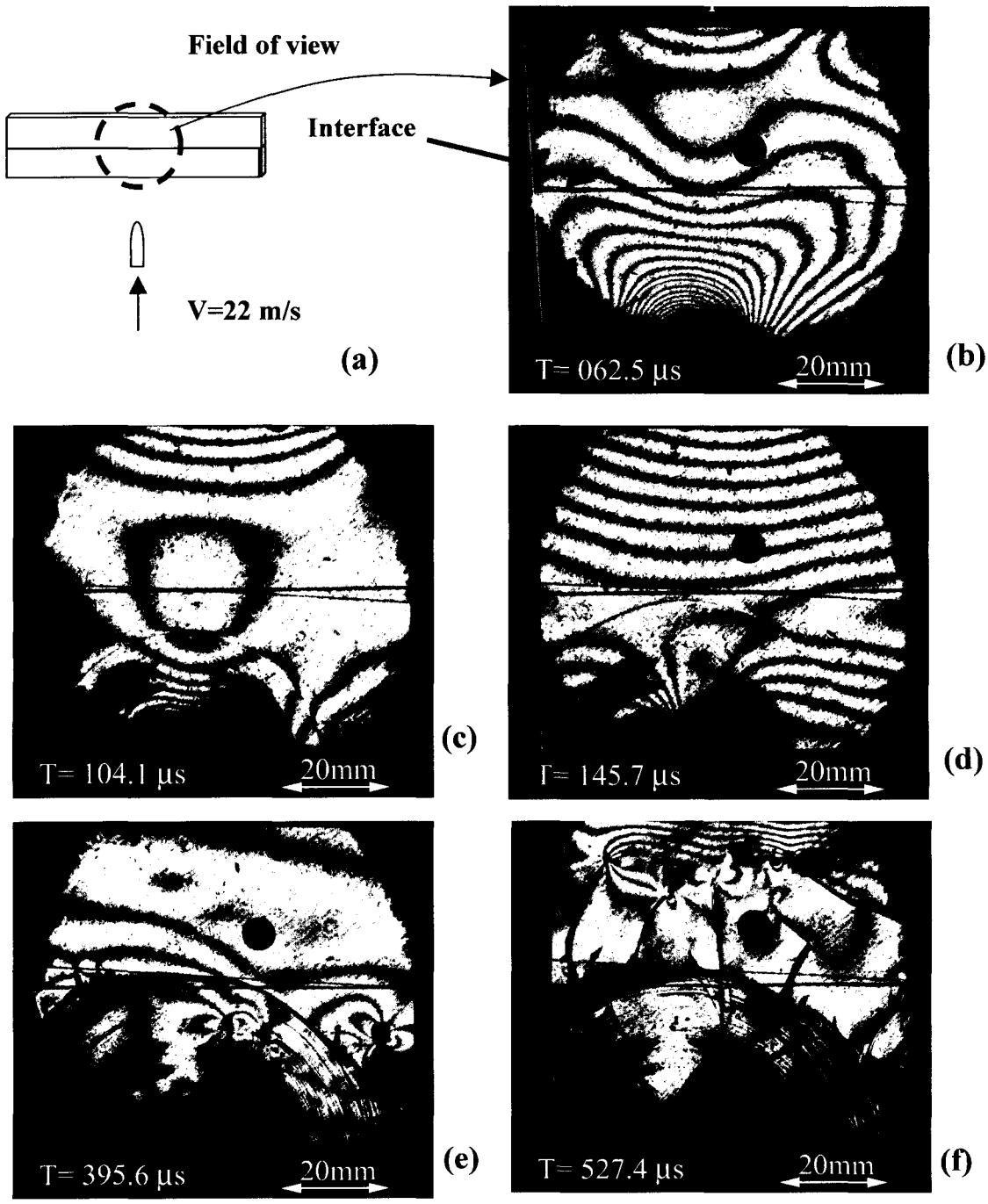

Figure 10. Failure process of a two-layer specimen (2lhhsp384-1) subjected to direct projectile impact.

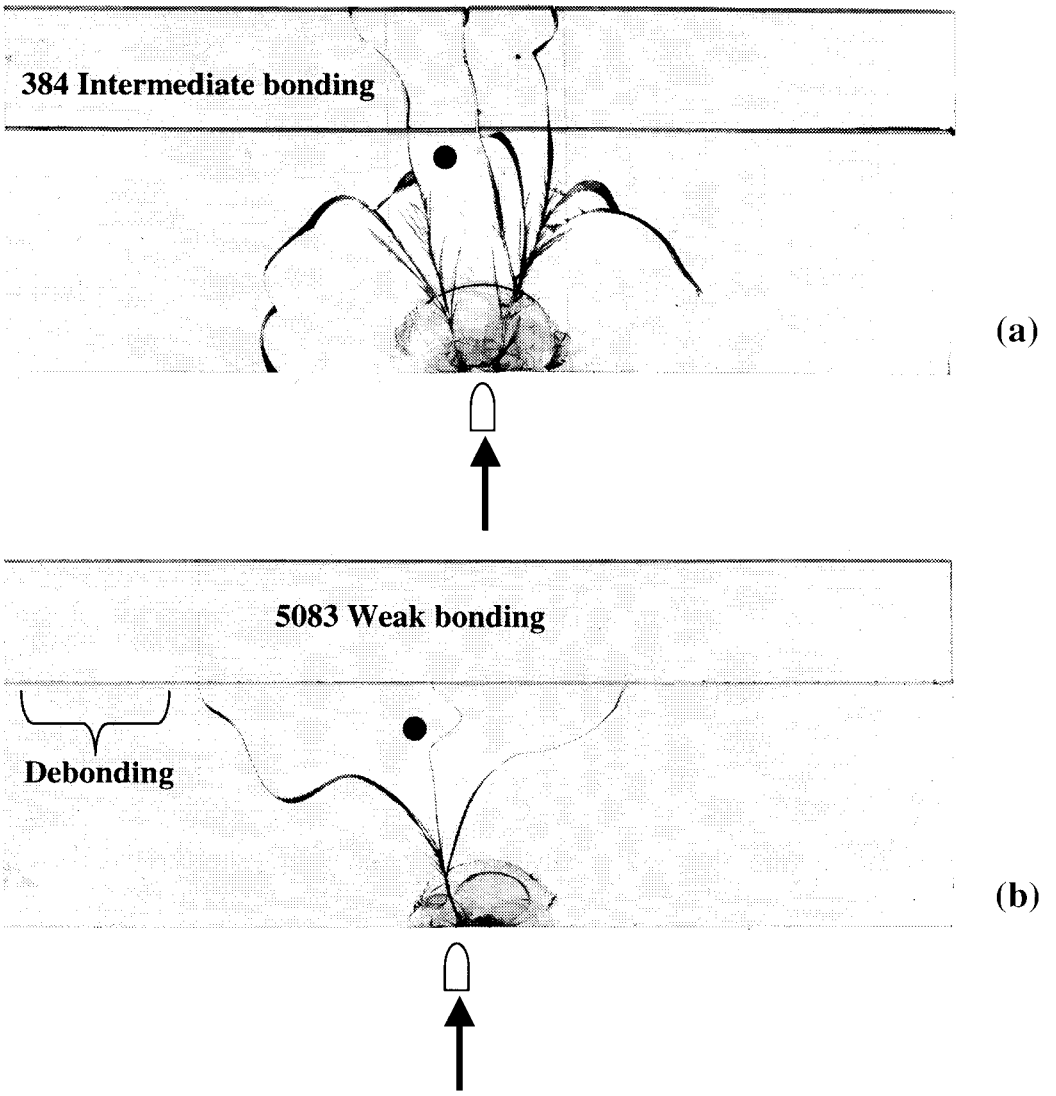

Figure 11. Post-mortem failure patterns of two identical specimens with different interfacial bond strengths subjected to the same impact speed of V=20 m/s. (a) 2LHHSP384-LT1 (two-layer system with 384 intermediate strength bonding and impact at the large width layer) (b) 2LHHSP5083-LT1 (with 5083 weak bonding).

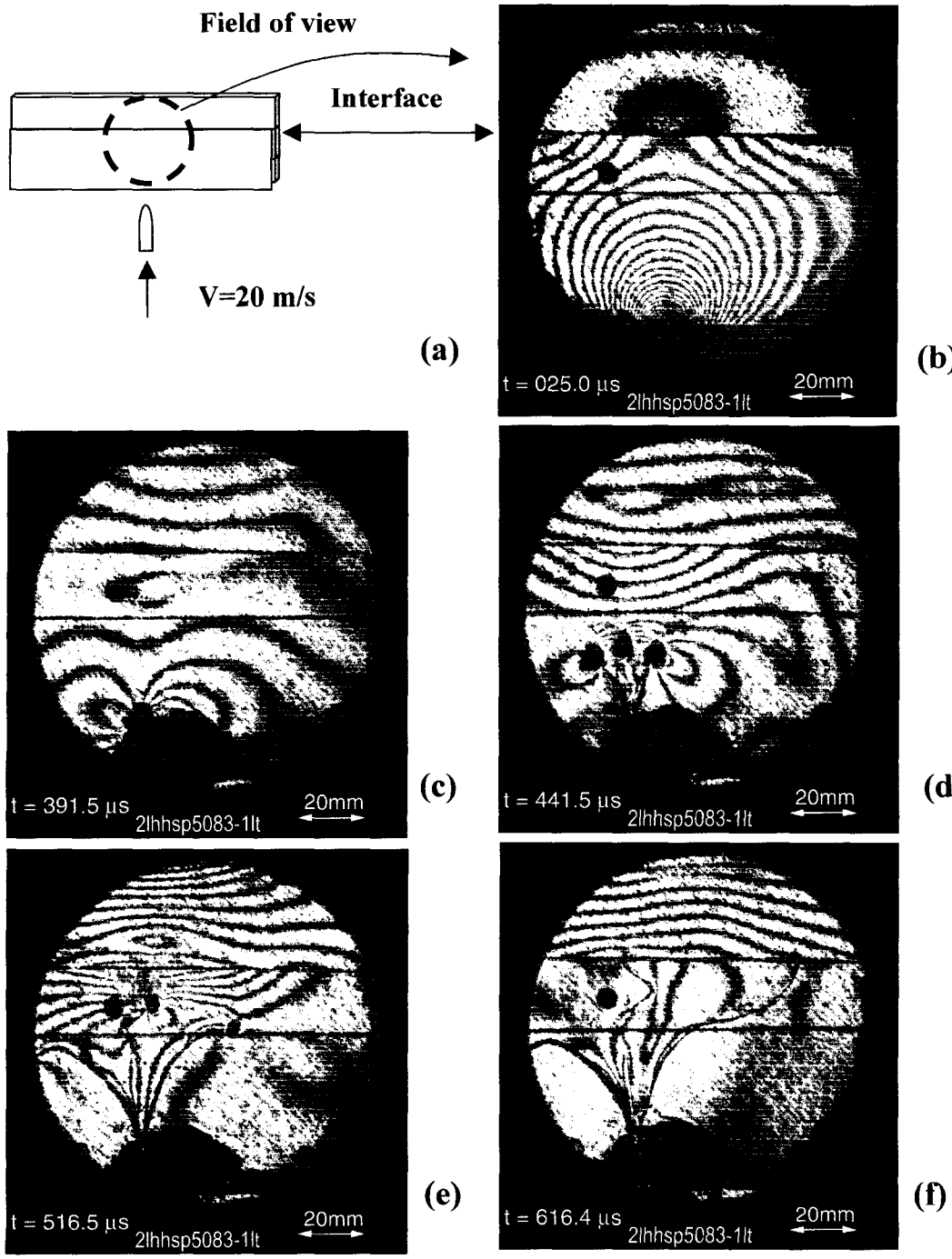

Figure 12. Crack propagation and arrest at a two-layer specimen with 5083 weak bonding. The central black line is the camera streak reference line. The upper horizontal line is the only interface.

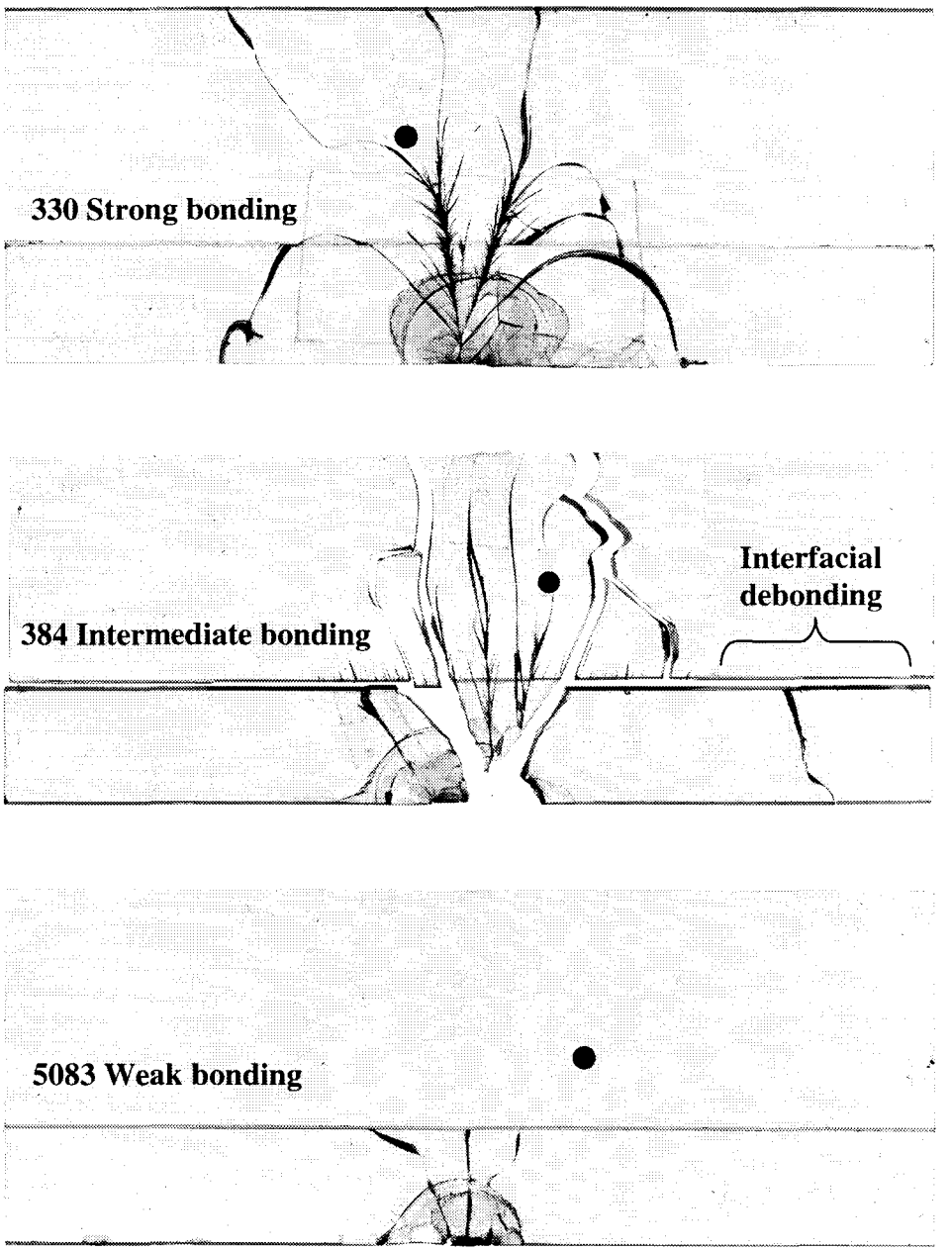

Figure 13. Post-mortem failure patterns of three bi-layer specimens with different interfacial bonding strengths subjected to the same impact speed of V=21 m/s. (a) 2LHHSP330-ST1 (b) 2LHHSP384-ST1 (c) 2LHHSP5083-ST2

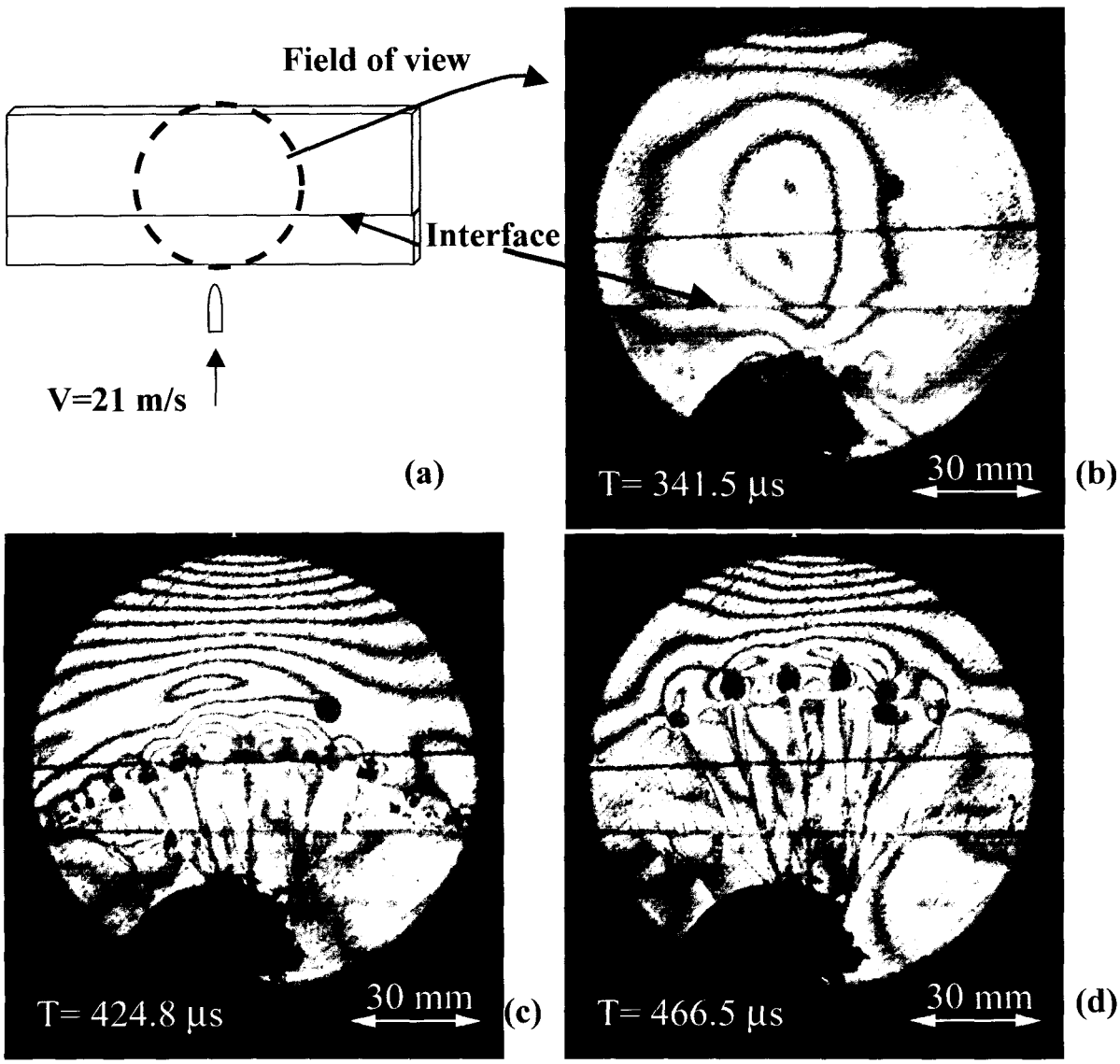

Figure 14. A group of cracks initiated and propagated in a bi-layer Homalite specimen (2lhhsp384-st1) with intermediate strength bonding. The lower thin line is the bonded interface. The upper horizontal line is a camera streak line.

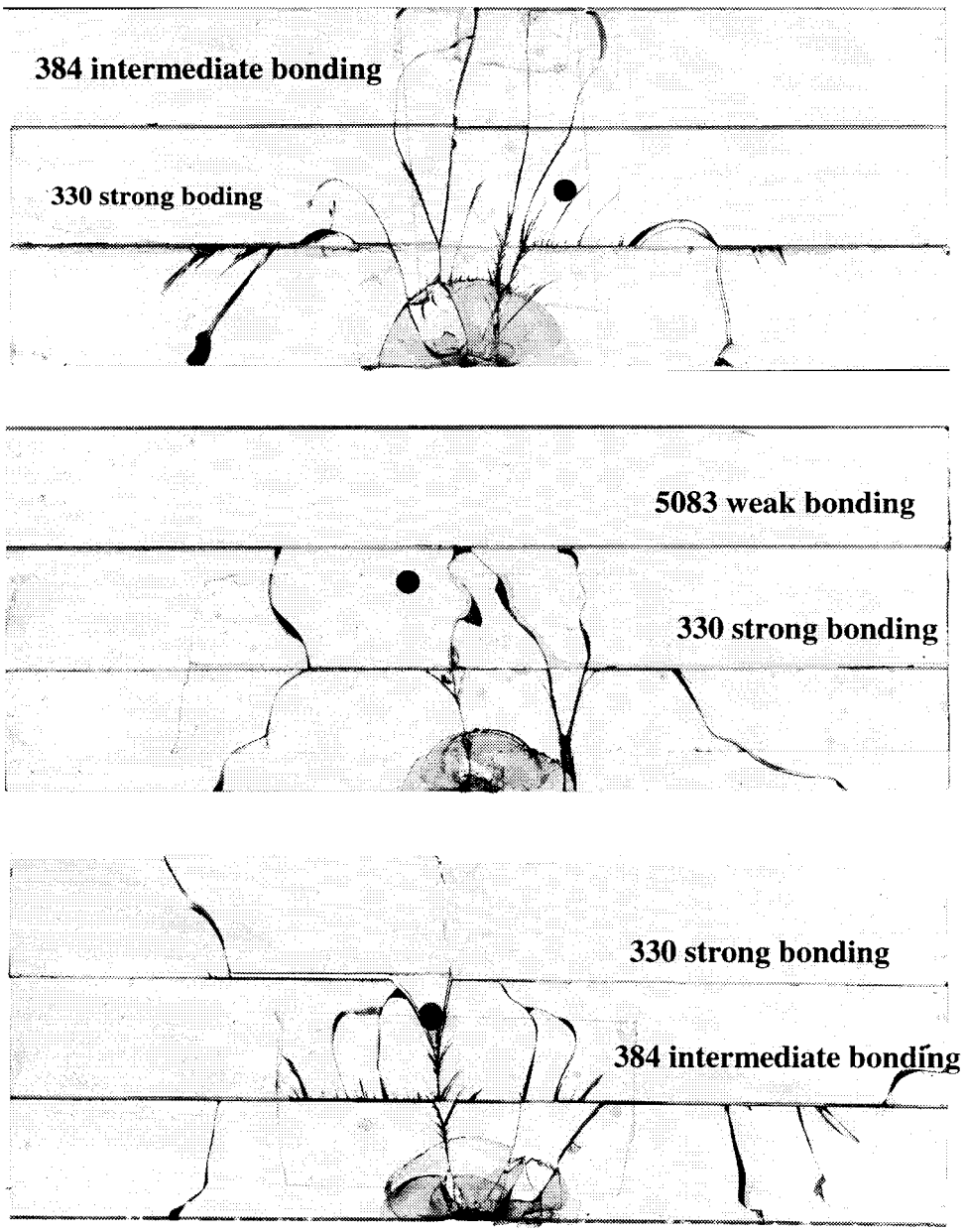

Figure 15. Failure patterns of the three-layer specimens with different bonding and impact sides. (a) 3LHHSP330384-3302 (b) 3LHHSP330583-3301 (c) 3LHHSP330384-3841. Notice specimens (a) and (c) are identical cases except for the different impact sides.

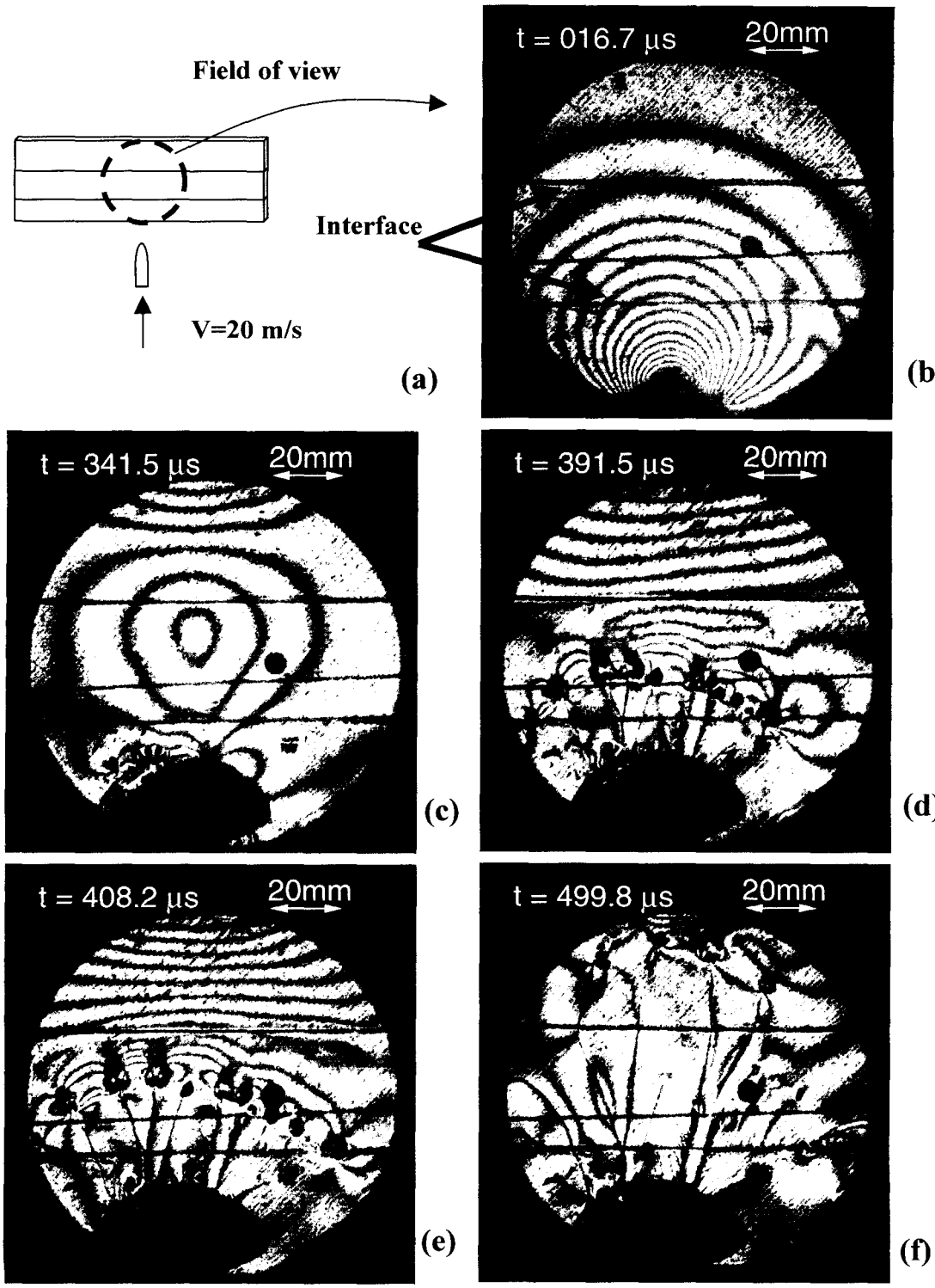

Figure 16. Failure process of specimen 3LHHSP450384-3302. (The lower and upper thin lines are intermediate and strong interfaces.)

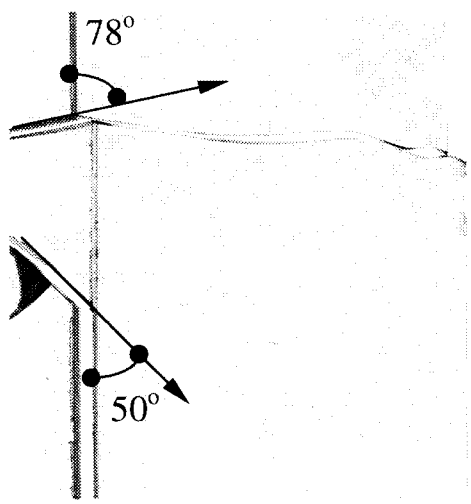

Figure 17. Intra-layer cracks hit the interface with different angles (specimen 3LHHSP330384-3841). The crack with a large incident angle penetrated the interface while the crack with a small incident angle deflected at the interface.

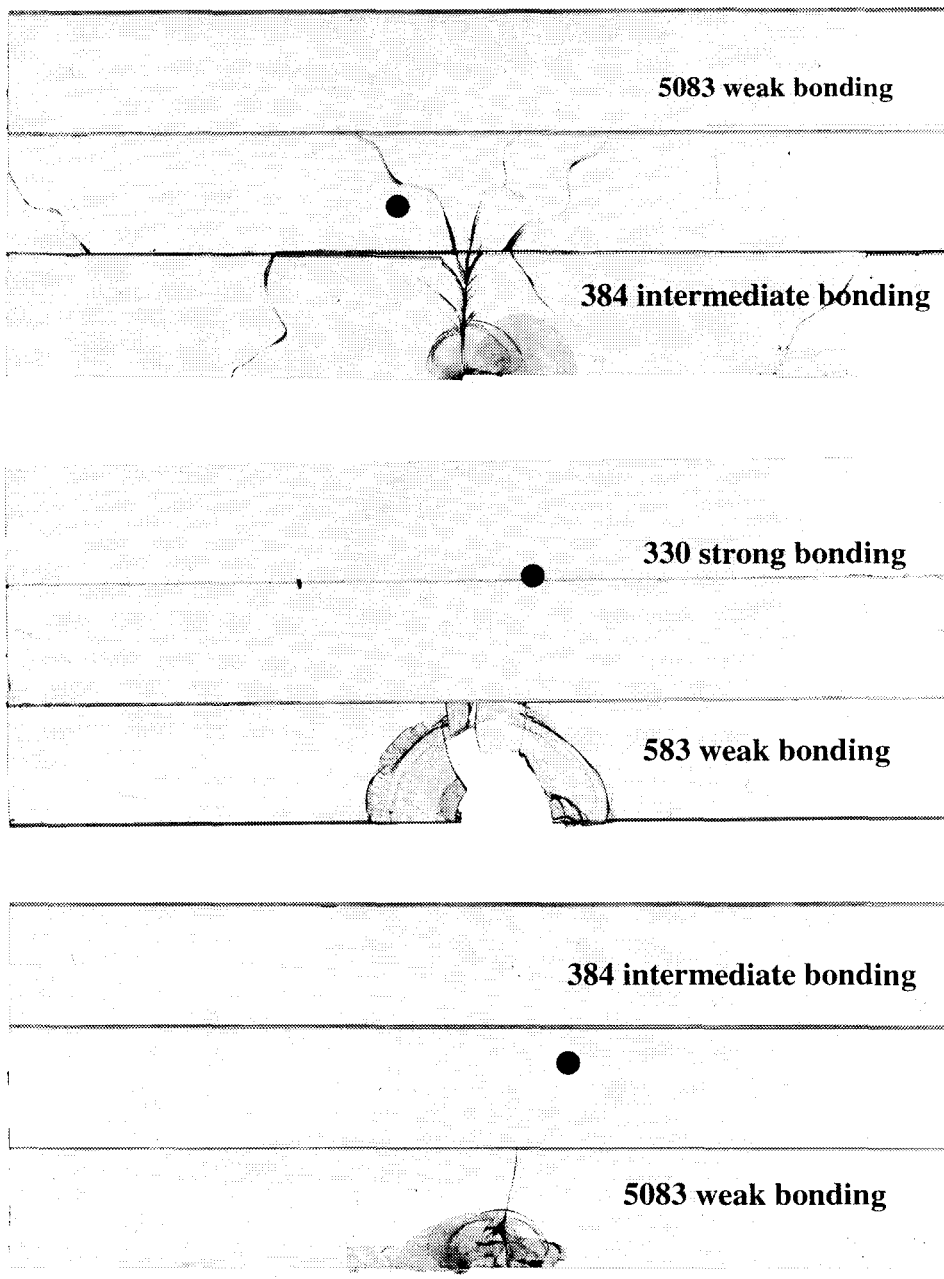

Figure 18. Comparison of final pattern of the three-layer specimens with 5083 bonding with the same impact speed of 21m/s. (a) 3LHHSP384583-3841 (b) 3LHHSP330583-5831 (c) 3LHHSP384583-5831

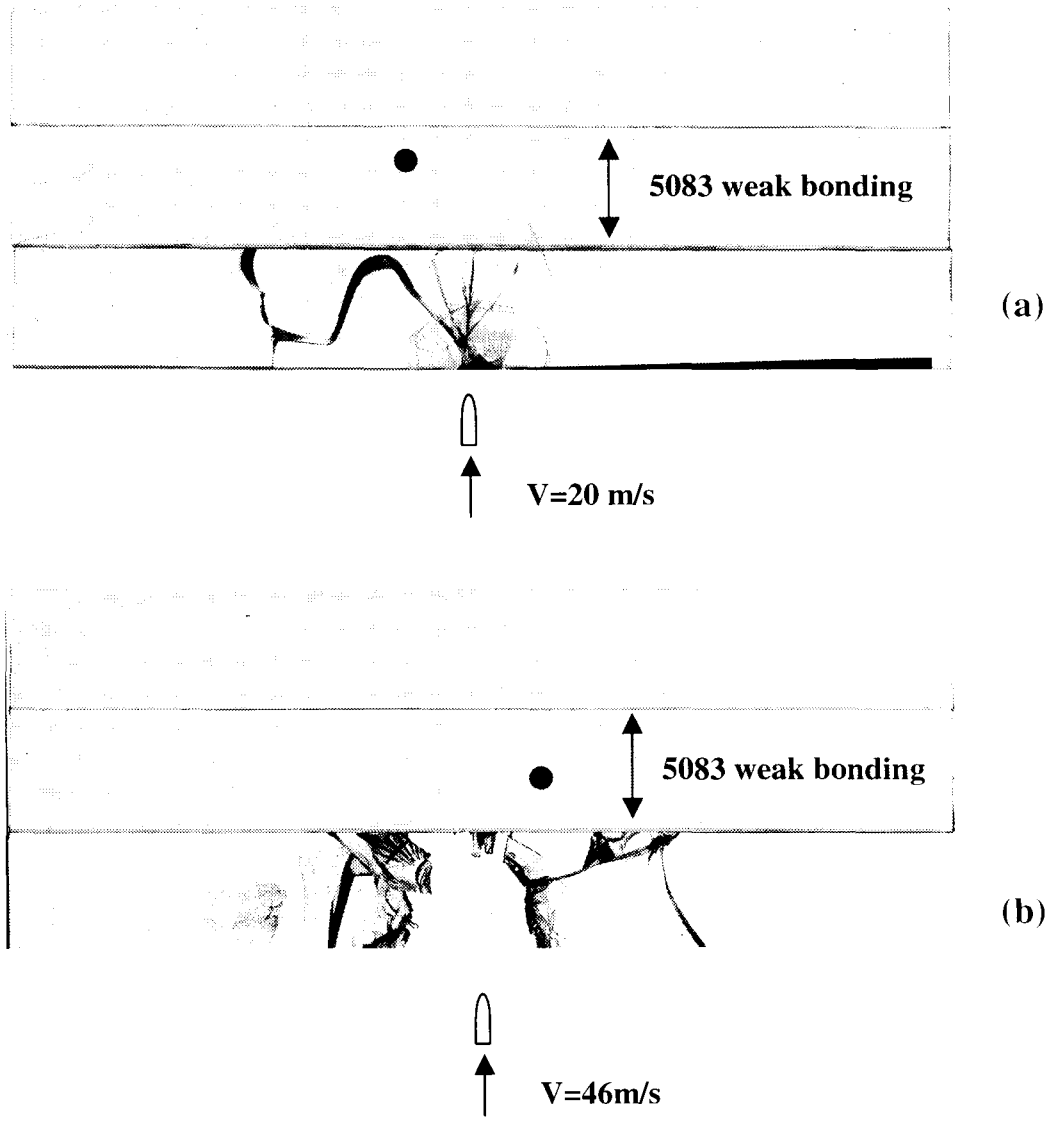

Figure 19. Effect of the impact speed to failure patterns of the three-layer specimens featuring two weak but ductile adhesive bonds.

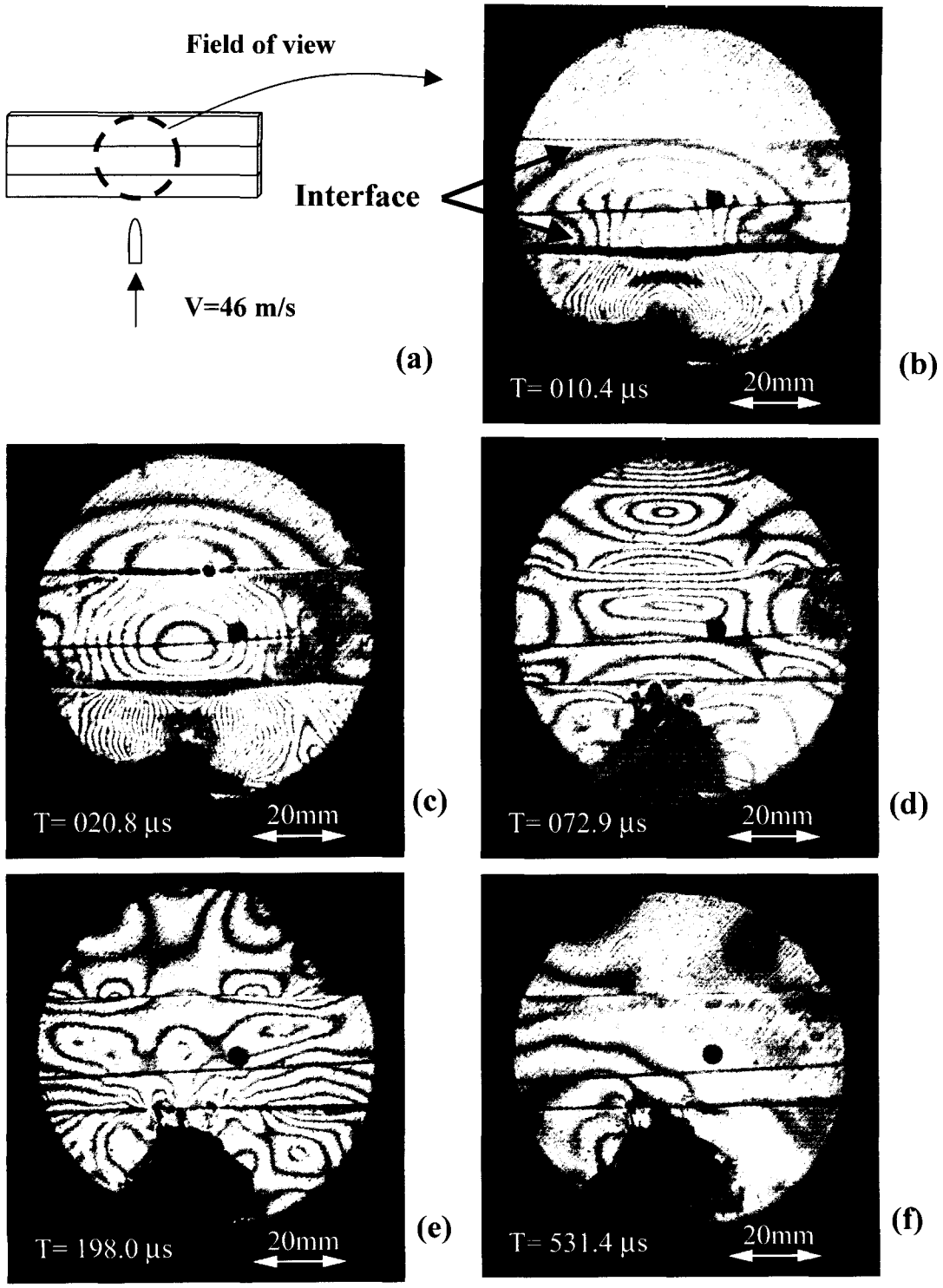

Figure 20. Impact damage progress and wave propagation in a three-layer specimen featuring two 5083 weakly bonded interfaces (3LHHSP583-2).

Chapter IV

Dynamic Crack Deflection and Penetration at Interfaces in Homogeneous Materials: Experimental Studies and Model Predictions

Abstract

We examine the deflection/penetration behavior of dynamic mode-I cracks propagating at various speeds towards inclined weak planes/interfaces of various strengths in otherwise homogenous isotropic plates. A dynamic wedge-loading mechanism is used to control the incoming crack speeds, and high-speed photography and dynamic photoelasticity are used to observe, in real-time, the failure mode transition mechanism at the interfaces. Simple dynamic fracture mechanics concepts used in conjunction with a postulated energy criterion are applied to examine the crack deflection/penetration behavior and, for the case of interfacial deflection, to predict the crack tip speed of the deflected crack. It is found that if the interfacial angle and strength are such as to trap an incident dynamic mode-I crack within the interface, a failure mode transition occurs. This transition is characterized by a distinct, observable and predicted speed jump as well as a dramatic crack speed increase as the crack transitions from a purely mode-I crack to an unstable mixed-mode interfacial crack.

IV-1. Introduction

When cracks propagate in homogenous, brittle solids, they can only do so under locally mode-I conditions and at sub-Rayleigh wave speeds typically below the crack branching speed (Freund, 1990; Broberg, 1999). Indeed, even if the applied far-field loading is asymmetric, the dynamically growing crack will curve and follow the path that will result to locally opening (mode-I) conditions at its tip making mix-mode and pure mode-II crack growth in homogeneous materials a physical impossibility. In addition, as the crack accelerates, under increasing far-field loading, it reaches a critical speed beyond which it becomes energetically more favorable to propagate with multiple, branched crack tips rather than as a single entity. This is called the branching speed which for a material like Homalite-100, is approximately equal to 0. 35 Cs.

The situation is entirely different if a crack is constrained to propagate along a weak preferable path in an otherwise homogenous solid. In this case and depending on the bond strength, the weak crack path or bond often traps the crack, suppresses any tendency of branching or kinking out of the weak plane and permits very fast crack growth much beyond the speeds observable in monolithic solids (Rosakis et al., 1999). Indeed, when mode-I cracks propagate in both isotropic and orthotropic solids containing weak crack paths (Washabough and Knauss, 1994; Coker and Rosakis, 1999), they can reach speeds as high as the Rayleigh wave speed of the solid. On the other hand, when mode-II cracks are made to propagate along such weak cracks, they tend to go even faster with speeds that are clearly within the intersonic regime of the solid (Rosakis et al., 1999; Gao et al., 2000; Geubelle and Kubair, 2001; Coker and Rosakis, 2001).

Although the extreme mode-I and mode-II cases have recently been studied experimentally and theoretically, very little is known about the dynamic mixed-mode crack growth along weak paths, a situation that has only recently been analyzed by Geubelle and Kubair (2001) and about the transition of an incident dynamic mode-I crack into a mixed-mode crack as it encounters a weak plane or interface. In the present work, we examine the incidence of dynamically growing cracks at inclined interfaces of various strengths. Our first goal is to observe this phenomenon experimentally and to establish and validate a dynamic deflection/penetration criterion. We then concentrate on the deflection behavior and examine mixed-mode crack growth along an interface.

It should be noted that stack deflection/penetration behavior at an interface has been the subject of numerous research efforts in the past years and that many significant results for various kinds of materials have been obtained (Cook and Gordon, 1964; He and Hutchinson, 1989a; Gupta et al., 1992; Evans and Zok, 1994; Martinez and Gupta, 1994; Ahn et al., 1998; Leguillon et al., 2000; Qin and Zhang, 2000). For quasi-statically growing cracks, the fracture toughness ratio of the interface and the matrix material has been identified as the most important parameter governing the crack deflection /penetration phenomenon and has formed the basis of a highly successful crack deflection/penetration criterion (Hutchinson and Suo, 1992). To authors' knowledge and with very few notable exceptions (Siegmund et al., 1997), the equivalent dynamic problem has remained unexplored. In this paper we deal only with an important subset of this problem. In particular, we consider weakly bonded systems composed of identical constituents solids so that the resulting material remains constitutively homogenous. However, the existence of a weak bond (bond of lower fracture toughness) makes this

material inhomogeneous regarding its fracture resistance behavior. By doing so we avoid the complication of the material property and wave speed mismatch across the interface while retaining the essential properties of a weak path or bond whose strength can be experimentally varied and analytically modeled.

Motivation for studying this basic problem comes from our recent experimental observations of dynamic failure mechanisms in bonded Homalite layers subjected to projectile impact (Xu and Rosakis, 2001a). A visual example of the interaction of a fan of dynamically moving mode-I branches incident on a weak interface is shown in Figure 1 (Dynamic equivalent of the Cook-Gordon mechanism). The horizontal line in this picture represents an interface between two weakly bonded Homalite layers. As the subsonic mode-I cracks approach the interface, one central shear-dominated interfacial crack is nucleated and propagates along the bond at intersonic speeds providing an illustrative example of failure mode transition. This nucleation and growth of a symmetrically growing intersonic shear crack along a straight-line path is extensively discussed in the book by Broberg (1999). Figure 1 is the direct evidence that such cracks exist and may be nucleated through remote interaction of incoming mode-I cracks with weak interfaces. Another example of the interaction between mode-I crack growth and an interface is given in the post-mortem picture of Figure 2. Here two mode-I branches are incident on to the same vertical interface at approximately the same speed. The two cracks meet the interface at two different incident angles (angle between the crack path and the interface). As evident form the picture, the crack that meets the interface at 78 degrees penetrates the interface while the other one is trapped by it (incident angle is 50 degrees). Another motivation comes from the question of dynamic crack propagation in brittle

heterogeneous solids (composed of large grains bonded together by weak grain boundaries). Examples of such solids include marble (Rosakis, 2000) or certain classes of high explosives (Dienes, 1996). Figure 3 shows a dynamic crack propagating towards a grain boundary which it may penetrate or follow depending on the incident crack speed, incident crack angle as well as the relative toughnesses between the grain and the grain boundary.

IV-2. Experimental procedures

IV-2.1 Materials and specimens

Similar to previous dynamic experiments (Rosakis et al., 1998), Homalite-100 was selected as our model photoelastic materials. Within the range of possible photoelastic materials, Homalite-100 was chosen because its dynamic facture behavior has been documented widely in the literature. Indeed the variation of dynamic fracture toughness of monolithic Homalite with crack speed has been studied in the early years of the dynamic fracture discipline (Dally, 1979; Fourney et al., 1983; Kalthoff, 1983). These results are used in relation to the analytical model described in section 4. Some of the physical properties of Homalite-100 are listed in Table 1. The quasi-static values were obtained from the literature while the dynamic values were measured by the authors (Xu and Rosakis, 2001a).

A novel wedge-loaded plate specimen was designed to produce a single, straight dynamic crack propagating towards the weakly bonded, inclined interface as shown in Figure 4. The wedge is inserted into a pre-notch and when it is impacted by a projectile, the wedge opens the notch faces producing a single mode-I crack which is driven towards

the inclined interface. The initial crack tip speed is related to the impact speed of the projectile. The advantage of this type of dynamic loading is the generation of a negative T-stress which enhances crack path stability and retards branching as the crack tip speed reaches certain levels (Cotterell and Rice, 1980). Wedge-loaded specimens of various types have been used extensively in previous static and dynamic fracture experiments (Hahn et al., 1980; Thouless, 1992; Guduru et al., 2001).

The specimen's sizes were large enough such that the major stress waves reflected from free boundaries entered the field of view, 20 μs after the incident crack reached the interface. After numerous preliminary tests, the in-plane specimen size was fixed to be 457 mm long, 254 mm wide and the plate thickness was 9.5 mm. Inclined interfaces were cut and covered several characteristic interfacial angles. These angles were 10, 30, 45, 60 and 90 degrees. To provide different interfacial strengths and fracture toughnesses, two kinds of adhesives, Weldon-10 and Loctite 384, were used to bond the interfaces and to create weak interfaces of toughness less than that of monolithic Homalite. The interfacial bond strengths and the fracture toughnesses were measured by the authors and are listed in Table 2 (Xu and Rosakis, 2001b). The Weldon-10 adhesive is considered to be a "strong" adhesive. The Loctite 384 formed a "weak" bond. The average thickness of all adhesive layers was less than 20 μm.

IV-2.2 Experimental setup

A schematic of the dynamic photoelasticity setup used in this study is given in Figure 5. Two sheets of circular polarizer were placed on either side of the specimen. The coherent, monochromatic, plane polarized laser output is collimated to a beam of 100 mm

in diameter. The laser beam is transmitted through the specimen. The resulting fringe pattern is recorded by the high-speed camera. A Cordin model 330A rotating mirror type high-speed film camera is used to record the images. During the impact test, a projectile was fired by the gas gun and impacted the loading wedge to trigger the recording system and to dynamically initiate the mode-I incident crack. Details of experiments were reported by Xu and Rosakis (2001a). Under the dynamic deformation, the generation of isochromatic fringe patterns is governed by the stress optic law. For the case of monochromatic light, the isochromatic fringe patterns observed are proportional to contours of constant maximum in-plane shear stress, $\hat{\tau}_{\max} = (\hat{\sigma}_1 - \hat{\sigma}_2)/2$.

IV-3. Experimental observations

In order to systematically study effects of interfacial angles, bond strengths and impact speeds on the dynamic crack penetration/deflection behavior at interfaces, a baseline impact speed of 19-20 m/s was chosen in order to produce a single mode-I crack without inducing crack branching at the pre-notch. Then, for the same interfacial bonding, different interfacial angles were tested.

IV-3.1 Crack deflection/penetration at a weak interface

Figure 6 shows a series of dynamic photoelasticity images of the crack deflection process at a weak interface whose interfacial angle is 10 degrees. The impact speed was 27 m/s. The vertical line appearing in every image is the camera streak line, which is used for positioning and reference purposes. Another almost horizontal thin line reveals the position of the interface. The dark circular spot, at the center and just above the interface,

is a scaling mark of 6.35 mm in diameter. Around 8 μs after impact, fringe patterns associated with the stress wave loading, induced by projectile impact, are clearly seen at the notch tip (Figure 6 (b)). Generally, the whole recording system has a delay and a timing error of 10 μs. In Figure 6 (c), a mode-I crack is seen propagating towards the inclined interface at high speed. The incident mode-I crack reached the interface at around 110 μs after impact. Then it transitions into a mixed-mode interfacial crack as seen in Figures 6 (e) and (f). The small asymmetry in the fringe patterns of the interfacial crack reveals the existence of a small mode mixity. The crack length versus time record is shown in Figure 7. The noticeable change of slops at around 120 μs indicates a significant increase of the cracks tip speed after the crack deflection. The average speed of the incoming crack is approximately 407 m/s. After crack defection at the interface, the average interfacial crack speed is approximately 988 m/s.

In the experiment described above, an impact speed of 27 m/s was employed and strong fringe patterns during the crack deflection process were observed. In the next experiment, a relatively lower impact of 19-20 m/s was intentionally chosen to reduce the spurious stress waves caused by projectile impact. Figure 8 shows the crack deflection process at a weak interface whose interfacial angle is 30 degrees. In Figure 8 (b), a dynamically propagating mode-I crack (surrounded by symmetric fringe patterns) is seen to propagate towards the interface. Around 164 μs after impact, we notice that the crack tip fringe pattern has already started to lose some of its symmetry. Around 170 μs (Figure 6 (d)), this mode-I incident crack has already transited into a mixed-mode crack at the interface whose fringe pattern at the crack tip was clearly asymmetric with respect to its propagation direction. In fact, a close look at this pattern reveals that its line of symmetry

is still parallel to the horizontal line although the crack propagates along the inclined weak interface. Also, the caustic (or shadow spot surrounding the crack tip) size at the crack tip was significantly reduced in comparison to the caustic sizes in Figures 8 (b) and (c). As the interfacial crack quickly moved out of the field of view, the horizontal crack faces of the original mode-I crack are seen to experience clear frictional contact as evident from the Figure 8 (f).

The abruptness of the transition behavior between a mode-I incident crack and a mixed-mode interfacial crack can be graphically witnessed by the impressive jump in crack speed across the interface. Figure 9 (a) shows the total crack length history as the incident mode-I crack develops and transitions into a mixed-mode interfacial crack. The interfacial crack length used in Figure 9 (a) is defined as the total instantaneous ark length measured along the no-uniform crack path. Differentiation of the crack length record furnishes the tangential crack tip speed before and after crack deflection. Since the differentiation process is based on a three-point-fitting of the crack length history, the exact crack speed at the interface could not be obtained. Before deflection, the crack tip speed is approximately 400 m/s, which is a speed very close to the branching speed of Homalite-100. After crack deflection, the speed jumped by as much as 800-1000 m/s and then decreased as it propagated further along the interface.

The next experiment was conducted at an interfacial angle of 45 degrees. The incident crack reached the interface around 150 μs after impact as seen in Figure 10 (c). It is observed that the symmetric fringe pattern disappeared as soon as the crack deflected into the interface (see Figures 10 (c) and (d)). The shape of the fringe pattern of Figure 10 (e) suggests that this interfacial crack is shear-dominated at the latter propagation stage. It

is interesting to observe that after this shear-dominated crack propagated some distance along the interface, some secondary cracks formed at one side of the interface. These secondary cracks are locally mode-I and form on the tension side of the sheared bimaterial interface. They form after the dominant crack has propagated along the interface and thus after the interface has already failed in shear. These types of secondary cracks that are a by-product of shear crack growth along interfaces have already been observed experimentally (Rosakis, et al., 2000; Xu and Rosakis, 2001a) and are always associated with dynamic shear-dominated crack growth along weak interfaces. Figure 11 presents the crack length and crack speed history. Similar to previous cases, a significant slope change of the crack length versus time record across the interface is seen in Figure 11 (a). This is verified by the crack speed jump which is obvious in Figure 11 (b) and is clearly due to the transition of the mode-I incident crack to a mixed-mode interfacial crack.

As the interfacial angle is changed to 60 degrees, the dynamic crack deflection behavior is slightly altered. As shown in Figure 12, the incident mode-I crack approached the interface at about 150 μs after impact and transitioned into a mixed-mode interfacial crack. At around 177 μs, this mixed-mode interfacial crack kinked into the right side of the interface. A significant caustic (or shadow spot) is seen in Figure 12 (e) to show the mode-I nature of the kinked crack. The speed of the kinked crack, which moved into the homogeneous Homalite part, was high enough to induce multiple branches which are visible in Figure 12 (f). The whole process is reflected in the crack speed record which is shown in Figure 13. First, we notice the crack speed jump across the interface at about 150 μs. Obviously, the initial interfacial crack speed of 700 m/s is much higher than the

incident crack speed which is about 400 m/s. However, the interfacial crack speed reduced to 350 m/s soon after the interfacial crack kinked into the right side of monolithic Homalite. The experiment also suggests that just before the crack kinking, there was a brief crack speed reduction characteristically seen in several failure mode transition experiments (Xu and Rosakis, 2001c).

The above results clearly elucidate the role of interface inclination on the nature of failure mode transition. In the following section, we will concentrate on the role of the interfacial strength on the same phenomenon. We also expect that interfacial bond strengths are essential to the determination of the dynamic crack deflection/penetration behavior (Needleman and Rosakis, 1999).

IV-3.2 Crack deflection/penetration at a strong interface

In the set of experiments described in this section, we examine interfaces inclined at exactly the same angles as in section 3.1 and incident mode-I cracks propagating with speeds that are nominally the same as before. The only difference is in the interfacial bond strength, which is higher than in the previous case.

Figure 14 shows a series of photoelasticity snap shots following impact of a specimen featuring a strong interfacial bond and an interfacial angle of 10 degrees. Figure 14 (b) shows a dynamically propagating mode-I crack (symmetric fringe patterns) approaching the interface at approximately 113 μs after impact. Around 133 μs after impact, the mode-I incident crack has just reached the interface as shown in Figure 14 (c). We notice that, at this moment, the crack tip fringes still had a symmetric pattern. At 150 μs, this mode-I crack transitioned into a mixed-mode crack at the interface in a

manner very similar to the case described in the previous section (See Figure 6 (d)). The transition behavior between the mode-I incident crack and the mixed-mode interfacial crack is clearly evident in the crack length and the crack speed records (see Figure 15 (a)). The instantaneous jump in crack tip speed is again evident.

Figure 16 shows the dynamic crack deflection at a strong interface whose interfacial angle is 30 degrees. Around 150 μs after impact, the incident crack approached the interface. Later on, it induced an deflected interfacial crack which propagated along the interface only. The crack length and speed records are shown in Figure 17 and they are qualitatively similar to the previous cases. The amplitude of the crack speed jump is approximately 550 m/s as opposed to 150 m/s of the previous case.

The last case considered in this section (see Figure 18) is the one involving an interfacial angle of 60 degrees. In this case, the interfacial crack kinked only slightly off its original path and then accelerated again in to the right side of the interface reaching branching conditions at 235 μs after impact. (See Figure 18 (f).) The experiment suggests that for this "strong" interface, the interfacial angle of 60 degrees is very close to the critical angle above which a crack penetration of this interface is possible. Figure 18 should be compared to Figure 12 where a weaker interface (also at 60 degrees) was tested under nominally the same conditions. The differences between the deflection/penetration behavior of Figure 12 (f) and 18 (f) are evident.

IV-4. A model for dynamic crack deflection/penetration

Figure 19 shows a schematic diagram describing the geometry relevant to the dynamic crack deflection/kinking problem. Two identical homogeneous and isotropic

elastic solids are bonded along an interface indicated here by the dashed line. The Young's and shear moduli, Poisson's ratio and mass density are denoted by E, μ, υ and ρ respectively. Before reaching the interface, a dynamic mode-I crack propagates within the homogenous solid towards the inclined interface (Figure 19 (a)). The angle between the crack plane and the interface is denoted by β. The critical question to be addressed is whether this mode-I crack will continue to propagate on the original crack plane (x_2=0) after encountering the interface (Figure 19 (a)), or it will kink out to propagate along the interface and become a mixed-mode interfacial crack (Figure 19 (b)). It is anticipated that the former (continuous crack propagation along the original crack plane) and the latter (crack deflection) modes occur for strong and weak interfaces, respectively.

IV-4.1 Static crack kinking/deflection analysis

He and Hutchinson (1989a,b) studied the competition between the two fracture modes of continuous crack propagation on the crack plane and crack kinking along a bimaterial interface subjected to remote static loading. An extensive discussion of this phenomenon was described by Hutchinson and Suo (1992). Once the two constituents have identical elastic properties (as in the present constitutively homogenous material system), the analysis becomes very simple, as described in the following.

For a mode-I crack subjected to a remote static stress intensity factor, K_I^s, continuous crack propagation within the crack plane occurs when the mode-I static crack energy release rate, G_I^s, reaches the fracture toughness Γ_{IC}^{MA} of the matrix material, i. e.,

$$G_I^s = \frac{1-\upsilon^2}{E}\left(K_I^s\right)^2 = \Gamma_{IC}^{MA} \qquad (1)$$

On the other hand, the crack will deflect/kink at the interface when the static energy release rate of the kinked/deflected crack tip, G^{sk}, reaches or exceeds the fracture toughness of the interface, Γ_c^{IT}, i.e.,

$$G^{sk} = \frac{1-\upsilon^2}{E}\left[(K_I^{sk})^2 + (K_{II}^{sk})^2\right] = \Gamma_c^{IT} \tag{2}$$

where K_I^{sk}, K_{II}^{sk} are static mode-I and mode-II stress intensity factors for the deflected (kinked) mixed-mode crack, and they are related to the remote mode-I stress intensity factors before crack deflection at the interfaces as a function of the kinking angle β (interfacial angle) (Hutchinson and Suo, 1992; Anderson, 1995):

$$K_I^{sk} = K_I^s\left(\frac{3}{4}\cos\frac{\beta}{2} + \frac{1}{4}\cos\frac{3\beta}{2}\right)$$
$$K_{II}^{sk} = K_I^s\left(\frac{1}{4}\sin\frac{\beta}{2} + \frac{1}{4}\sin\frac{3\beta}{2}\right) \tag{3}$$

From the ratio of equations (2) and (1), the critical conditions governing these two fracture modes are as follows:

$$\frac{G^{sk}}{G_I^s} < \frac{\Gamma_c^{IT}}{\Gamma_{Ic}^{MA}} \tag{4a}$$

for the continuous crack propagation (crack penetration) along the original crack plane and

$$\frac{G^{sk}}{G_I^s} \geq \frac{\Gamma_c^{IT}}{\Gamma_{Ic}^{MA}} \tag{4b}$$

for crack deflection/kinking at the interface. It is observed that from equations (1)-(3), the ratio of two energy release rates depends only on the kinking (interfacial) angle and not on the value of the stress intensity factor or material properties.

$$\frac{G^{sk}}{G_I^s} = \frac{1}{16}\left[(3\cos\frac{\beta}{2} + \cos\frac{3\beta}{2})^2 + (\sin\frac{\beta}{2} + \sin\frac{3\beta}{2})^2\right] \tag{5}$$

It is pointed out that the above expression for the energy release rate ratio holds for both plane strain and plane stress analyses.

IV-4.2 Dynamic crack propagation in the crack plane

Let v_1 denote the crack tip speed prior to reaching the interface. The dynamic energy release rate around the mode-I, plane strain crack tip is given by (e.g., Freund, 1990; Broberg, 1999)

$$G_I^d = \frac{1-\upsilon^2}{E}\left[A_I(v_1)(K_I^d(v_1))^2\right] \tag{6}$$

where K_I^d is the dynamic stress intensity factor of the incident mode-I crack. A_I is a universal function of crack tip speed v_1, given by

$$A_I(v) = \frac{v^2\alpha_d}{(1-\upsilon)c_s^2 D} \tag{7}$$

where

$$D = 4\alpha_s\alpha_d - (1+\alpha_s^2)^2$$

$$\alpha_s = \sqrt{1-(v/c_s)^2} \qquad \alpha_d = \sqrt{1-(v/c_d)^2} \tag{8}$$

$$c_s = \sqrt{\frac{\mu}{\rho}} \qquad c_d = \sqrt{\frac{\kappa+1}{\kappa-1}}c_s$$

$$\kappa = \begin{cases} = 3-4\upsilon & (plane \quad strain) \\ = \dfrac{3-\upsilon}{1+\upsilon} & (plane \quad stress) \end{cases}$$

and Cs and Cd are the shear wave speed and dilatational wave speeds of the matrix material. Under certain circumstances, the dynamic crack stress intensity factor K_I^d can be related to its static counterpart K_I^s through a "universal function of crack tip speed," $k_I(v)$ (Freund, 1990)

$$K_I^d = k_I(v_1)K_I^s \tag{9}$$

where the universal function of crack tip speed depends on the material properties through the elastic wave speeds, but it is independent of the loading on the body:

$$k_I(v) = \frac{1-v/c_R}{S_t(1/v)\sqrt{1-v/c_d}} \tag{10}$$

where C_R is the Rayleigh wave speed of the material. For most practical purposes, $S_t(1/v) \approx 1$. The crack will continue to propagate in the crack plane if the dynamic energy release rate of the mode-I incident crack reaches the corresponding dynamic fracture toughness $\Gamma_{Id}^{MA}(v_1)$ of the matrix materials, i.e.,

$$G_I^d = \frac{1-\nu^2}{E} A_I(v_1)\left[k_I(v_1)K_I^s\right]^2 = \Gamma_{Id}^{MA}(v_1) \tag{11}$$

where equations (6) and (9) have been used.

IV-4.3 Dynamic crack deflection/kinking along the interface

As shown in Figure 19 (b), let v_2 denote the speed of the deflected crack tip at the instant right after deflection, and let K_I^{dk}, K_{II}^{dk} be dynamic mode-I and mode-II stress intensity factors for the deflected (kinked) mixed-mode crack. We will assume that the universal relation (equation 9) between the dynamic and static stress intensity factors also holds for the deflected crack tip, i.e.,

$$K_I^{dk} = k_I(v_2)K_I^{sk} \tag{12}$$

$$K_{II}^{dk} = k_{II}(v_2)K_{II}^{sk}$$

where the static stress intensity factors around the deflected crack tip are given in equation (3). In the above, k_I is the same universal function in equation 10 for mode-I dynamic crack propagation (though it is a function of the speed of the deflected crack), k_{II} is the universal function for mode-II dynamic crack propagation and is the same as k_I in equation 10 except that the dilatational wave speed C_d is replaced by the shear wave speed Cs (Freund, 1990), i.e.,

$$k_{II}(v) \cong \frac{1-v/c_R}{\sqrt{1-v/c_s}} \tag{13}$$

The dynamic energy release rate around the deflected crack tip is then related to the corresponding dynamic crack tip stress intensity factors by

$$G^d = \frac{1-\upsilon^2}{E}\left[A_I(v_2)[K_I^{dk}]^2 + A_{II}(v_2)[K_{II}^{dk}]^2\right] \tag{14}$$

where A_{II} is given by (e.g., Freund, 1990)

$$A_{II}(v) = \frac{v^2\alpha_s}{(1-\upsilon)c_s^2 D(v)} \tag{15}$$

The crack will deflect at the interface if the dynamic energy release rate around the deflected crack tip reaches or exceeds the corresponding fracture toughness of the interface, i.e.,

$$G^d = \frac{1-\upsilon^2}{E}\left[A_I(v_2)[k_I(v_2)K_I^{sk}]^2 + A_{II}(v_2)[k_{II}(v_2)K_{II}^{sk}]^2\right] \geq \Gamma_c^{IT}(v_2) \tag{16}$$

IV-4.4 Critical condition for dynamic crack deflection at the interface

Similar to the static case, we may use the ratio of dynamic crack energy release rates in equations (11) and (16) to determine the critical condition for dynamic crack deflection at the interface. The advantage of using the ratio of equations (16) to (11) is that the remote stress intensity does not come into play and as a result the resulting criterion for dynamic crack deflection depends only on the interfacial angle β, the crack tip speeds v_1 and v_2, and the shear and longitudinal wave speeds Cs and Cd. Using equations (7) and (1) for A_I and A_{II} respectively and the relation (3) between the static stress intensity factors, we have determined the ratio of two energy release rates for the deflected (kinked) interfacial crack and the incident mode-I crack:

$$\frac{G^d(\beta,v_2)}{G_I^d(v_1)}=\frac{A_I(v_2)k_I^2(v_2)(3\cos\frac{\beta}{2}+\cos\frac{3\beta}{2})^2+A_{II}(v_2)k_{II}^2(v_2)(\sin\frac{\beta}{2}+\sin\frac{3\beta}{2})^2}{16A_I(v_1)k_I^2(v_1)}$$

$$=\left(\frac{v_2}{v_1}\right)^2\frac{D_1}{D_2}\frac{\alpha_{d2}k_I^2(v_2)(3\cos\frac{\beta}{2}+\cos\frac{3\beta}{2})^2+\alpha_{s2}k_{II}^2(v_2)(\sin\frac{\beta}{2}+\sin\frac{3\beta}{2})^2}{16\alpha_{d1}k_I^2(v_1)} \qquad (17)$$

It should be pointed out that, similar to its counterpart (5) for the static case, the above ratio holds for both plane strain and plane stress analyses. From equations (16) and (11), the crack deflection criterion can be stated as follows:

$$\frac{G^d(\beta,v_2)}{G_I^d(v_1)}\geq\frac{\Gamma_c^{IT}(v_2)}{\Gamma_{Id}^{MA}(v_1)} \qquad (18)$$

It should be noted at this point that, for fixed β and v_1, the ratio in the left side of equation (18) vanishes for $v_2=C_R$ and is maximized for $v_2=0$. This is evident from Figure 20 where this ratio is plotted as a function of v_2 for various interfacial angles β. Simple inspection of equation (17) shows that this behavior is a consequence of the speed dependence of universal functions $k_I(v)$ and $k_{II}(v)$ which vanish at $v=C_R$. The behavior of this ratio necessitates that the above deflection criterion is reduced to

$$Max_{v_2}\{\frac{G^d(\beta,v_2)}{G_I^d(v_1)}\}=\frac{G^d(\beta,0)}{G_I^d(v_1)}\geq\frac{\Gamma_c^{IT}(v_2)}{\Gamma_{Id}^{MA}(v_1)} \qquad (19)$$

If the criterion is indeed satisfied and the crack deflects into the interface, its speed v_2 will be such that relation (18) holds as a pure equality. Then

$$\frac{G^d(\beta,v_2)}{G_I^d(v_1)}=\frac{\Gamma_c^{IT}(v_2)}{\Gamma_{Id}^{MA}(v_1)} \qquad (20)$$

and the above equation will provide an expression for v_2, as a function of the incident crack tip speed v_1, and the ratio of interfacial to matrix toughnesses (right-hand side of equation 20). The toughness ratio will itself, in general, be a function of the crack tip speeds v_1 and v_2. Indeed, $\Gamma_{Id}^{MA}(v_1)$ is the dynamic fracture toughness of the matrix material (Homalite-100 in this experiment), which is a function of crack speeds that has been measured in experiments by Kobayashi and Mall (1978) and Dally (1979). In nominally brittle homogenous materials such as Homalite-100, PMMA and Glass, the functional form $\Gamma_{Id}^{MA}(v_1)$ is typically monotonically increasing from a quasi-static crack growth value to much larger levels achieved just before the branching speed is reached (Rosakis and Ravichandran, 2000). Indeed, as a crack increases its speed, it starts generating local micro-kinks, or abortive branches, whose number drastically multiplies just before final branching occurs. By doing so, the total energy spent in crack growth (toughness) increases drastically (Ravi-chandar and Knauss, 1984; Sharon and Finenberg, 1999), accounting for the observed drastic increase of toughness with speeds close to 0.3-0.4 Cs. In the presence of weak paths, bonds or interfaces, the situation is often very different. The weak path suppresses any off-plane microbranches that might develop as a mode-I crack accelerates along its length (Lee and Knauss, 1989; Washabaugh and Knauss, 1994). This effect deactivates the mechanism of fracture toughness increase with speeds, described above for purely homogeneous monolithic solids, and allows a crack to reach speeds as high as the Rayleigh wave speed of the surrounding bulk solids without any increase in fracture toughness (Washabaugh and Knauss, 1994; Coker and Rosakis, 2001). Weak fracture paths and bonds can also trap mixed-mode or mode-II propagating cracks. Indeed depending on the detailed bond characteristics, mixed-mode cracks can

often become very fast and may (unlike their mode-I equivalent) become intersonic as shown in a series of recent studies (Lambors and Rosakis, 1994; Rosakis et al., 1999; Coker and Rosakis, 2001). Consistent with the above discussion, we will assume in this work that the interfacial fracture toughness is independent of the crack speed and of the mode mixity. We believe this second assumption to be a good assumption for most mixity levels especially because the materials to the right and left of the bonds are identical (Hutchinson and Suo, 1992). Following these assumptions, equation (20) which determines the interfacial crack tip speed v_2 as a function of the speed v_1 of the incident mode-I crack is

$$\frac{G^d(\beta, v_2)}{G_I^d(v_1)} = \frac{\Gamma_c^{IT}}{\Gamma_{Id}^{MA}(v_1)} \tag{21}$$

IV-5. Results and discussions

IV-5.1 Deflection vs. penetration

To determine whether an incident crack will penetrate an interface, the normalized energy release rate, which is the left-hand side of equation (19), is plotted as a function of angle β, at the particular speed of incidence v_1. Examples of such plots are seen in Figures 21 and 22. The right-hand side of this equation is then estimated from experimental measurements of the fracture toughness of the bond and the bulk Homalite at crack growth speed v_1. The data for the variation of dynamic fracture toughness with speeds were reported by Fourney et al. (1983), Kalthoff (1983), Kobayashi and Mall (1978).

We first start by applying this methodology to the experiments briefly discussed in Figure 2 (Xu and Rosakis, 2001a). In this case, the bond involved in a polyester adhesive and its fracture toughness is 0.56 MPa $\sqrt{m}$ (Xu and Rosakis, 2001a). The incident crack speed was about 300 m/s. The fracture toughness of Homalite at this crack speed is 0.6 MPa $\sqrt{m}$, making the ratio $\Gamma_c^{IT} / \Gamma_{Id}^{MA}$ in the right-hand side of equation (19) equal to 0.87. Figure 21 displays a graphic representation of the inequality (19). Indeed, according to the criterion, deflection into the interface will take place at $0<\beta< 59^{o}$ while the interface will be penetrated for $59^{o}<\beta< 90^{o}$. It should be noted here that both cases displayed in Figure 2 are consistent with this prediction.

For the inclined interface experiments presented here in Chapter 3, the incident crack speed varied between 350 to 450 m/s (0.252-0.377 Cs) and the corresponding dynamic fracture toughness of Homalite-100 varied from 0.75 to 1.4 MPa respectively. Recognizing a certain level of uncertainty in the experimental measurement of crack tip speeds and toughness (both bond and Homalite), average values of these parameters were taken.

Figure 22 (a) and (b) describe the predicted crack deflection/penetration regimes for the two types of bonds described in Table 2 and used in the experiments presented in section 3. It should be noted here that for the case of a weak bond (Loctite-384 adhesive), there is no intersection of the horizontal line (toughness ratio) with the left-hand side of equation (19) at speeds v_1 such that $0.252 < v_1 < 0.377$ Cs. This means that the crack will always deflect into the interface as is the case in Figures 6, 8, 10 and 12. For a higher bond strength case (Weldon-10 adhesive), the crack will deflect into the interface for all $\beta< 68^{o}$ and will penetrate the interface for all $68^{o}<\beta< 90^{o}$. This is consistent with the

result of Figures 14, 16 and 18. Indeed, for interface angles 10 and 30 degrees, the crack is clearly deflected. On the other hand for interfacial angle of 60 degrees (see Figure 18), the crack kinked slightly but very soon penetrated the interface suffering only a small temporary deflection. This is consistent with the fact that, within experimental error, 60° is very close to the end of crack deflection zone. It should be noted at this point that the horizontal levels of toughness ratio are represented in Figure 22 as bands to reflect maximum uncertainties in incident crack tip speeds v_1.

IV-5.2 Predictions of the interfacial crack speeds

For a certain speed of the incident mode-I crack and if the interfacial angle and the bond strength are such that the criterion of equation (19) predicts crack deflection at the interface, then the interfacial crack speed can be predicted by equation (20). This procedure is graphically illustrated in Figure 23 (a). This Figure shows the variation of the normalized energy release as a function of interfacial angle for a fixed incident crack speed v_1=0.4 Cs. This ratio depends on v_2 parametrically. The figure also displays the normalized material resistance level for this specific v_1 as a dotted line. For the specific interfacial angle under consideration, a vertical line is drawn to interest the dotted line at a point A. The speed v_2=k v_1 is then adjusted in such a way as to have the normalized energy release curve pass through point A thus satisfying the criterion of equation (20). For reference, the curve corresponding to v_2=0 is also shown. Applying this procedure to the two interface cases discussed in section 3, we can display the variation of the ratio v_2/v_1 as a function of interfacial angle (see Figure 23 (b)). As expected, the weak interface features higher deflection speeds. Also as the interfacial angle increases, the

speed ratio drops in both cases. In particular, for the strong interface case, it drops to zero at an interfacial angle of $\beta=68^{o}$ beyond which penetration will occur. Table 3 compares these analytical predictions to the observations of interfacial crack tip speeds observed in the experiments described in section 3. Given the errors in accurate speed estimation just before and after deflection (about $\pm$ 100 m/s), the agreement is very good.

IV-5.3 Alternative mechanisms of failure mode transition at interfaces

In all cases described above, the incident mode-I crack reached the interface, and within our observation resolution, deflected along it or penetrated through it without nucleating interfacial decohesion at a distance. In Figure 24, we show an alternative way of producing failure mode transition which does not fit within our previous discussions but has conceptual similarities. Here a faster incident crack (crack speed is about 450 m/s) races towards a weak interface (Loctite 384 bond) inclined at an angle of 30 degrees to the horizontal. Before the mode-I crack reached the interface (Figure 24 (c)), a central debonding nucleated at the weak interface and started to propagate downwards first and then upwards along the interface. The two crack tips of this debonding clearly had two different speeds as evident from Figures 24 (e) and (f). This phenomenon was observed mainly for specimens featuring weak interfaces and high incident crack speeds (or high stress intensity factor of the incident crack tip) in some of our experiments. It is very reminiscent of the observations displayed in Figure 1 and discussed in connection to the dynamic "Cook-Gordon mechanism." The static equivalent of this phenomenon was recently analyzed by Arata et al., (2000) and Leguillon et al., (2000) and merits additional attention in the future.

Acknowledgements

The authors gratefully acknowledge the support of the Office of Naval Research (Dr. Y. D. S. Rajapakse, Project Monitor) through a grant (#N00014-95-1-0453) to Caltech. Valuable discussions with Drs. G. Ravichandran, O. Samudrala and G. Xu are appreciated.

References

Anderson, T. L., 1995. Fracture Mechanics 2nd ed., CRC Press, Boca Raton

Arata, J. J. M., Nedleman, A., Kumar, K. S. and Curtin, W. A. 2000. Microcrack nucleation and growth in elastic lamellar solids. International Journal of Fracture, 105, 321-342.

Ahn, B. K., Curtin, W. A., Parthasarathy, T. A. and Dutton, R. E. 1998. Criteria for crack deflection/penetration for fiber-reinforced ceramic matrix composites. Composites Sci. and Technology, 58,1775-1784.

Broberg, K. B., 1999. Cracks and Fracture, Academic Press, San Diego.

Coker, D. and Rosakis, A. J., 2001. Dynamic fracture of unidirectional composite materials: mode-I crack initiation and propagation. In preparation.

Cook, J. and Gordon, J. E. 1964. A mechanism for the control of crack propagation in all brittle systems. Proc. Roy. Soc. 282A, 508-520.

Cotterell, B. and Rice, J. R. 1980. Slightly curved or kinked cracks. International J. of Fracture, 16 (2), 155-169.

Dally, J. W. 1979. Dynamic Photoelastic Studies of Fracture. Experimental Mechanics,19, 349-61.

Dienes, J. K. 1996. A unified theory of flow, hot spots, and fragmentation with an application to explosive sensitivity. In: Davison, L. (Ed.), High pressure shock compression of solids—I. Springer –Verlag, New York.

Evans, A. G. and Zok, F. W. 1994. Review the physics and mechanics of fiber-reinforced brittle matrix composites, J. of Materials Science, 29, 3857-3896.

Fourney, W. L., Chona, R., Sanford, R. J. 1983. Dynamic crack growth in polymers. Workshop on dynamic fracture, W. G. Knauss, K. Ravi-Chandar, A. J. Rosakis ed., Pasadena. Caltech SM Report 83-12. pp.75-99.

Freund, L. B. 1990. Dynamic Fracture Mechanics, Cambridge University Press, New York.

Gao, H., Huang, Y., Gumbsch, P. and Rosakis, A. J. 1999. On radiation-free transonicmotion of cracks and dislocations. Journal of the Mechanics and Physics of Solids. 47, 1941-1961.

Geubelle, P. H. and Kubair, D. 2001. Intersonic Crack Propagation in Homogeneous Media under Shear-dominated Loading: Numerical Analysis. J. Mech. Physics Solids, 49, 571-587.

Guduru, P., Zehnder, A.T., Rosakis, A.J. and Ravichandran, G. 2001. Dynamic, Full-Field Measurements of Crack Tip Temperatures. Engineering Fracture Mechanics, in press.

Gupta, V., Argon, A. S. and Suo, Z. 1992. Crack deflection at an interface between two orthoptropic materials. J. of Applied Mechanics, 59, s79-s87.

Hahn, G. T., Hoagland, R. G., Lereim, J., Markworth, A. J. and Rosenfield, A. R. 1980. Fast fracture toughness and crack arrest toughness of reactor pressure vessel steel. Crack arrest methodology and applications, ASTM STP 711, G. T. Hanh and M. F. Kanninen, Eds., American Society for Testing and Materials, 1980, pp. 289-320.

He, M. Y. and Hutchinson, J. W. 1989 a, Crack deflection at an interface between dissimilar elastic materials. International J. of Solids and Structures. 25, 1053-1067.

He, M. Y. and Hutchinson, J. W. 1989b, Kinking of a crack out of an interface. J. of Applied Mechanics, 56, 270-278.

Hutchinson, J. W. and Suo, Z., 1992. Mixed mode cracking in layered materials. Advances in Applied Mechanics. 29, 63-191.

Kalthoff, J. F. 1983. On some current problems in experimental fracture. Workshop on dynamic fracture, W. G. Knauss, K. Ravi-Chandar, A. J. Rosakis ed., Pasadena. Caltech SM Report 83-12. pp.11-35.

Kobayashi, A. S. and Mall, S. 1978. Dynamic fracture toughness of homalite-100. Experimental Mechanics, 18, 11-18.

Lee, O. S. and Knauss, W. G. 1989. Dynamic crack propagation along a weakly bonded planes in a polymer. Experimental Mechanics, 29, 342-345.

Leguillon, D., Lacroix, C. and Martin, E. 2000. Interface debonding ahead of a primary crack. Journal of the Mechanics and Physics of Solids, 48, 2137-2161.

Martinez, D. and Gupta, V. 1994. Energy criterion for crack deflection at an interface between two orthotropic media. . Journal of the Mechanics and Physics of Solids. 42 (8), 1247-1271.

Needleman, A. and Rosakis, A. J. 1999 The effect of bond strength and loading rate on the conditions governing the attainment of intersonic crack growth along interfaces. J. Mech. Phys. Solids, 47,2411-2449

Qin, Q. H. and Zhang X. 2000. Crack deflection at an interface between dissimilar piezoelectric materials, International J. of Fracture, 102, 355-370.

Rosakis, A. J., Samudrala, O., Singh, R. P. and Shukla, A. 1998. Intersonic crack propagation in bimaterial systems. Journal of the Mechanics and Physics of Solids, 46, 1789-1813.

Rosakis, A.J., Samudrala, O. and Coker, D. 1999. Cracks faster than shear wave speed. Science, 284 1337-1340.

Rosakis, A. J. 2000. Explosion at the Parthenon; can we pick up the pieces? Caltech Solid Mechanics report.

Rosakis, A. J. and Ravichandran, G. 2000. Dynamic failure mechanics. International J. of Solids and Structures. 37, 331-348.

Siegmund, T., Fleck, N. A. and Needleman, A. 1997. Dynamic crack growth across an interface. International J. of Fracture, 85, 381-402.

Sharon, E. and Fineberg, J. 1999. Confirming the continuum theory of dynamic brittle fracture for fast cracks, Nature, 397, 333-335.

Thouless, M. D. 1992. Mixed-mode fracture of a lubricated interface. Acta Metall. Mater. 40 (6) 1281-1286.

Washabaugh, P. G. and Knauss, W. G. 1994. A reconciliation of dynamic crack growth velocity and Rayleigh wave speed in isotropic brittle solids. International J. of Fracture 65, 97-114.

Xu, L. R. and Rosakis, A. J. 2001a. An experimental study of impact-induced failure events in homogeneous layered materials using dynamic photoelasticity and high-speed photography, Submitted to Optics and Lasers in Engineering.

Xu, L. R. and Rosakis, A. J. 2001b. Comparison of static tensile and shear strengths and fracture toughness of various adhesive bonds between elastic materials. In preparation.

Xu, L. R and Rosakis, A. J. 2001c. Dynamic failure in layered materials, Part II. layered systems with initial defects. In preparation.

List of tables

List of figures

Figure 23. Methodology for predicting interfacial crack speed following deflection (a) and effect of the interfacial fracture toughness on deflected interfacial crack speeds for the case of incident crack speed of 400 m/s (b).

Figure 24. Remotely induced dynamic interfacial decohesion due to an approaching mode-I crack at a weak interface (interfacial angle 30 degrees).

Table 1. Material properties of Homalite –100

Property	Homalite 100	
	Static (Strain rate ~ 10^{-3}/s)	Dynamic (Strain rate ~ 10^{3}/s)
Density ρ (kg/m^3)	1230	1230
Young's modulus (GPa)	3.45	
Dilatational wave speed c_l (m/s) (plane stress)	1890	2119
Shear wave speed c_s (m/s)	1080	1208
Rayleigh wave speed c_R (m/s)	1010	1110
Poisson's Ratio ν	0.35	0.35
Material fringe constant f_σ (kN/m)	23.7	

Table 2. Interfacial strengths and mode-I fracture toughnesses of different bonds

Interface	Tensile strength σ_c (MPa)	Shear strength τ_c (MPa)	Fracture toughness K_{IC} (MPa*$m^{1/2}$)	Γ_{IC} (J/m^2)
Homalite//Weldon-10// Homalite (strong)	7.74	>21.65	0.83	199.7
Homalite//polyester// Homalite		>23.26	0.56	90.9
Homalite//384// Homalite (weak)	6.75	7.47	0.38	41.9

Table 3. Comparison of predicted and measured interfacial crack speeds

	Strong interface		Weak interface	
Angles (degrees)	Predicted (m/s)	Experimental (m/s)	Predicted (m/s)	Experimental (m/s)
10	576	534		
30	559	766	944	1100/ 920
45			928	800
60			896	700

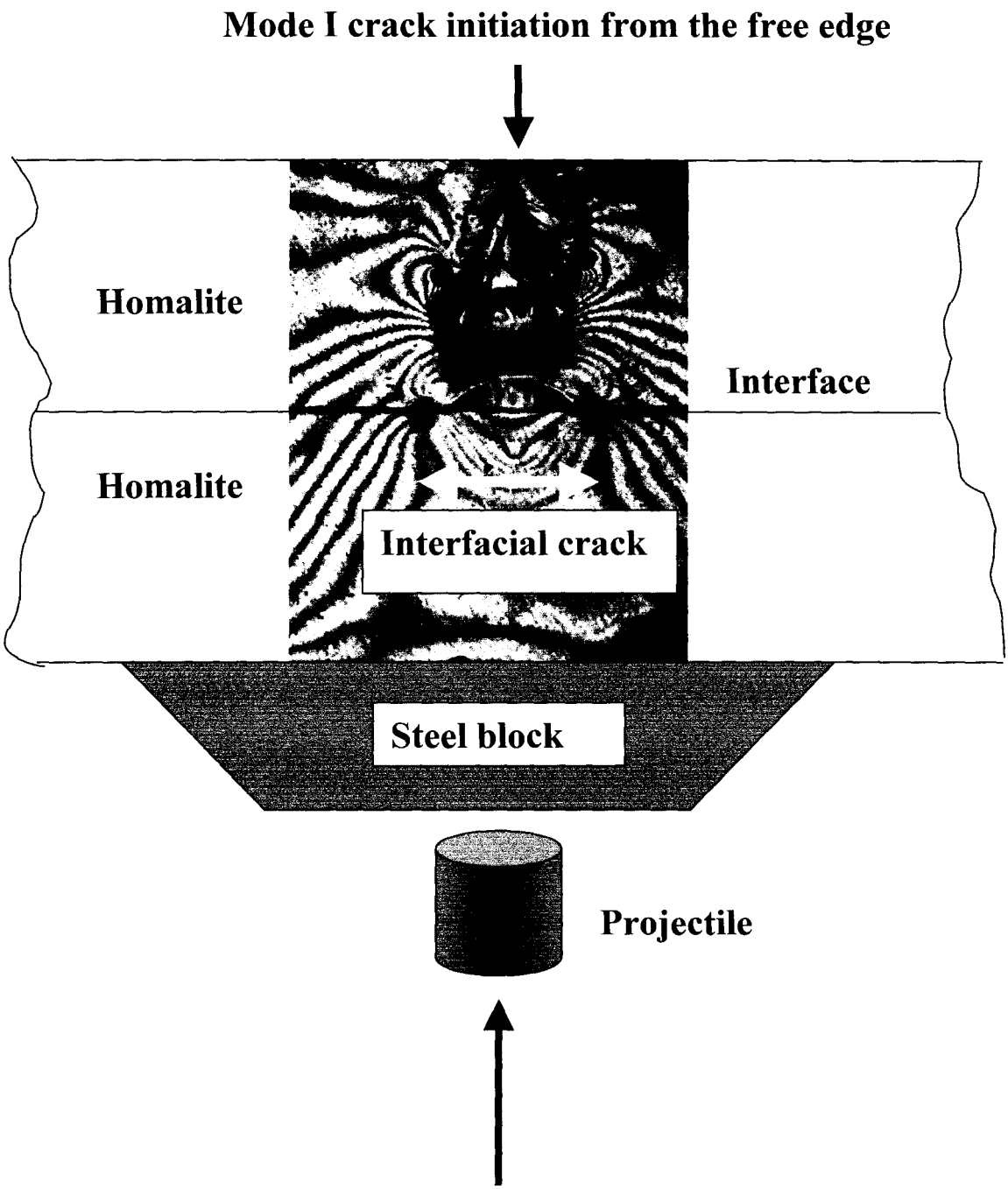

Figure 1. Experimental evidence of the dynamic equivalent of the "Cook-Gordon mechanism." A fan of mode-I cracks is incident on a horizontal interface inducing intersonic debonding before these mode-I cracks reach the interface (Xu and Rosakis, 2001a).

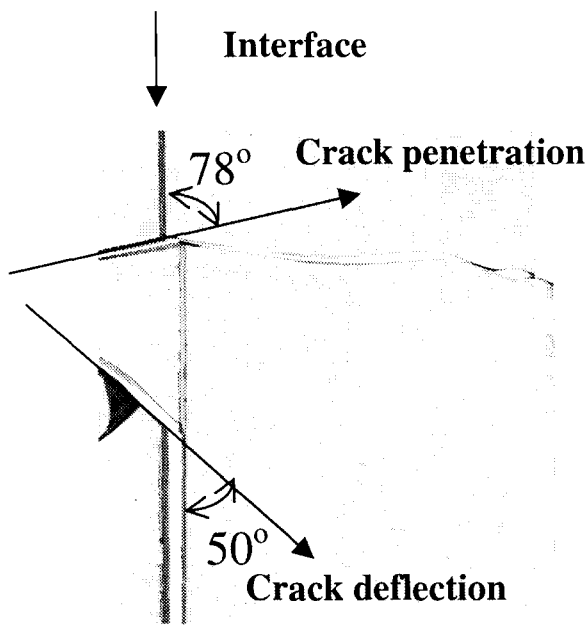

Figure 2. Experimental observations of the dynamic crack deflection/penetration at an interface. The incident cracks traveled at 300 m/s. If the angle between the crack path and the interface is small, the dynamic crack cannot penetrate the interface and only causes interface debonding (Xu and Rosakis, 2001a).

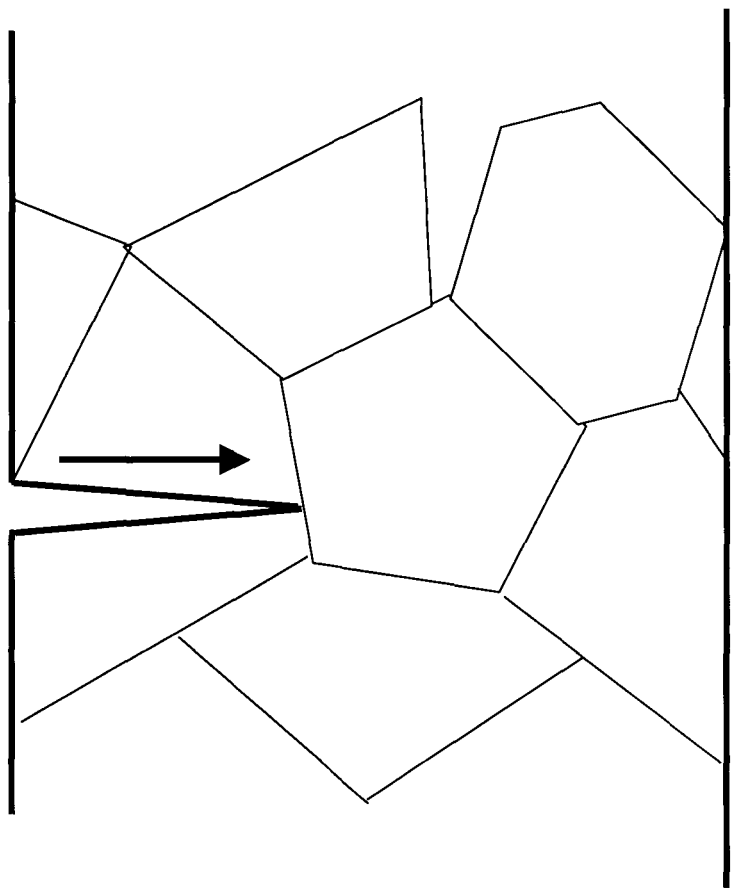

Figure 3. Dynamic crack propagation towards a grain boundary

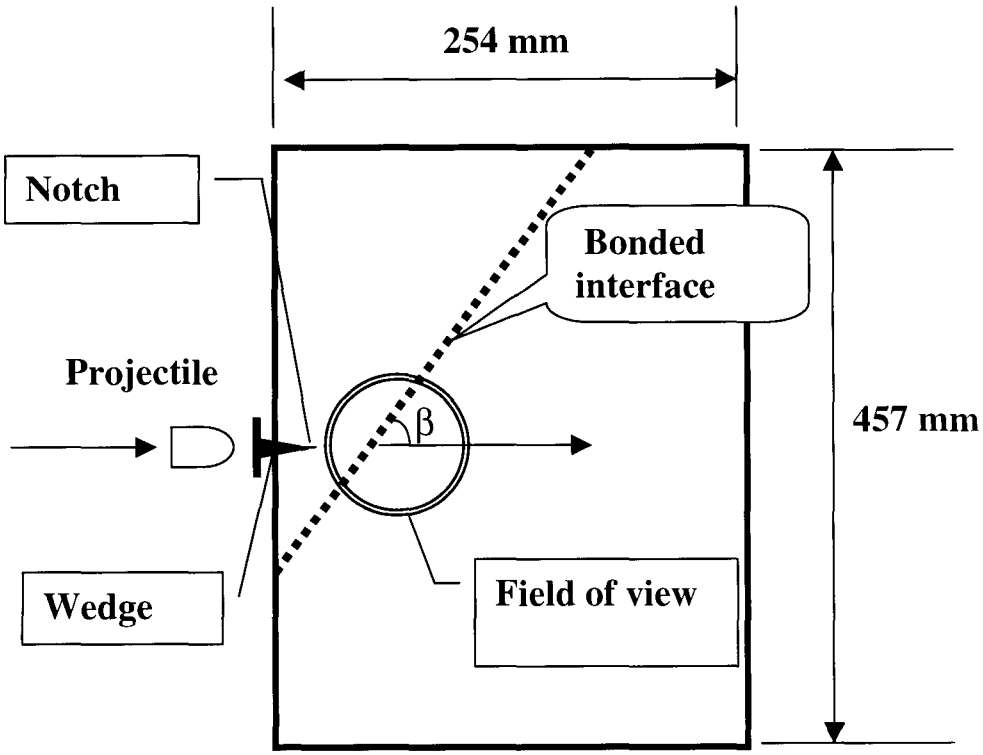

Figure 4. The wedge-loaded pre-notched specimen geometry

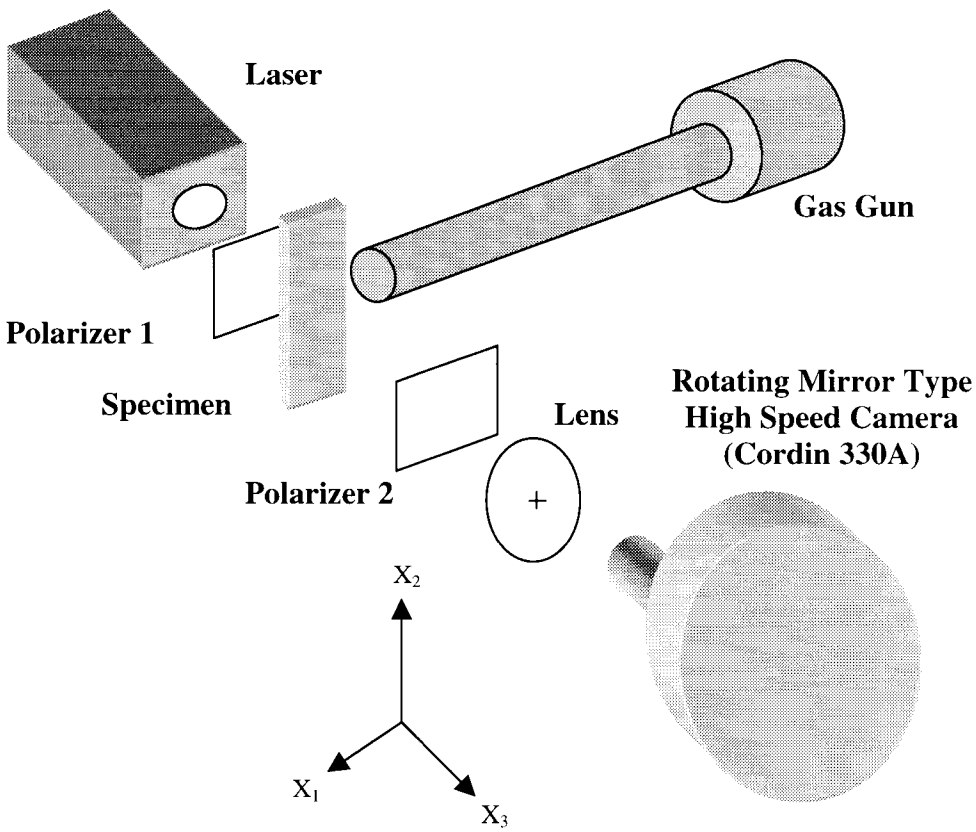

Figure 5. Schematic of the dynamic photoelasticity setup

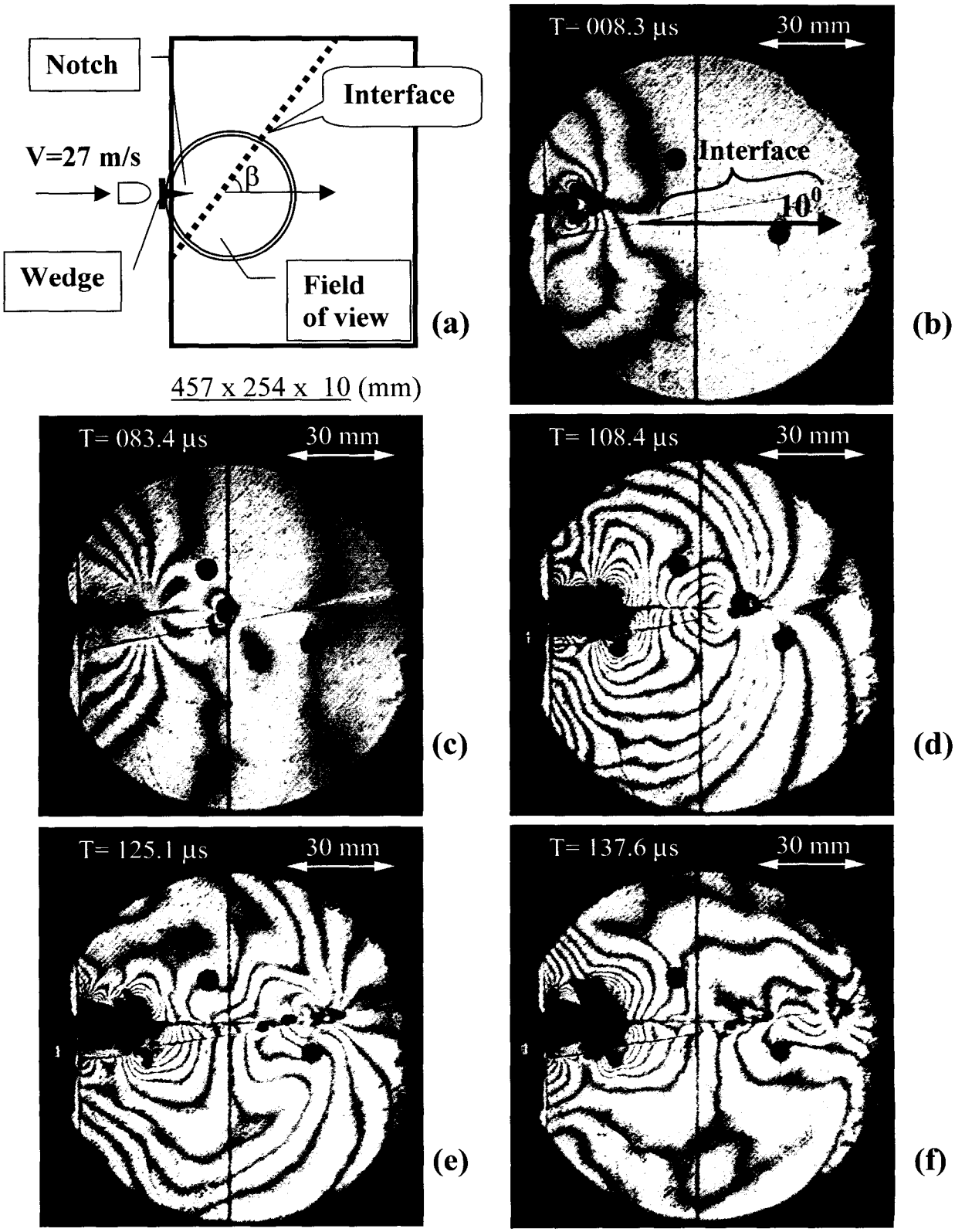

Figure 6. Crack deflection process at a weak interface (interfacial angle 10 degrees)

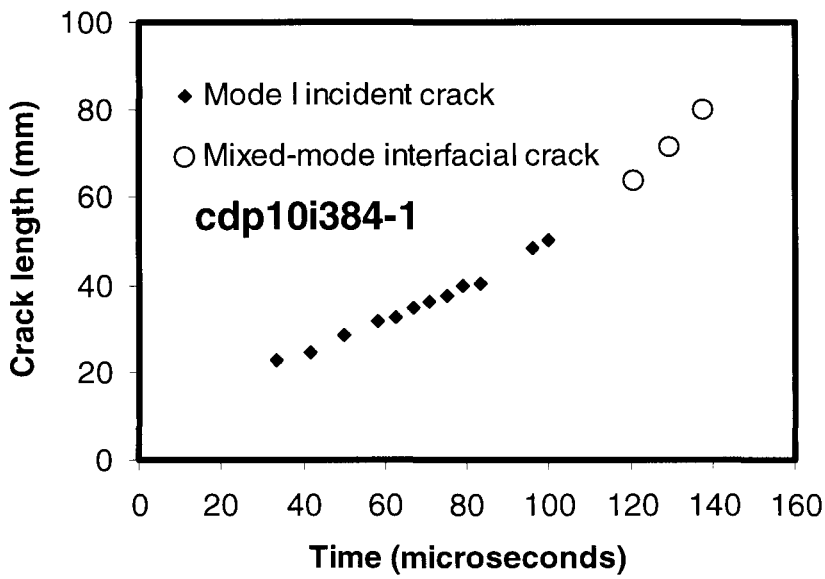

Figure 7. Crack length history before and after crack deflection at a weak interface (interfacial angle 10 degrees).

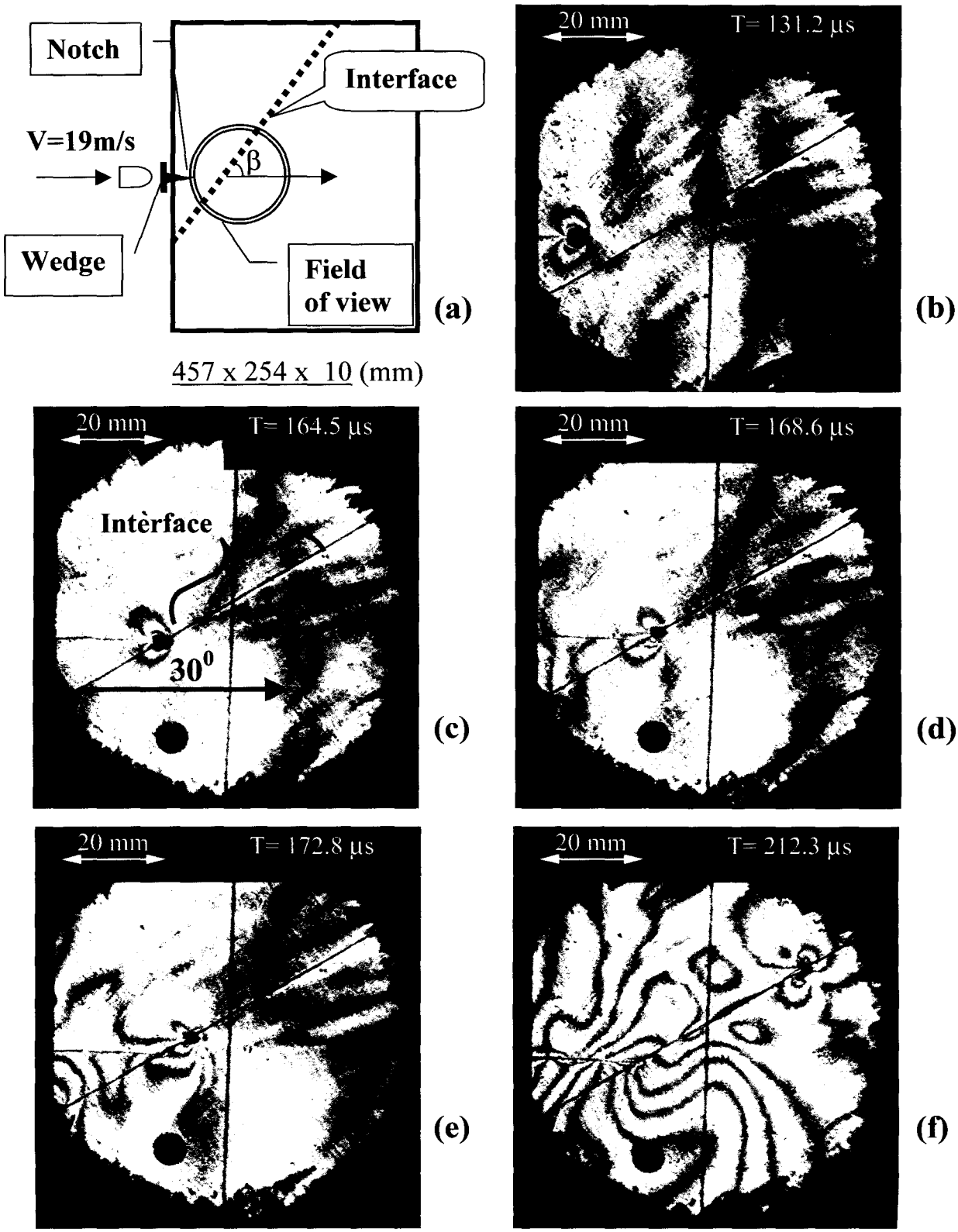

Figure 8. Crack deflection process at a weak interface (interfacial angle 30 degrees)

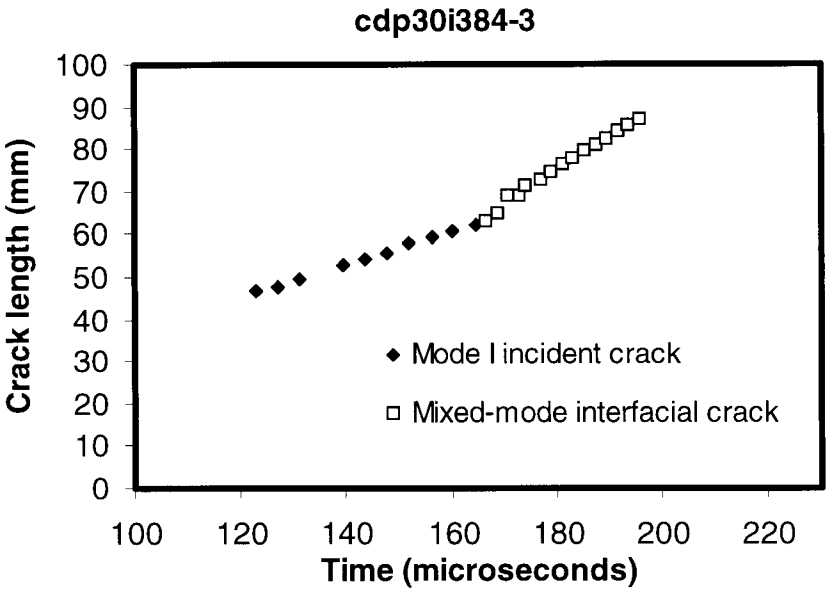

(a)

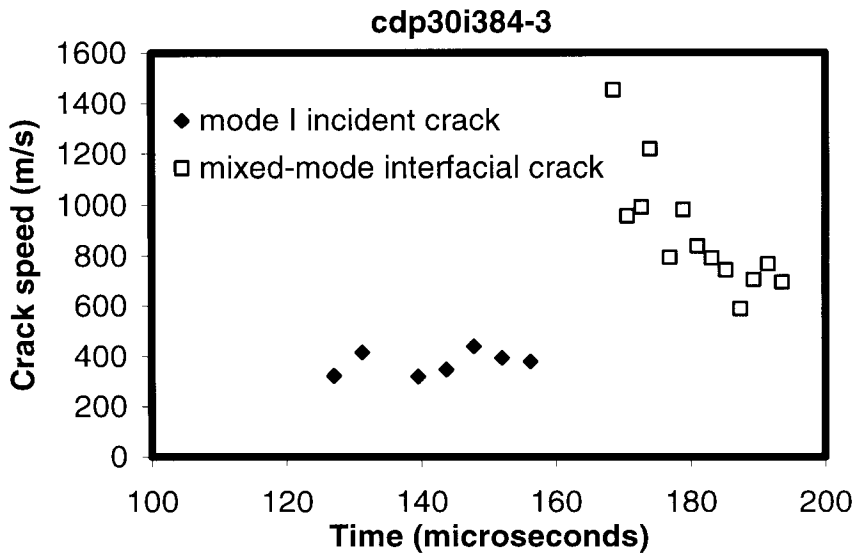

(b)

Figure 9. Crack length history (a) and crack speed history (b) before and after crack deflection at a weak interface (interfacial angle 30 degrees).

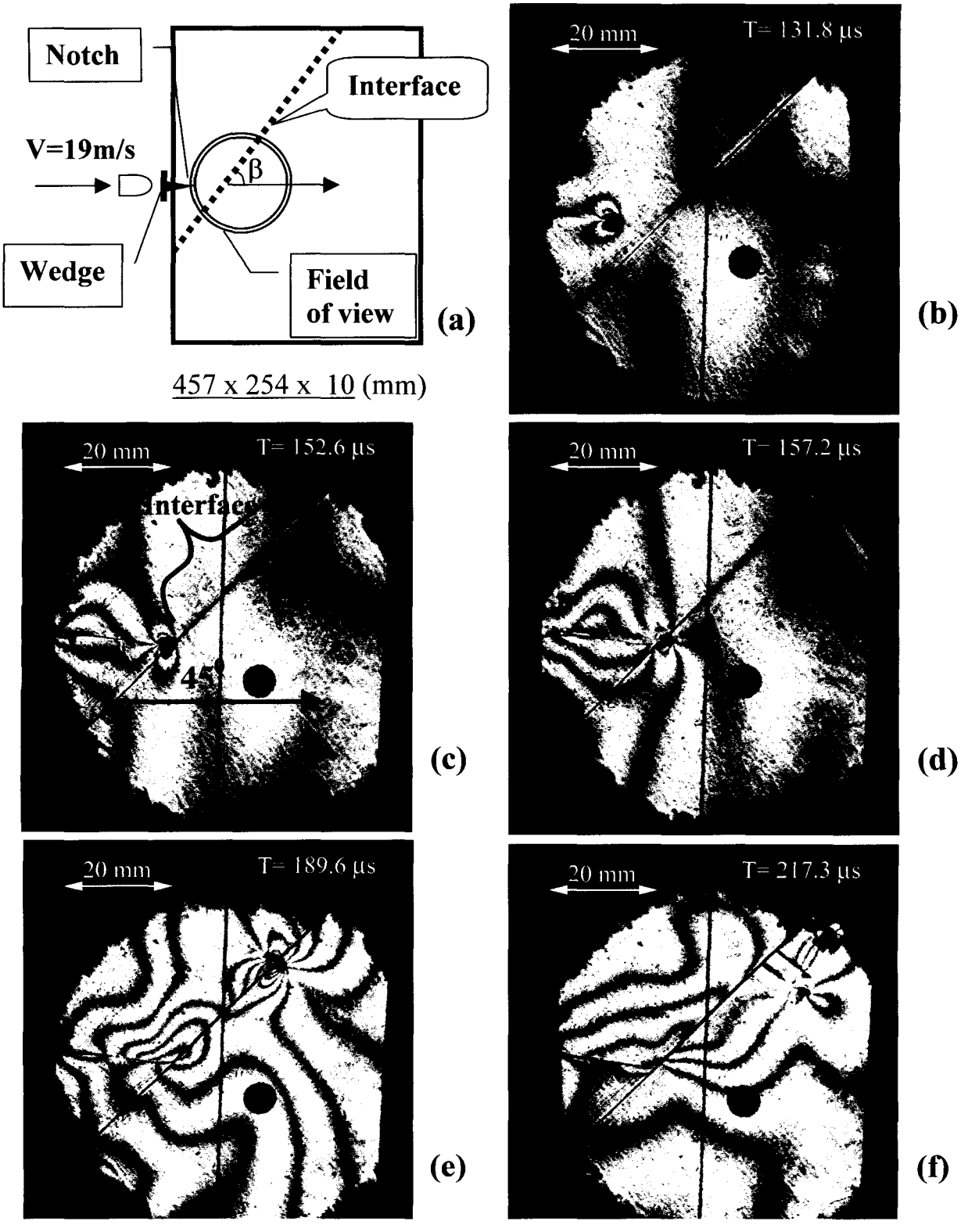

Figure 10. Crack deflection process at a weak interface (interfacial angle 45 degrees)

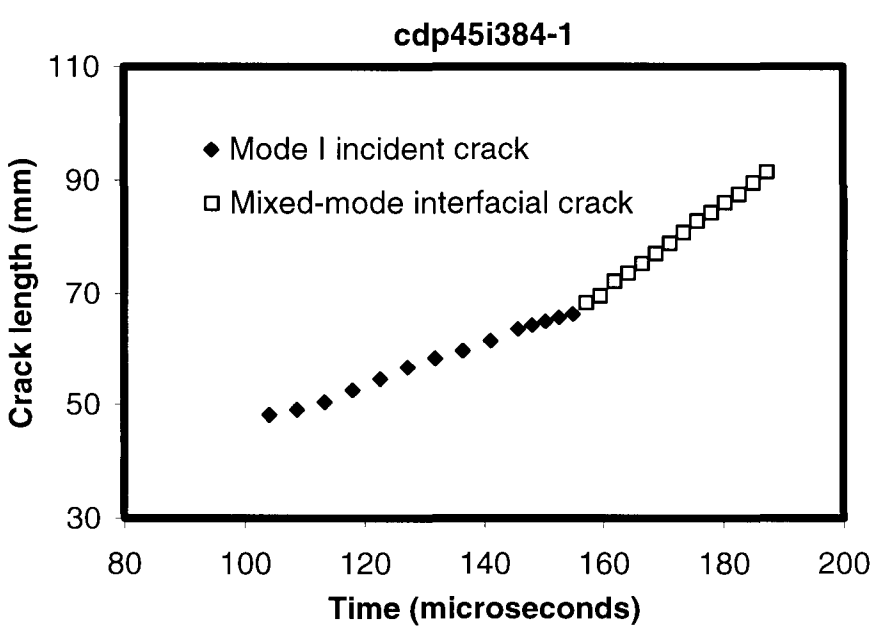

(a)

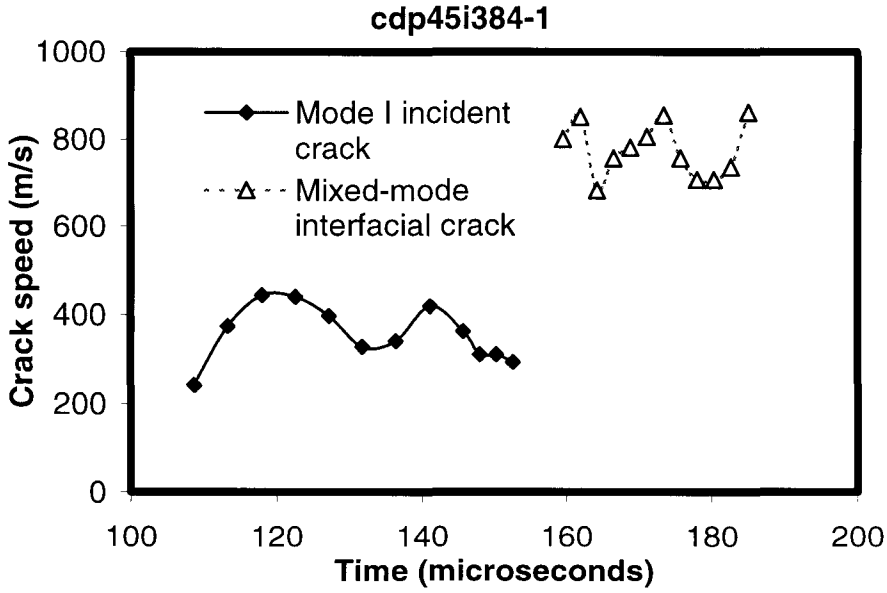

(b)

Figure 11. Crack length history (a) and crack speed history (b) before and after crack deflection at a weak interface (interfacial angle 45 degrees).

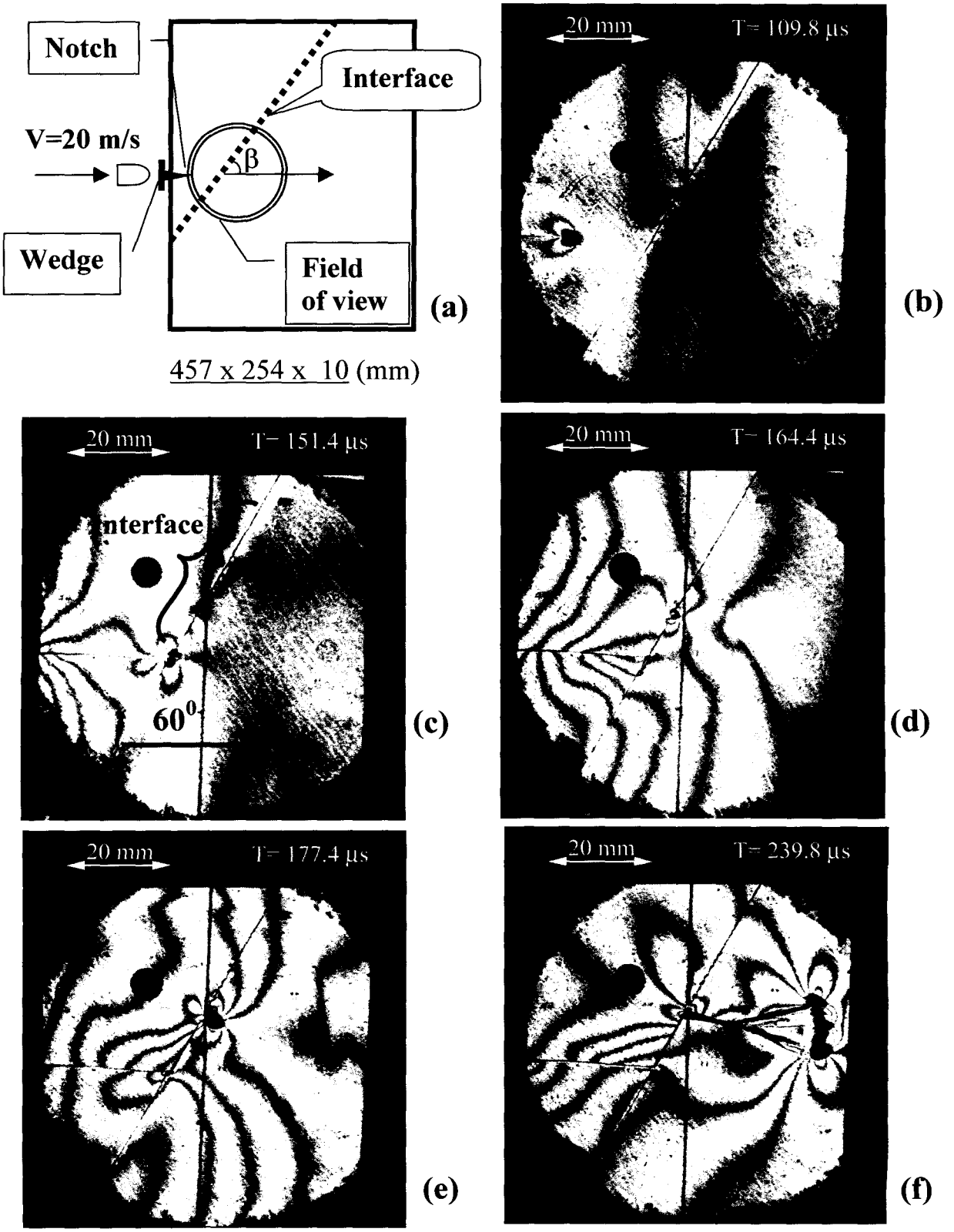

Figure 12. Crack deflection process at a weak interface (interfacial angle 60 degrees)

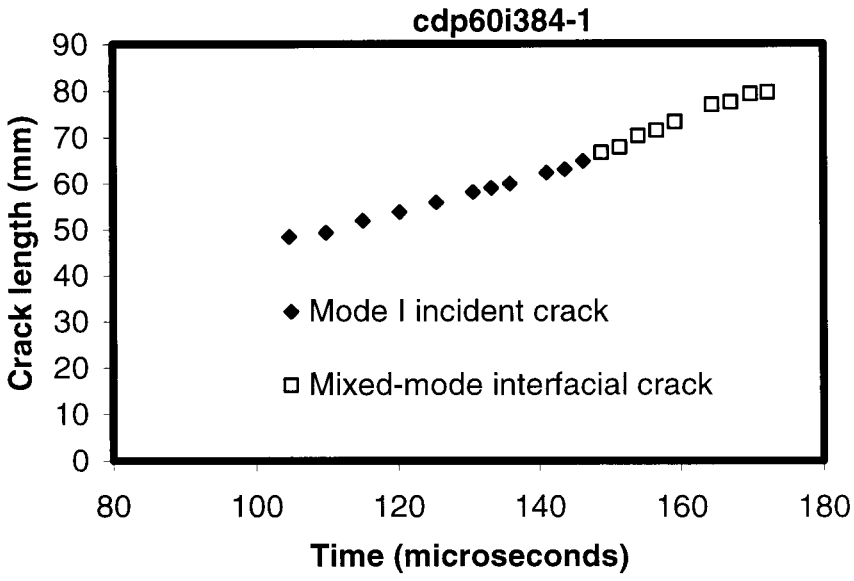

(a)

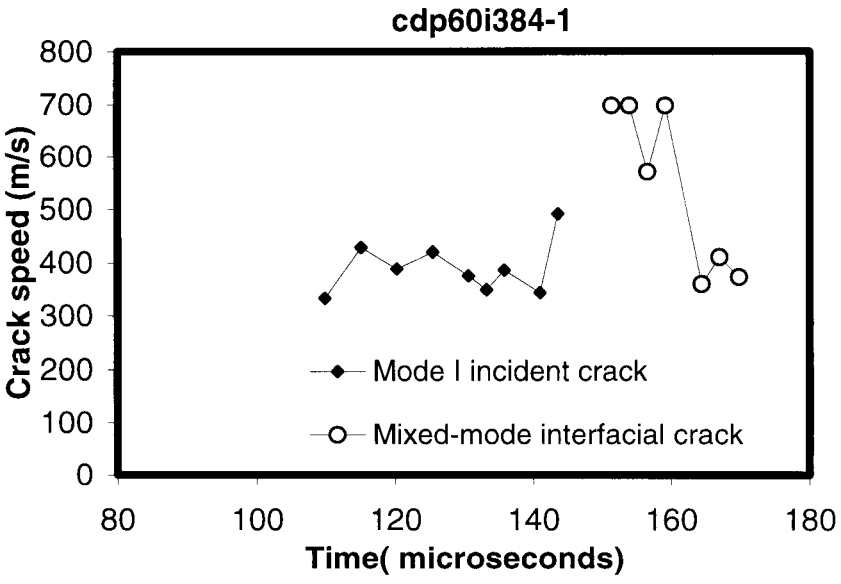

(b)

Figure 13. Crack length history (a) and crack speed history (b) before and after crack deflection at a weak interface (interfacial angle 60 degrees).

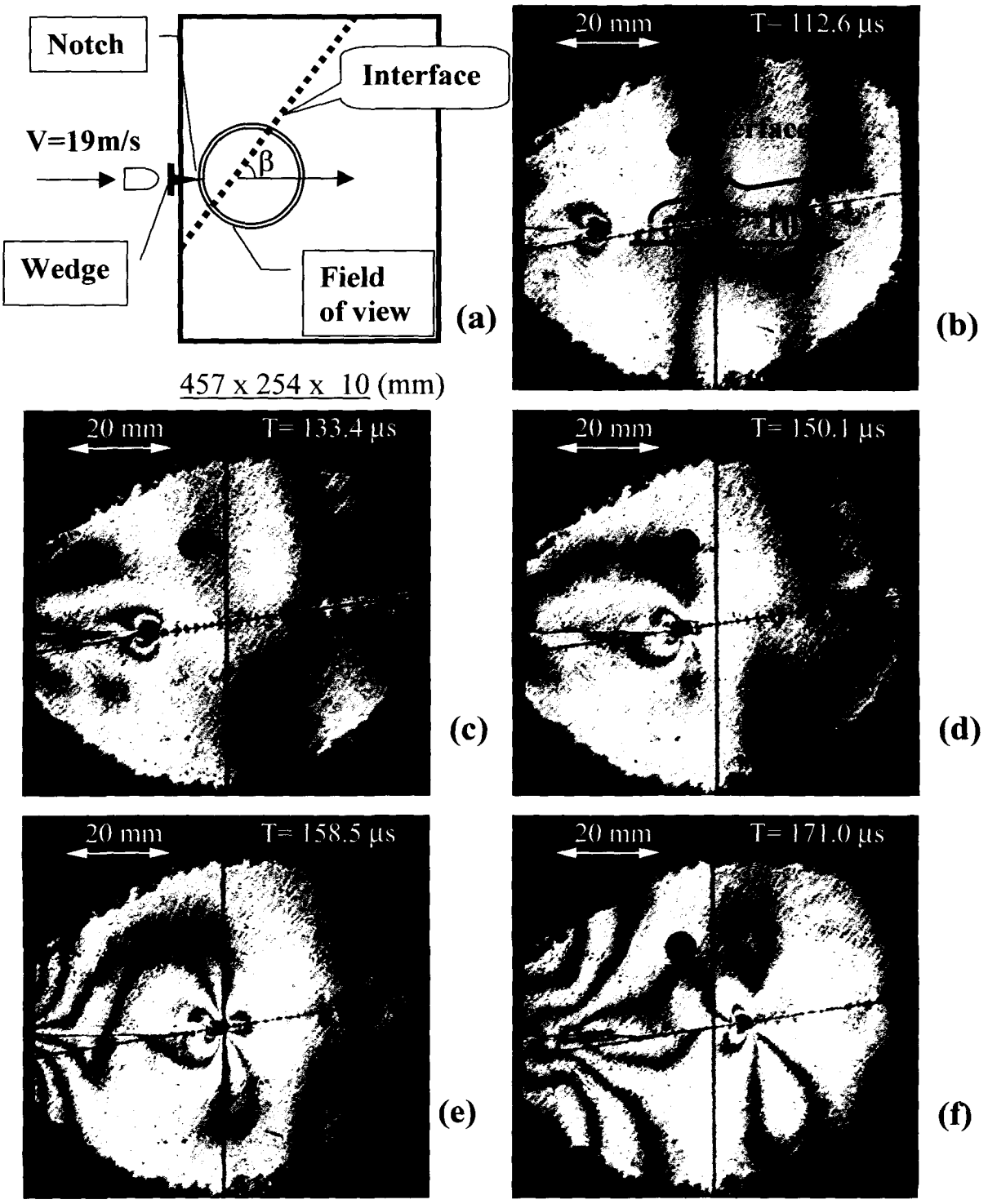

Figure 14. Crack deflection process at a strong interface (interfacial angle 10 degrees)

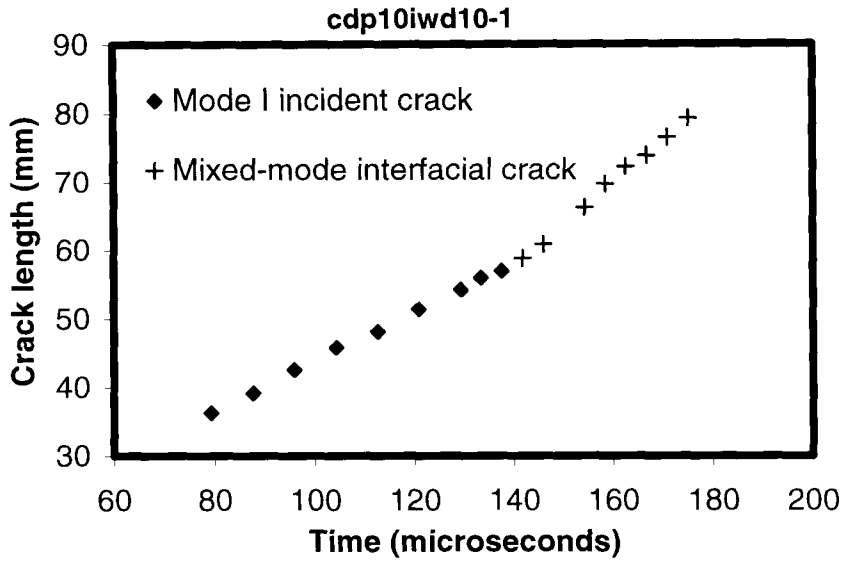

(a)

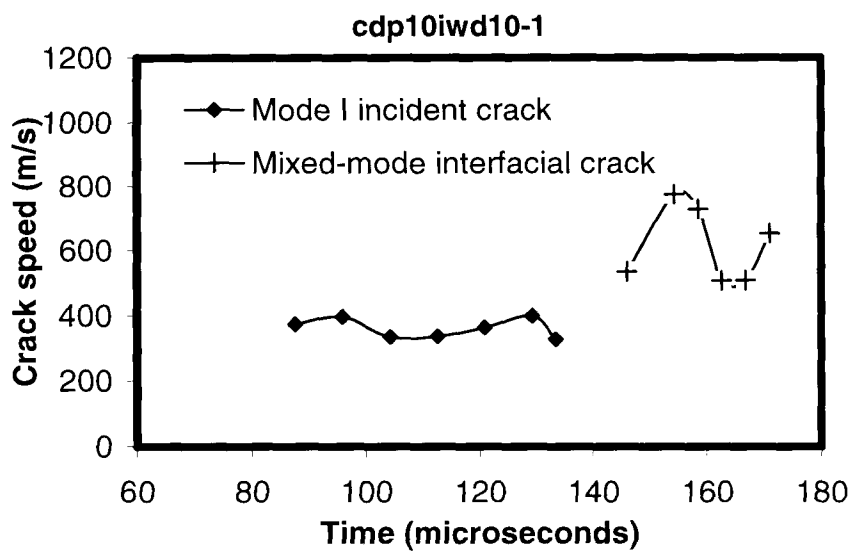

(b)

Figure 15. Crack length history (a) and crack speed history (b) before and after crack deflection at a strong interface (interfacial angle 10 degrees).

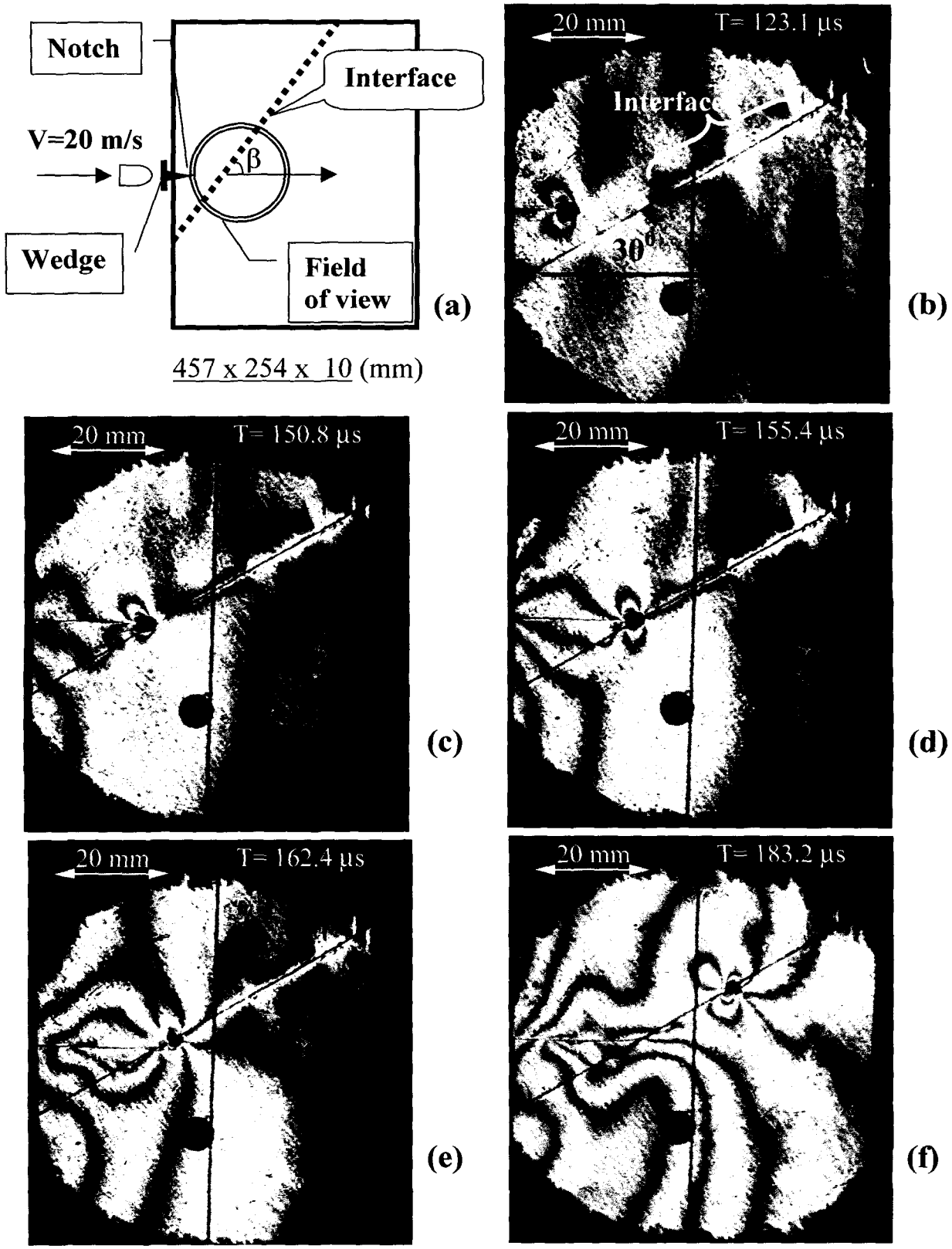

Figure 16. Crack deflection process at a strong interface (interfacial angle 30 degrees)

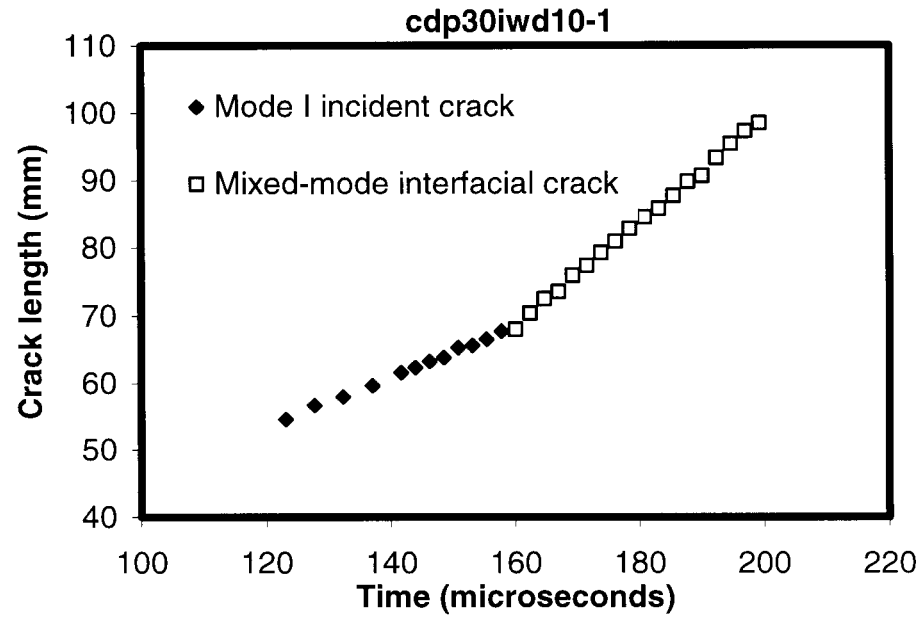

(a)

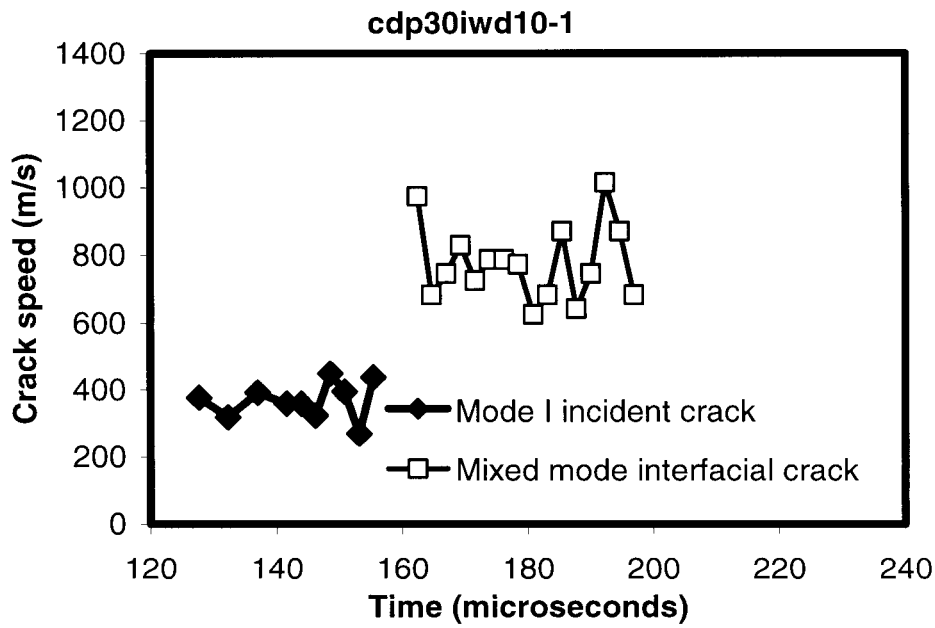

(b)

Figure 17. Crack length history (a) and crack speed history (b) before and after crack deflection at a strong interface (interfacial angle 30 degrees).

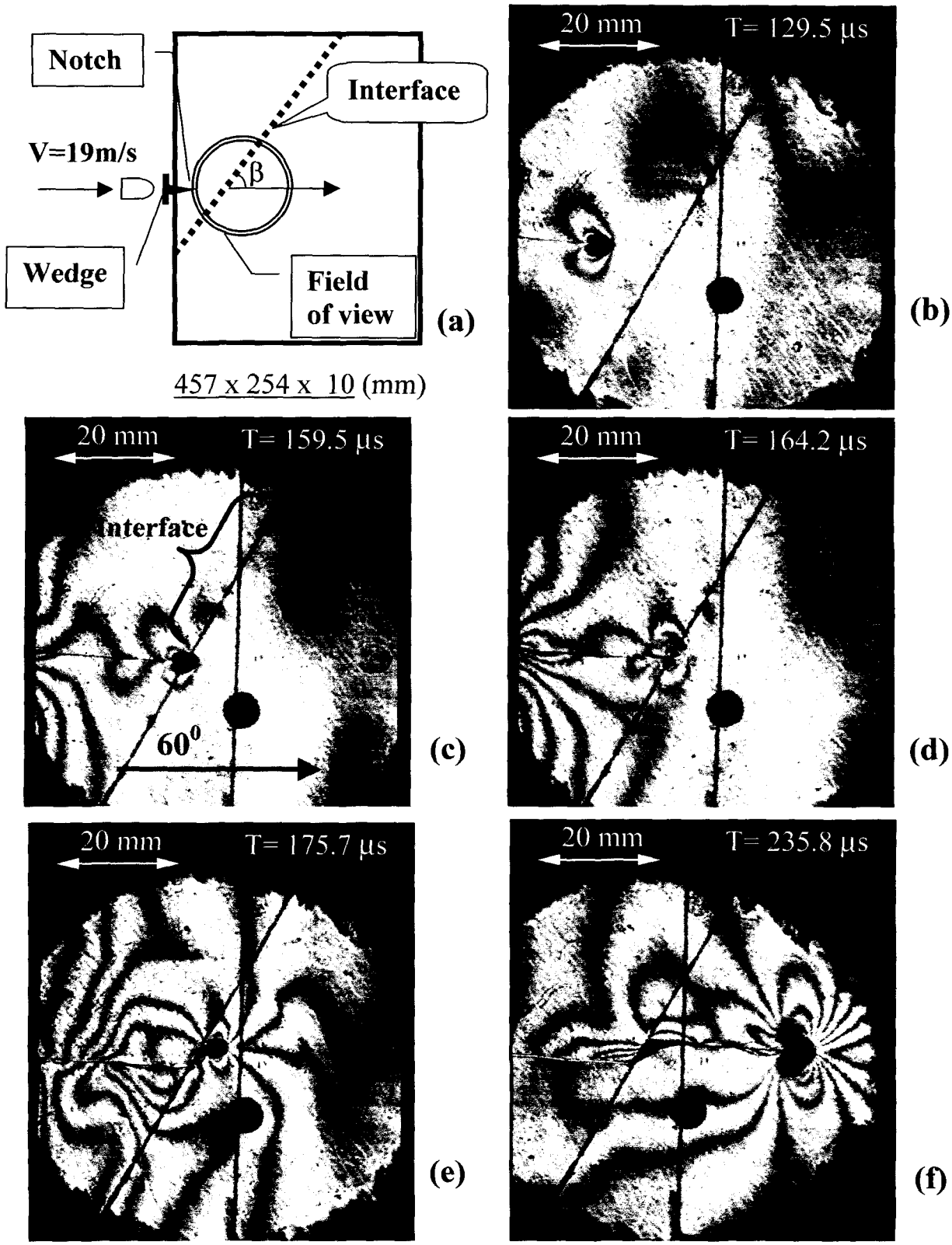

Figure 18. Crack deflection and subsequent penetration at a strong interface (interfacial angle 60 degrees)

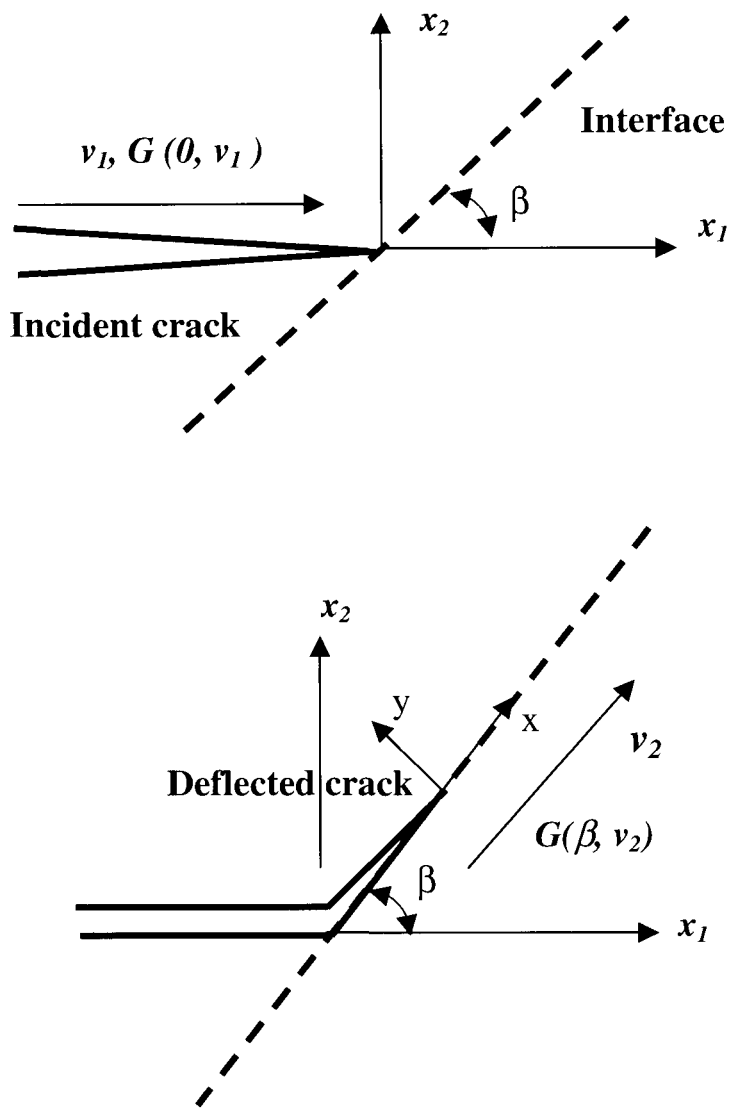

Figure 19. Schematic diagram showing a mode-I crack arriving (a) and subsequently deflecting at a weak interface between two identical homogenous solids (b).

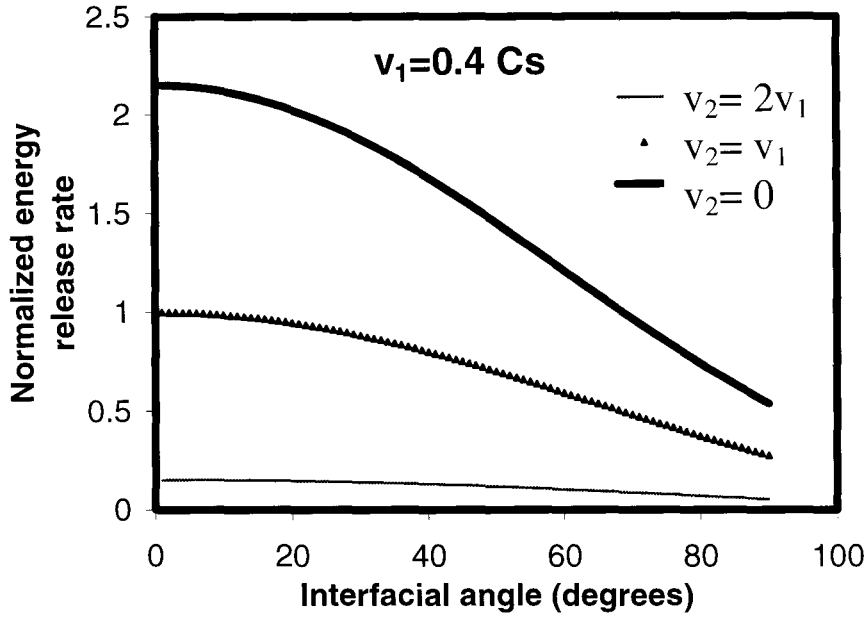

(a)

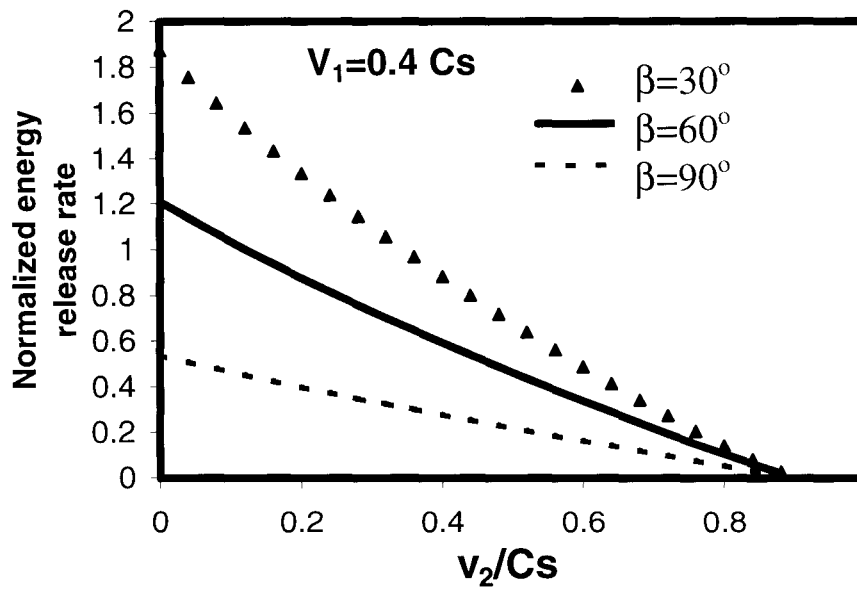

(b)

Figure 20. The energy release rate (driving force) for a deflected crack of speed v_2 normalized with the energy release rate of the incident mode-I crack (speed v_1=0.4 Cs) as a function of v_2 and different interfacial angles.

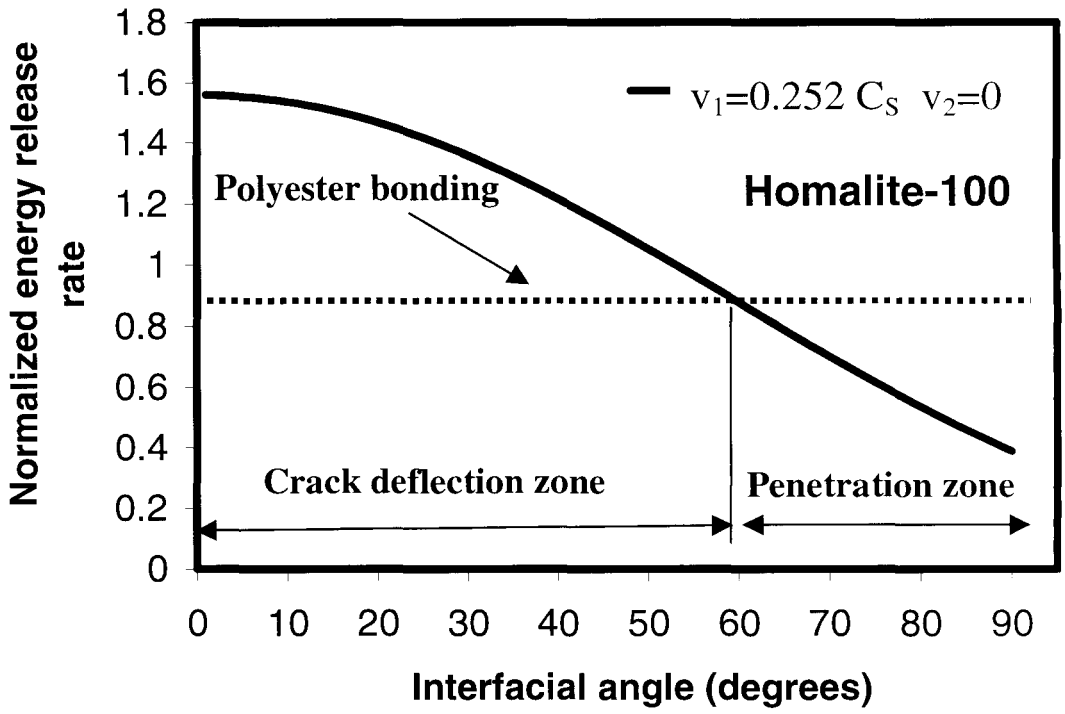

Figure 21. Prediction of the dynamic crack deflection /penetration regimes for a crack traveling at 300 m/s towards an interface bonded by a polyester adhesive.

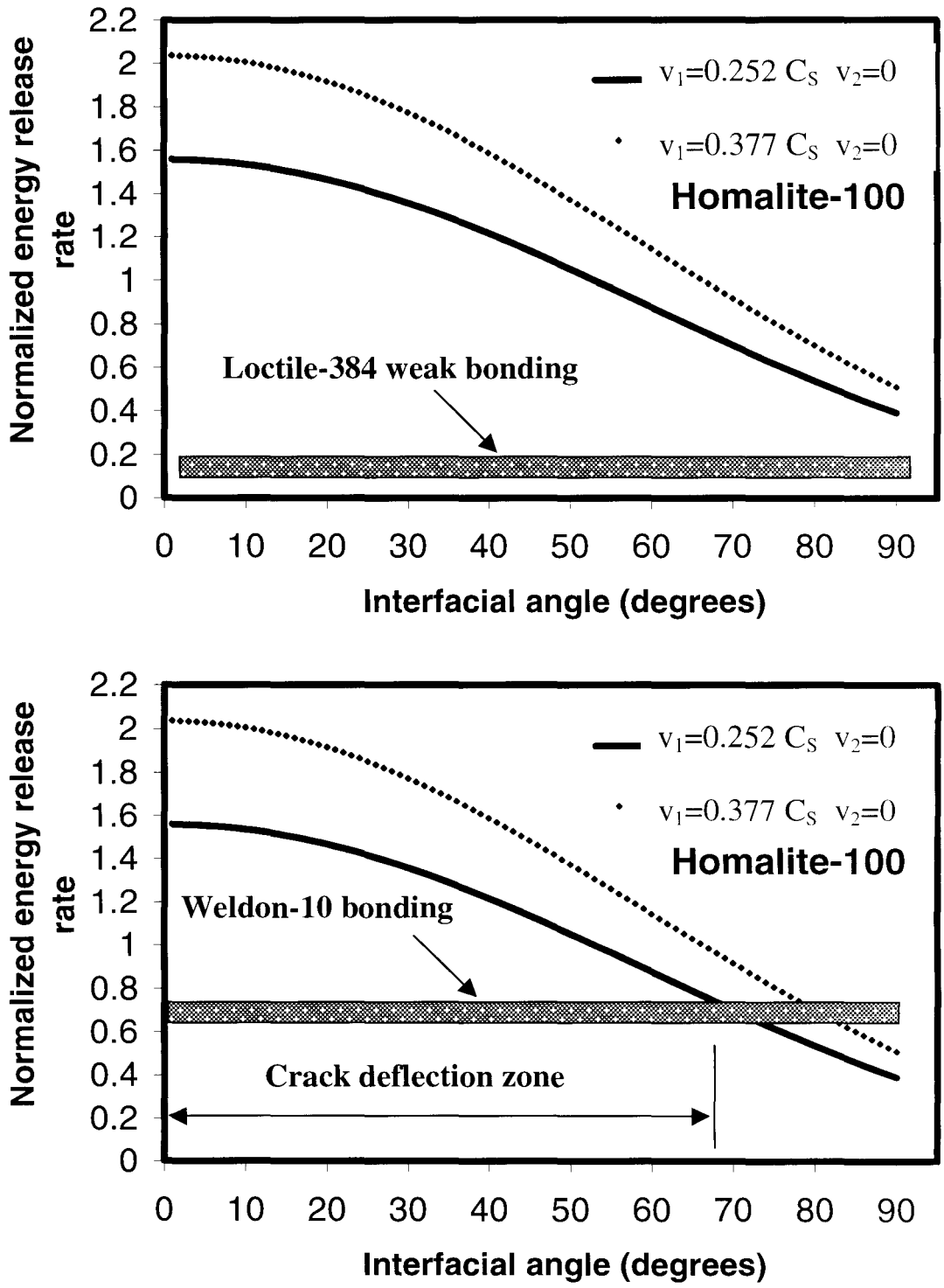

Figure 22. Prediction of dynamic crack deflection and penetration regimes at interfaces for a weak bond (a) and for a strong bond (b).

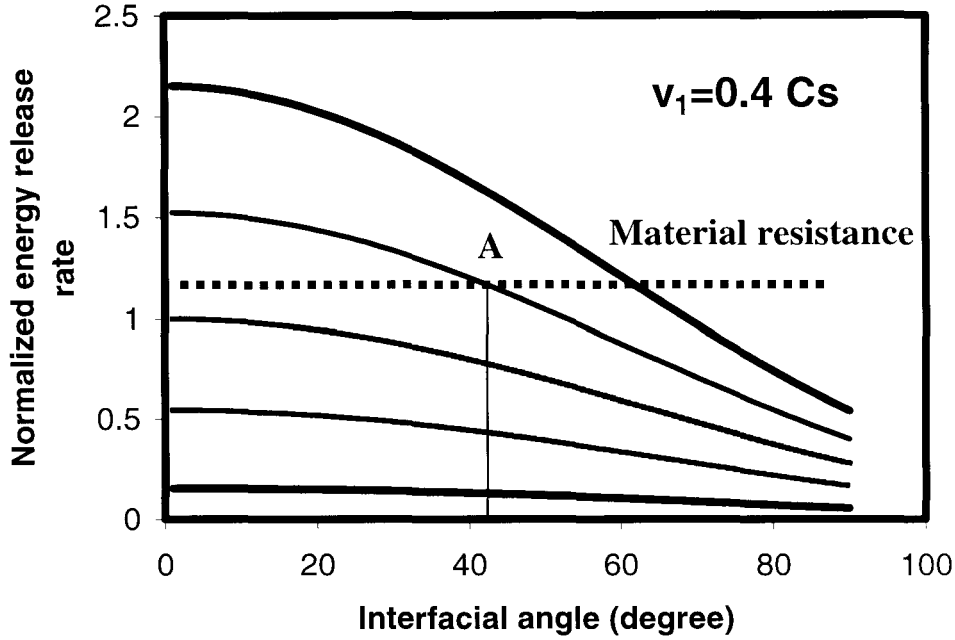

(a)

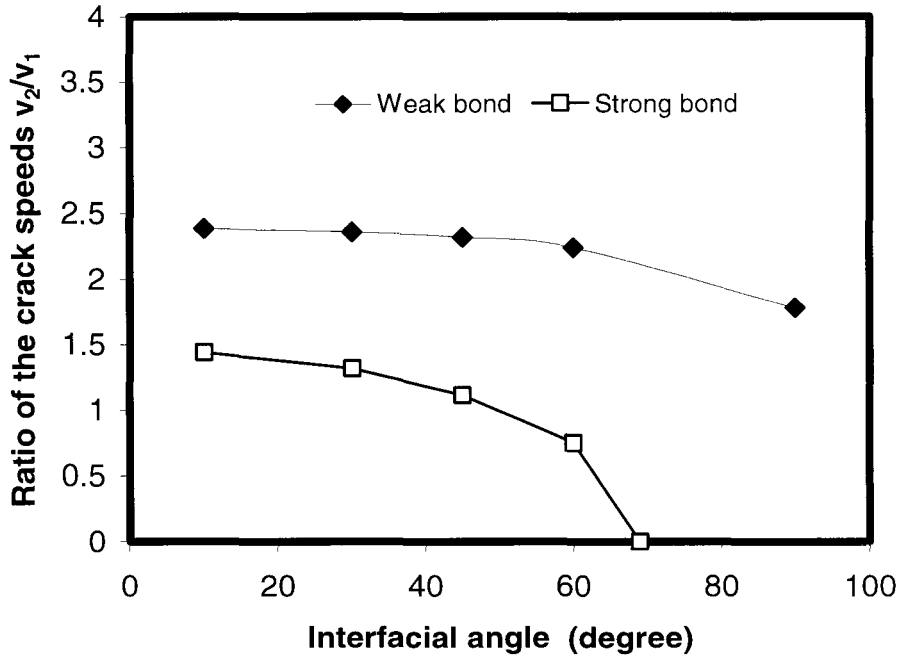

(b)

Figure 23. Methodology for predicting interfacial crack speed following deflection (a) and effect of the interfacial fracture toughness on deflected interfacial crack speeds for the case of incident crack speed of 400 m/s (b).

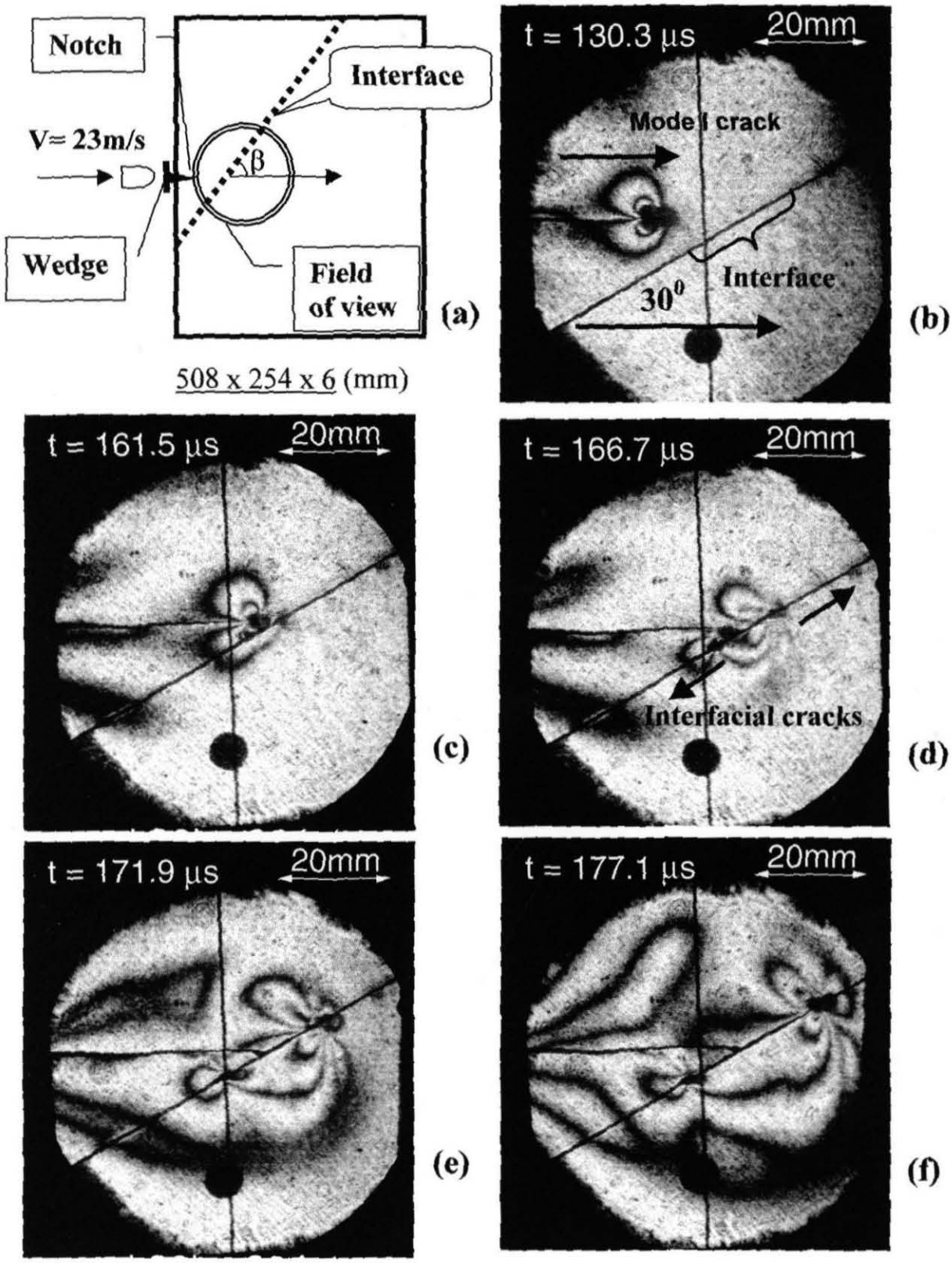

Figure 24. Remotely induced dynamic interfacial decohesion due to an approaching mode-I crack at a weak interface (interfacial angle 30 degrees)